NASA CR-163,189

NASA-CR-163189
19800015803

A Reproduced Copy

OF

NASA CR-163,189

() COMPARISON OF THEORETICALLY PREDICTED
LATERAL-DIRECTIONAL AERODYNAMIC
CHARACTERISTICS WITH FULL-SCALE WIND TUNNEL
DATA ON THE ATLIT AIRPLANE (Kansas Univ.
Center for Research, Inc.) 213 p

N80-24295

Unclas
G3/05 20998

THE UNIVERSITY OF KANSAS CENTER FOR RESEARCH, INC
2291 Irving Hill Drive—Campus West
Lawrence, Kansas 66045

N80-24295 #

COMPARISON OF THEORETICALLY PREDICTED LATERAL-DIRECTIONAL AERODYNAMIC CHARACTERISTICS WITH FULL-SCALE WIND TUNNEL DATA ON THE ATLIT AIRPLANE

KU-FRL-399-2

This work was performed under
NASA Grant NSG-1574

Prepared by: Michael Griswold

Principal Investigator: J. Roskam

University of Kansas
Lawrence, Kansas

May 1980

ABSTRACT

In this report an analytical method is presented for predicting lateral-directional aerodynamic characteristics of light twin-engine propeller-driven airplanes.

This method is applied to the Advanced Technology Light Twin-Engine (ATLIT) airplane. The calculated characteristics are correlated against full-scale wind tunnel data.

The method predicts the sideslip derivatives fairly well, although angle of attack variations are not well predicted. Spoiler performance was predicted somewhat high but was still reasonable. The rudder derivatives were not well predicted, in particular the effect of angle of attack. The predicted dynamic derivatives could not be correlated due to lack of experimental data.

TABLE OF CONTENTS

TABLE OF CONTENTS (continued)

TABLE OF CONTENTS (continued)

TABLE OF CONTENTS (continued)

LIST OF TABLES

LIST OF FIGURES

LIST OF FIGURES (continued)

LIST OF FIGURES (continued)

LIST OF FIGURES (continued)

LIST OF FIGURES (continued)

LIST OF FIGURES (continued)

LIST OF SYMBOLS

Symbol	Definition	Dimension
A	Aspect ratio	
$A_{v_{eff}}$	Effective vertical tail aspect ratio	
B_1	$1 - M^2$; compressibility factor	
B_2	$1 - \cos^2 \Lambda_{c/4} M^2$; swept compressibility factor	
b	Span	m (ft)
b_p	Propeller blade width	m (ft)
C_1, C_2	Propeller sidewash factors	
$(C_{D_o})_w$	Wing zero lift drag coefficient	
C_L	Lift coefficient	
$C_{L_{max}}$	Maximum lift coefficient	
C_{L_α}	Lift curve slope	deg^{-1}, rad^{-1}
$(C_{L_\alpha})_{N_p}$	Lift curve slope of the lift due to propeller normal force	deg^{-1}, rad^{-1}
$(C_{L_\alpha}')_v$	Effective C_{L_α} of the vertical tail	deg^{-1}, rad^{-1}
c_{l_α}	Section lift curve slope	deg^{-1}, rad^{-1}
$\frac{c_{l_\delta}}{(c_{l_\delta})_{theory}}$	Empirical lift effectiveness correction factor	
$(c_{l_\delta})_{theory}$	Theoretical section lift effectiveness	deg^{-1}, rad^{-1}
$c_{l_{\delta_r}}$	Section lift effectiveness of rudder	deg^{-1}, rad^{-1}

LIST OF SYMBOLS (continued)

Symbol	Definition	Dimension
C_ℓ	Rolling moment coefficient	
C_{ℓ_p}	Rolling moment due to roll rate	
C_{ℓ_r}	Rolling moment due to yaw rate	
C_{ℓ_β}	Rolling moment due to sideslip	deg^{-1}, rad^{-1}
C'_{ℓ_δ}	Rolling moment effectiveness	rad^{-1}
$C_{\ell_{\delta_r}}$	Rolling moment due to rudder deflection	deg^{-1}, rad^{-1}
$C_{\ell_{\delta_s}}$	Rolling moment due to spoiler deflection	deg^{-1}, rad^{-1}
$(C_{N_\alpha})_p$	Variation of propeller normal force with angle of attack	deg^{-1}, rad^{-1}
C_n	Yawing moment	
C_{n_p}	Yawing moment due to roll rate	rad^{-1}
C_{n_r}	Yawing moment due to yaw rate	rad^{-1}
C_{n_β}	Yawing moment due to sideslip	deg^{-1}, rad^{-1}
$C_{n_{\delta_r}}$	Yawing moment due to rudder deflection	deg^{-1}, rad^{-1}
$C_{n_{\delta_s}}$	Yawing moment due to spoiler deflection	deg^{-1}, rad^{-1}
C_{Y_β}	Side force due to sideslip	deg^{-1}, rad^{-1}
$C_{Y_{\delta_R}}$	Side force due to rudder deflection	deg^{-1}, rad^{-1}

LIST OF SYMBOLS (continued)

Symbol	Definition	Dimension
$\bar{c}$	Mean aerodynamic chord	m (ft)
c_1, c_2	Wing taper factors	
c_r	Root chord	m (ft)
c_t	Tip chord	m (ft)
$(d_f)_h$ $(d_f)_v$ $(d_f)_w$	Width of the fuselage at the appropriate surface	m (ft)
d_n	Maximum depth of the nacelle forward of the wing	m (ft)
f	Propeller inflow factor	
h	Maximum fuselage height	m (ft)
h_1	Fuselage height at one-quarter of the fuselage length from the nose	m (ft)
h_2	Fuselage height at three-quarters of the fuselage length from the nose	m (ft)
h_s	Distance from airfoil mean line to end of spoiler	m (ft)
J	Viscous drag parameter	
K'	Correction factor for lift effectiveness at high rudder deflection angles	
K_b	Rudder span factor	
K_h	Relative tail size factor	
K_i	Wing-body interference factor	
K_{M_Γ}	Compressibility correction for C_{l_β}	

LIST OF SYMBOLS (continued)

Symbol	Definition	Dimension
K_N	1) Empirical factor for fuselage C_{n_β} in the presence of the wing (Section 4.2.3) 2) Empirical normal propeller force factor (Section 6.1.1)	
k	Empirical sweep correction factor for viscous drag	
k_1, k_2	Nacelle reduced mass factors	
k_1'	Relative body size factor	
k_v	$(C_{l_\alpha})_v/2\pi$	
l_f	length of the fuselage	m (ft)
$l_{n_{eff}}$	length of the nacelle ahead of the wing	m (ft)
l_v	Distance from the center of gravity to the quarter-chord of the mean aerodynamic chord of the vertical tail, parallel to the X-body axis	m (ft)
l_v'	Distance parallel to the X-body axis from the center of gravity to the quarter chord of the mean aerodynamic chord of that portion of the vertical tail spanned by the rudder	m (ft)
M	Mach number	
N_{Re}	Reynolds number	
n_n	Number of nacelles	
prop	Propeller	
$\frac{\bar{q}_v}{\bar{q}_\infty}$	Dynamic pressure ratio at the vertical tail	

LIST OF SYMBOLS (continued)

Symbol	Definition	Dimension
$\frac{\bar{q}_n}{\bar{q}_\infty}$	Dynamic pressure ratio at the nacelle	
$\bar{q}_\infty$	Free stream dynamic pressure	N/m^2 (lb/ft^2)
R_p	Propeller radius	m (ft)
S	Area	m^2 (ft^2)
$(S_f)_s$	Fuselage side area	m^2 (ft^2)
S_p	Propeller disc area	m^2 (ft^2)
S_{x_n}	Nacelle effective cross section area equal to a circular cross section with a diameter equal to d_n	m^2 (ft^2)
T	Total propeller thrust	N (lb)
T'_c	$T/(\bar{q}_\infty S_w)$	
t/c	Maximum thickness ratio	
$\bar{v}$	Fuselage volume	m^3 (ft^3)
w_{max}	Maximum fuselage width	m (ft)
$\bar{x}$	$\bar{x}_{a.c.} - \bar{x}_{c.g.}$	
$x_{a.c.}$	Distance from the lifting surface apex to the aerodynamic center	m (ft)
$x_{ac_h}(c_r)_{le}$	Distance from leading edge of the vertical tail to the a.c. of the horizontal tail, in plane of the horizontal tail	m (ft)
$x_{c.g.}$	Distance from the center of gravity to the leading edge of the wing mean aerodynamic chord	m (ft)
$x_{c_{r_h}}(c_{r_v})$	Distance from root chord of vertical tail to root chord of horizontal tail	m (ft)

LIST OF SYMBOLS (continued)

Symbol	Definition	Dimension
x_m	Distance from the airplane nose to the center of gravity	m (ft)
x_n	Longitudinal distance from the center of gravity to the effective nacelle center of pressure	m (ft)
x_p	Longitudinal distance from the propeller to the airplane center of gravity	m (ft)
x'_p	Distance from the propeller to the wing quarter-chord along the thrust line	m (ft)
x_s	Distance from the airfoil leading edge to the end of the spoiler	m (ft)
$\bar{y}^*$	Spanwise location of centroid of angle of attack loading	
$y_{\bar{c}}$	Lateral distance from the root chord to the mean aerodynamic chord	m (ft)
y_T	Lateral distance from the thrust line to the center of gravity	m (ft)
$z_{c_{r_h}}(c_{r_v})$	Distance from the root chord of the vertical tail to the root chord of the horizontal tail	m (ft)
z_n	Vertical distance from the effective nacelle center of pressure to the center of gravity	m (ft)
z_p	Vertical distance from the thrust line to the airplane center of gravity	m (ft)
z_v	Distance from the center of gravity to the vertical tail mean aerodynamic chord, perpendicular to the X-body axis	m (ft)
z'_v	Distance parallel to the Z-body axis from the center of gravity to the quarter-chord of the mean aerodynamic chord of the portion of the vertical tail spanned by the rudder	m (ft)
z_w	Vertical distance from the X-axis of the equivalent circular fuselage to the quarter chord of the root chord of the exposed wing	m (ft)

LIST OF SYMBOLS (continued)

Symbol	Definition	Dimension
z'_w	Vertical distance from the airplane to the quarter chord of the root chord of the exposed wing	m (ft)
Greek Symbols		
α	Angle of attack relative to X-body axis	deg
α_{abs}	Absolute angle of attack $\alpha - \alpha_o + i$	deg
α_{o_f}	Fuselage zero lift angle of attack	deg
$(\alpha_\delta)_{C_L}$	$(\partial C_L/\partial\delta)/(\partial C_L/\partial\alpha)$	
$(\alpha_\delta)_{C_l}$	$(\partial C_l/\partial_\delta)/(\partial C_l/\partial\alpha)$	
β	Sideslip angle	deg
β'	Propeller blade angle	deg
Γ	Dihedral angle	deg
Δ	Empirical viscous drag increment	
$(\Delta C_L)_{N_p}$	Increment in lift coefficient due to propeller normal force	
$(\Delta C_L)_{\varepsilon_p}$	Increment in lift coefficient due to propeller downwash	
$(\Delta C_{L_\alpha})_{w(\Delta\bar{q})}$	Increment in wing lift curve slope due to power induced increased dynamic pressure	deg^{-1}, rad^{-1}
$(\Delta C_{L_\alpha})_{w(\varepsilon_p)}$	Increment in wing lift curve slop due to propeller downwash	deg^{-1}, rad^{-1}
$(\Delta C_{l_p})_{drag}$	Increment in C_{l_p} due to viscous drag	rad^{-1}
$(\Delta C_{l_p})_{N_p}$	Increment in C_{l_p} due to propeller normal force	rad^{-1}

LIST OF SYMBOLS (continued)

Symbol	Definition	Dimension
$(\Delta C_{\ell_p})_{power}$	Increment in C_{ℓ_p} due to power	rad^{-1}
$(\Delta C_{\ell_p})_{w(\Delta\bar{q}+\epsilon_p)}$	Increment in wing contribution to C_{ℓ_p} due to increased dynamic pressure and propeller downwash	rad^{-1}
$(\Delta C_{\ell_\beta})_{N_p}$	Increment in C_{ℓ_β} due to propeller normal force	deg^{-1}, rad^{-1}
$(\Delta C_{\ell_\beta})_{n(\Delta\bar{q}+\epsilon_p)}$	Increment in nacelle contribution to C_{ℓ_β} due to increased dynamic pressure and propeller downwash	deg^{-1}, rad^{-1}
$(\Delta C_{\ell_\beta})_{power}$	Increment in C_{ℓ_β} due to power	deg^{-1}, rad^{-1}
$(\Delta C_{n_\beta})_{N_p}$	Increment in C_{n_β} due to propeller normal force	deg^{-1}, rad^{-1}
$(\Delta C_{n_\beta})_{n(\Delta\bar{q})}$	Increment in nacelle contribution to C_{n_β} due to increased dynamic pressure	deg^{-1}, rad^{-1}
$(\Delta C_{n_\beta})_{n(\sigma_p)}$	Increment in nacelle contribution to C_{n_β} due to propeller sidewash	deg^{-1}, rad^{-1}
$(\Delta C_{n_\beta})_{power}$	Increment in C_{n_β} due to power	deg^{-1}, rad^{-1}
$(\Delta C_{Y_\beta})_{N_p}$	Increment in C_{Y_β} due to propeller normal force	deg^{-1}, rad^{-1}
$(\Delta C_{Y_\beta})_{n(\Delta\bar{q})}$	Increment in nacelle contribution to C_{Y_β} due to increased dynamic pressure	deg^{-1}, rad^{-1}
$(\Delta C_{Y_\beta})_{n(\sigma_p)}$	Increment in nacelle contribution to C_{Y_β} due to propeller sidewash	deg^{-1}, rad^{-1}

LIST OF SYMBOLS (continued)

Symbol	Definition	Dimension
$(\Delta C_{Y_\beta})_{power}$	Increment in C_{Y_β} due to power	deg^{-1}, rad^{-1}
$\frac{\Delta\bar{q}}{\bar{q}_\infty}$	Dynamic pressure increase behind the propeller as a ratio of the free stream dynamic pressure	
$\frac{\Delta\bar{q}_n}{\bar{q}_\infty}$	Dynamic pressure increase at the nacelles due to propeller as a ratio of the free stream dynamic pressure	
$\Delta\alpha's$	Spoiler lift effectiveness in terms of the change in zero-lift angle of attack	deg, rad
δ_R	Rudder deflection	deg, rad
δ_s	Spoiler deflection	deg, rad
$\frac{\partial C_{D_o}'}{\partial\alpha}$	Variation of viscous drag with angle of attack	
$\frac{\partial\varepsilon_p}{\partial\alpha_p}$	Downwash gradient behind the propeller	
$\frac{\partial\varepsilon_u}{\partial\alpha_w}$	Upwash gradient at the propeller	
$\frac{\partial\sigma}{\partial\frac{pb_w}{2V}}$	Variation of sidewash with wing tip helix angle	
$\frac{\partial\sigma}{\partial\beta}$	Variation of sidewash with sideslip	
$\frac{\partial\sigma_p}{\partial\beta}$	Variation of propeller sidewash with sideslip	
ε_p	Downwash angle behind the propeller	deg
η	Non-dimensional spanwise station, $y/(b/2)$	

LIST OF SYMBOLS (continued)

Symbol	Definition	Dimension
θ	1) Wing twist	deg
	2) Effective spoiler sweep angle	deg
Λ	Sweep angle	deg
Λ_β	Corrected sweep angle, $\tan^{-1}[\tan(\Lambda_{c/4})/\beta]$	deg
λ	Taper ratio	
ϕ_{TE}	Section trailing-edge angle	deg

Subscripts

c/2	Half-chord line
c/4	Quarter-chord line
c.g.	Center of gravity
e	Exposed panel
f	Fuselage
fh	Fuselage-horizontal tail combination
h	Horizontal tail
ℓe	Leading edge
M	High subsonic mach number
max	Maximum
n	Nacelle
prop off	Propellers removed
power on	Propellers installed and power on
r	Root
t	Tip
v	Vertical tail

LIST OF SYMBOLS (continued)

Symbol	Definition
w	Wing
wf	Wing-fuselage combination
wfh	Wing-fuselage-horizontal tail combination

CHAPTER 1

INTRODUCTION

This report describes work carried out under the second phase of a project performed by the Flight Research Laboratory of the University of Kansas sponsored by Grant NSG 1574 from the National Aeronautics and Space Administration (NASA), Langley Research Center. The purpose of this project was to correlate theoretically predicted aerodynamic characteristics of the Advanced Technology Light Twin (ATLIT) airplane with full-scale wind tunnel and flight test data. The original phases of this project were

1. correlate theoretical predictions of longitudinal aerodynamic characteristics with full-scale wind tunnel data;
2. correlate theoretical predictions of lateral-directional aerodynamic characteristics with full-scale wind tunnel data;
3. correlate the results of point 1 and point 2 with flight test data.

The results of the longitudinal correlation (point 1) are presented in Reference 1. This report deals only with the lateral-directional correlation (point 2). Full scale wind tunnel data used in the correlation were taken from Reference 2. The methods used in the prediction were taken from References 3 and 4.

The purpose of this report is to present an analytical method for predicting the lateral-directional aerodynamic characteristics of this class of airplane and to correlate the predictions with full-scale wind tunnel tests to identify areas where current predictions fall short.

This report was originally to correlate the predicted characteristics with flight test data. However, aside from some performance data presented in Reference 5, sufficient flight test data is not yet available to perform a meaningful correlation. After consulting with NASA, it was agreed to delete the flight test correlation phase. Additional work of a similar nature (full-scale wind tunnel correlation) is presently being performed on another airplane in place of the ATLIT flight test correlation. Some derivatives for which no wind tunnel data were available are still presented for future comparison when this data becomes available.

CHAPTER 2

THE ATLIT AIRPLANE

The ATLIT airplane is a Piper PA-34-200 Seneca I general aviation low-wing monoplane with a number of high technology modifications. The major physical characteristics are listed in Table 2.1, and a three-view drawing is shown in Figure 2.1.

The improvements implemented on the ATLIT were

1. The original untapered, aspect ratio 7.25 wing having a 65_2412 airfoil and an area of 19.4 m^2 (208.7 ft^2) was replaced by a new tapered wing (taper ratio 0.5) with a higher aspect ratio (10.32) and a smaller area (14.4 m^2). The new wing used a 17-percent thick GA(W)-1 airfoil.
2. Full span 30-percent chord Fowler flaps replaced the original 20-percent chord plain flaps.
3. Spoilers were installed for roll control instead of ailerons.

The new wing area was made smaller and the aspect ratio increased to provide better drag characteristics than the original wing. The GA(W)-1 airfoil was used for its high lift-to-drag ratio and high maximum lift coefficient. For acceptable landing speeds, full span flaps were used with spoilers providing roll control. During flight test, supercritical propellers were also evaluated. However, these were not used in the full-scale wind tunnel tests and are therefore not considered here.

In addition a number of changes were made in part of the wind tunnel test to clean up the drag of the ATLIT. This resulted in "as built' and "fully clean" wind tunnel tests. All comparisons in this report are done using the "fully clean" wind tunnel data.

Table 2.1: Specifications of the ATLIT Airplane

Wing:	
Area, m^2 (ft^2)	14.40 (155.0)
Span, m (ft)	12.19 (40.0)
Aspect ratio	10.32
Thickness ratio	0.17
Dihedral, deg	7
Taper ratio	0.5
Incidence angle at root, deg	0.5
Incidence angle at tip, deg	-2.5
Leading edge and trailing edge sweep, deg	3.67
Mean aerodynamic chord, m (ft)	1.225 (4.018)
Root chord, m (in)	1.575 (62.0)
Tip chord, m (in)	0.787 (31.0)
Airfoil	GA(W)-1
Flap:	
Type	Fowler
Area (total), m^2 (ft^2)	3.56 (38.3)
Span/side, m (ft)	5.15 (16.91)
Chord, perc. of wing chord	30
Inboard wing station, m (in)	0.711 (28.0)
Outboard wing station, m (in)	5.867 (231.0)
Leading edge retracted, perc. of wing chord	70
Maximum deflection, deg	40
Maximum travel, m (in)	0.343 (13.50)
Root chord, m (in)	0.445 (17.50)
Tip chord, m (in)	0.244 (9.62)

Table 2.1: Continued

Spoiler:	
Type	Differential-Slat-Upper Surface
Area (total), m² (ft²)	0.488 (5.25)
Span/side, m (in)	3.226 (127.0)
Inboard wing station, m (in)	2.565 (101.0)
Outboard wing station, m (in)	5.791 (228.0)
Hinge, perc. of wing chord	70
Maximum deflection, deg	60
Root chord, m (in)	0.177 (6.975)
Tip chord, m (in)	0.124 (4.880)
Tail:	
Stabilator:	
Area (including tab), m² (ft²)	3.60 (38.7)
Span, m (ft)	4.13 (13.56)
Chord (constant), m (in)	0.871 (34.29)
Aspect ratio	4.75
Sweep angle, deg	0
Dihedral, deg	0
Hinge line, perc. of chord	26.6
Airfoil	NACA 0010
Vertical:	
Area (including tab), m² (ft²)	1.85 (19.9)
Span, m (ft)	1.52 (5.00)
Aspect ratio	1.19
Taper ratio	0.42
Root chord, m (in)	1.708 (67.23)
Tip chord, m (in)	0.723 (28.45)

Table 2.1: Continued

Mean aerodynamic chord, m (in)	1.282 (50.47)
Leading edge sweep angle, deg	39.92
Airfoil	NACA 0009
Stabilator tab:	
Area, m^2 (ft^2)	0.539 (5.8)
Span, m (in)	3.023 (119.0)
Chord (constant), m (in)	0.178 (7.0)
Tab hinge line to stabilator hinge line, m (in)	0.462 (18.17)
Rudder:	
Area (including tab), m^2 (ft^2)	0.706 (7.6)
Span, m (in)	1.525 (60.02)
Chord (constant), m (in)	0.449 (17.69)
Rudder trim tab:	
Area, m^2 (ft^2)	0.158 (1.7)
Span, m (in)	0.895 (35.25)
Chord (constant), m (in)	0.175 (6.9)
Powerplant:	
Number of engines	2
Manufacturer	Lycoming
Model	IO-360-C1E6
Takeoff rpm	2700
Takeoff power, hp	200
Propeller:	
Manufacturer	Hartzell
Model	HC-C2YK-1CEF/FC 7666A
Number of blades	2
Diameter, m (in)	1.930 (76.0)

Table 2.1: Concluded

Weights and Loading:	
Gross weight, N (lb)	17,792 (4,000)
Empty weight, N (lb)	11,018 (2,477)
Useful load, N (lb)	6,774 (1,523)
Wing loading (at gross weight), N/m^2 (lb/ft^2)	1,236 (25.8)

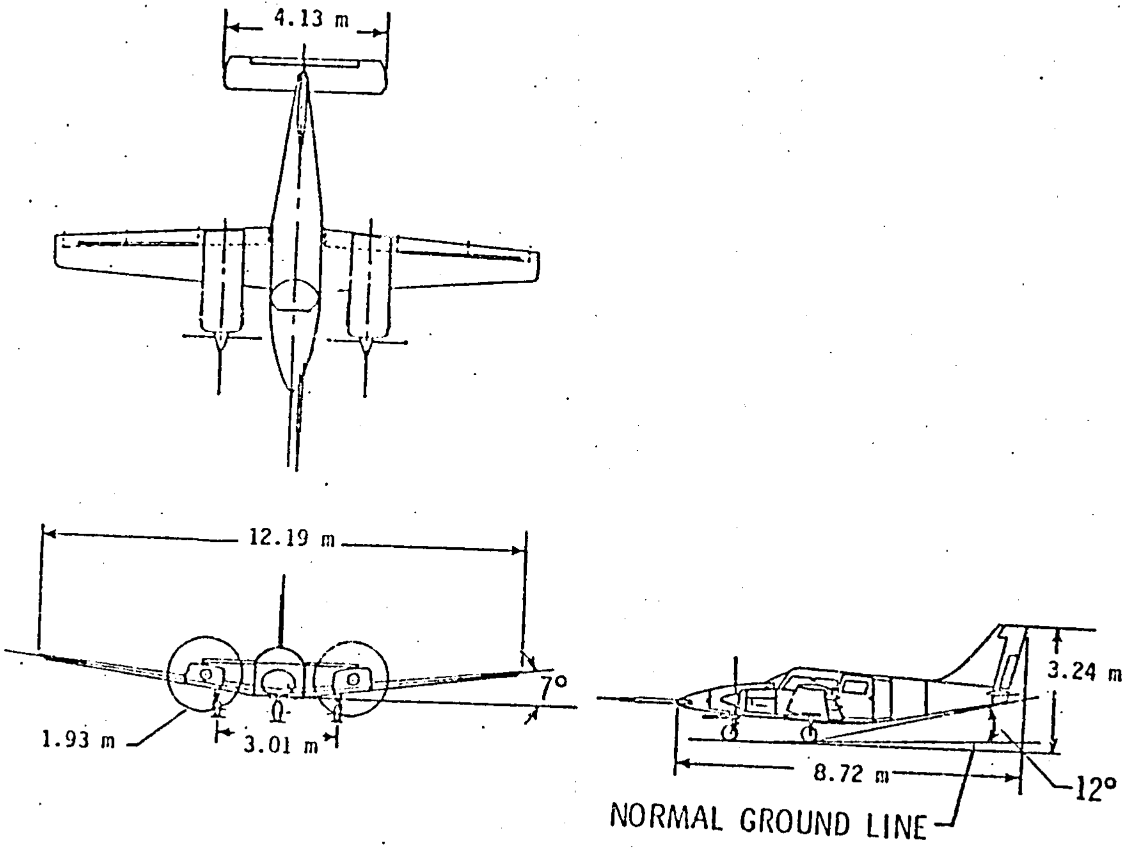

Figure 2.1: Three-view drawing of the ATLIT airplane (Reference 1)

2.1 Geometric Parameters of Wing and Tail

Depending on which characteristic has to be determined, the total area or the exposed area of the wing and the tail are considered. The total planform is considered to extend through the nacelle and the fuselage, while the exposed planform terminates at the fuselage. Pertinent dimensions for the wing, the horizontal tail and the vertical tail are shown in Figures 2.1.1, 2.1.2 and 2.1.3, respectively. Table 2.1.1 lists the geometric parameters of the wing and the tail pertinent in the analysis.

Table 2.1.1: Pertinent Wing and Tail Geometric Parameters Used in the Analysis

Symbol	Description	Wing		Horizontal Tail		Vertical Tail
		Total	Exposed	Total	Exposed	Exposed
S	Area, m^2 (ft^2)	14.40 (155.0)	12.53 (134.8)	3.60 (38.7)	3.25 (34.9)	1.75 (18.8)
b	Span, m (ft)	12.19 (40.0)	10.96 (36.0)	4.13 (13.56)	3.73 (12.23)	1.52 (5.0)
A	Aspect ratio, b^2/S	10.32	9.61	4.75	4.28	1.33
c_t	Tip chord, m (in)	0.787 (31.00)	0.787 (31.00)	0.871 (34.29)	0.871 (34.29)	0.723 (28.45)
c_r	Root chord, m (in)	1.575 (62.00)	1.495 (58.87)	0.871 (34.29)	0.871 (34.29)	1.575 (62.0)
λ	Taper ratio, c_t/c_r	0.50	0.527	1	1	0.459
$\bar{c}$	* Mean aerodynamic chord, m (in)	1.225 (48.22)	1.178 (46.38)	0.871 (34.29)	0.871 (34.29)	1.201 (47.30)
$y_{\bar{c}}$	** Lateral position of mean aerodynamic chord, m (in)	2.709 (106.67)	2.46 (96.85)	1.033 (40.68)	0.932 (36.69)	0.334 (13.15)
Γ	Dihedral angle, deg.	7	7	0	0	-
Λ_{le}	Leading-edge sweep, deg.	3.67	3.67	0	0	40.0
$\Lambda_{c/4}$	Sweep of c/4 line, deg.	1.835	1.835	0	0	34.5
$\Lambda_{c/2}$	Sweep of c/2 line, deg.	0	0	0	0	29.0

$$* \; \bar{c} = \frac{2}{3} c_r \left(\frac{1 + \lambda + \lambda^2}{1 + \lambda} \right)$$

$$** \; y_{\bar{c}} = \frac{1}{3} \left(\frac{1 + 2\lambda}{1 + \lambda} \right) \frac{b}{2}$$

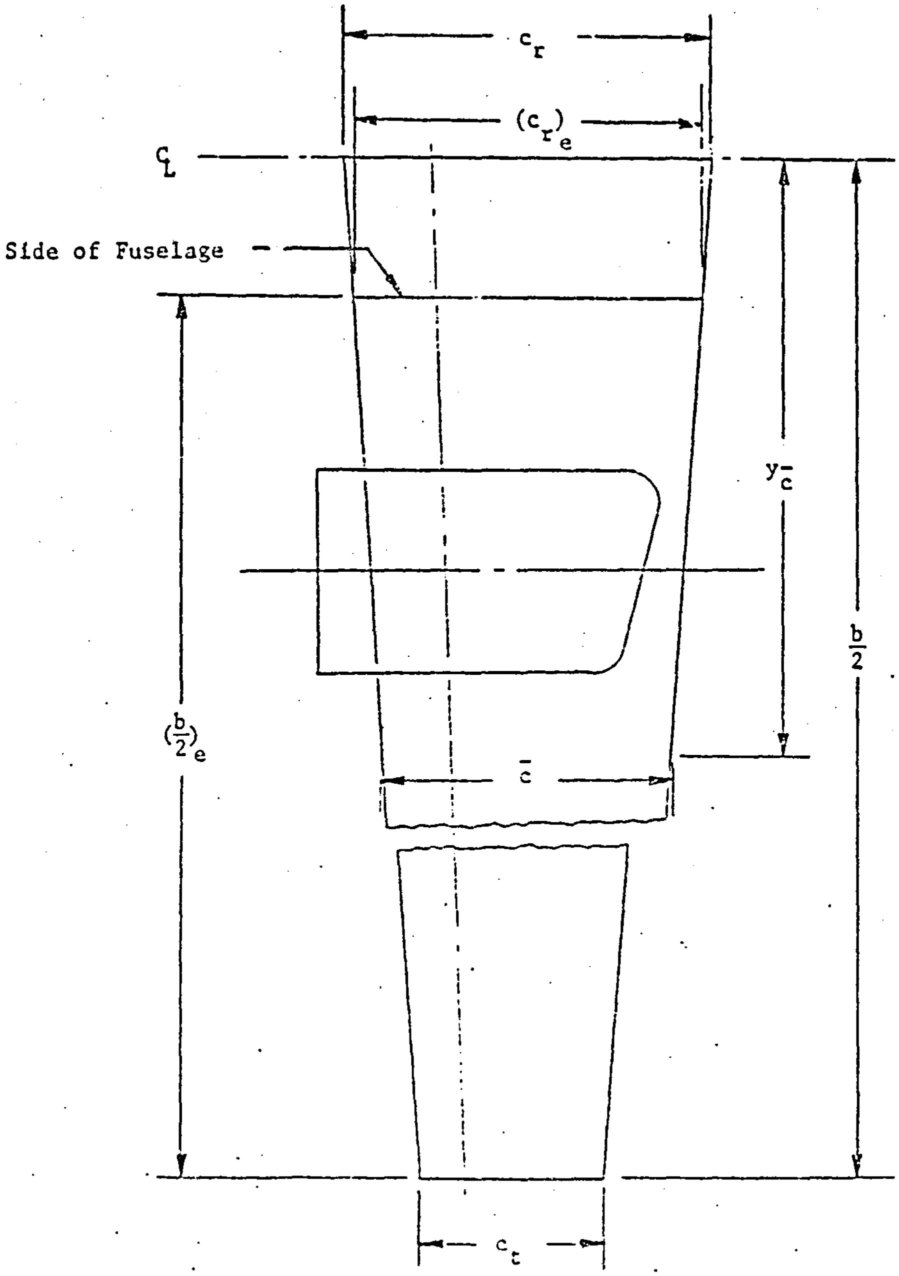

Figure 2.1.1: Definition sketch of wing dimensions

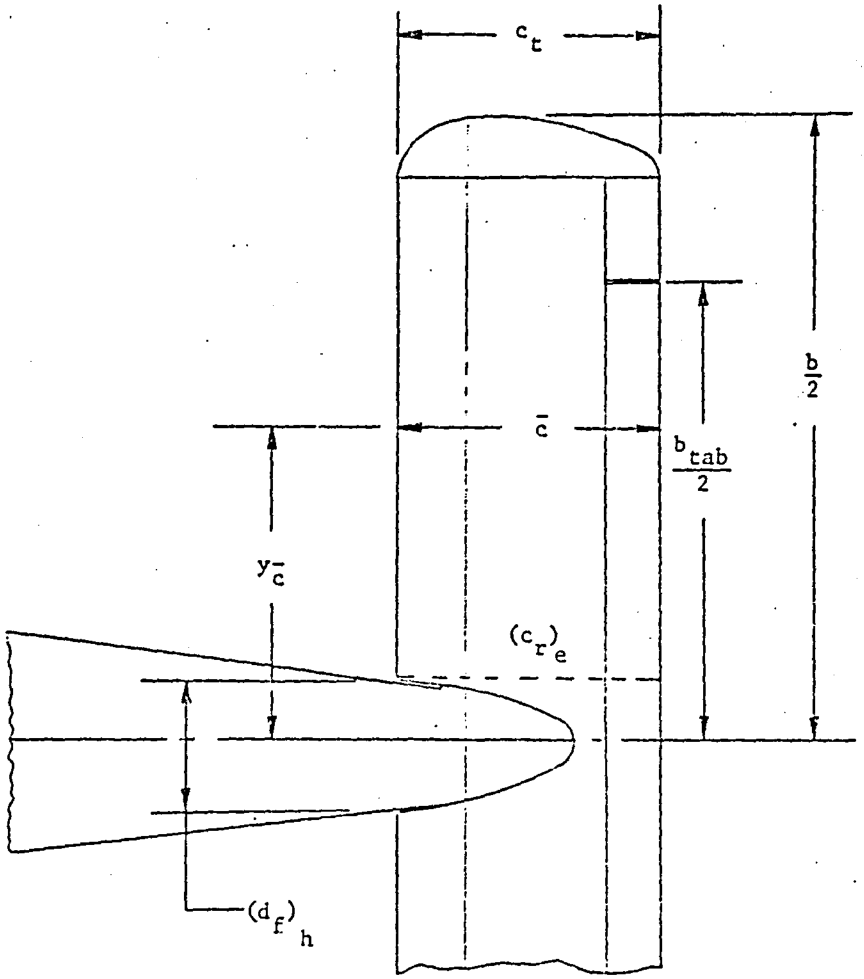

Figure 2.1.2: Definition sketch of horizontal tail dimensions

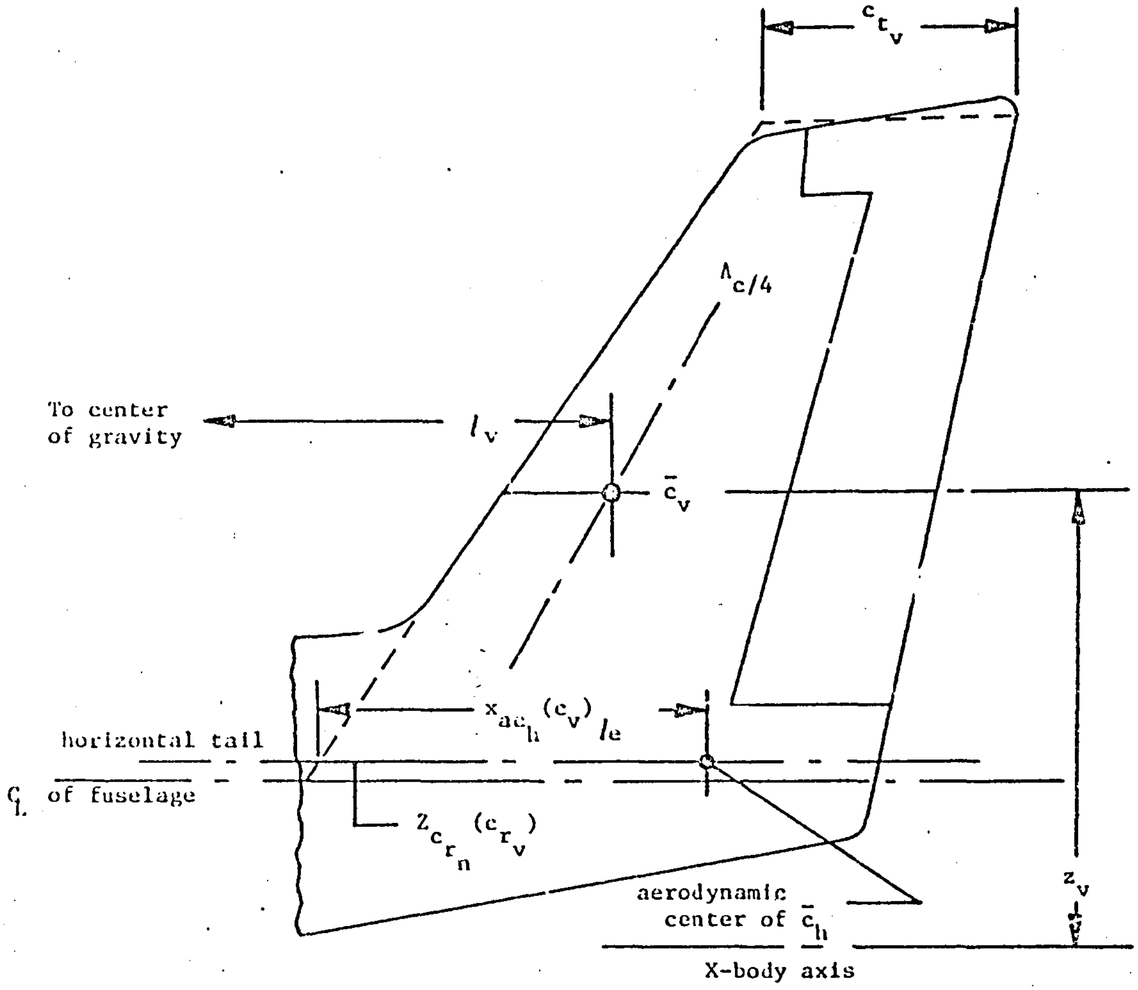

Figure 2.1.3: Definition sketch of vertical tail dimensions

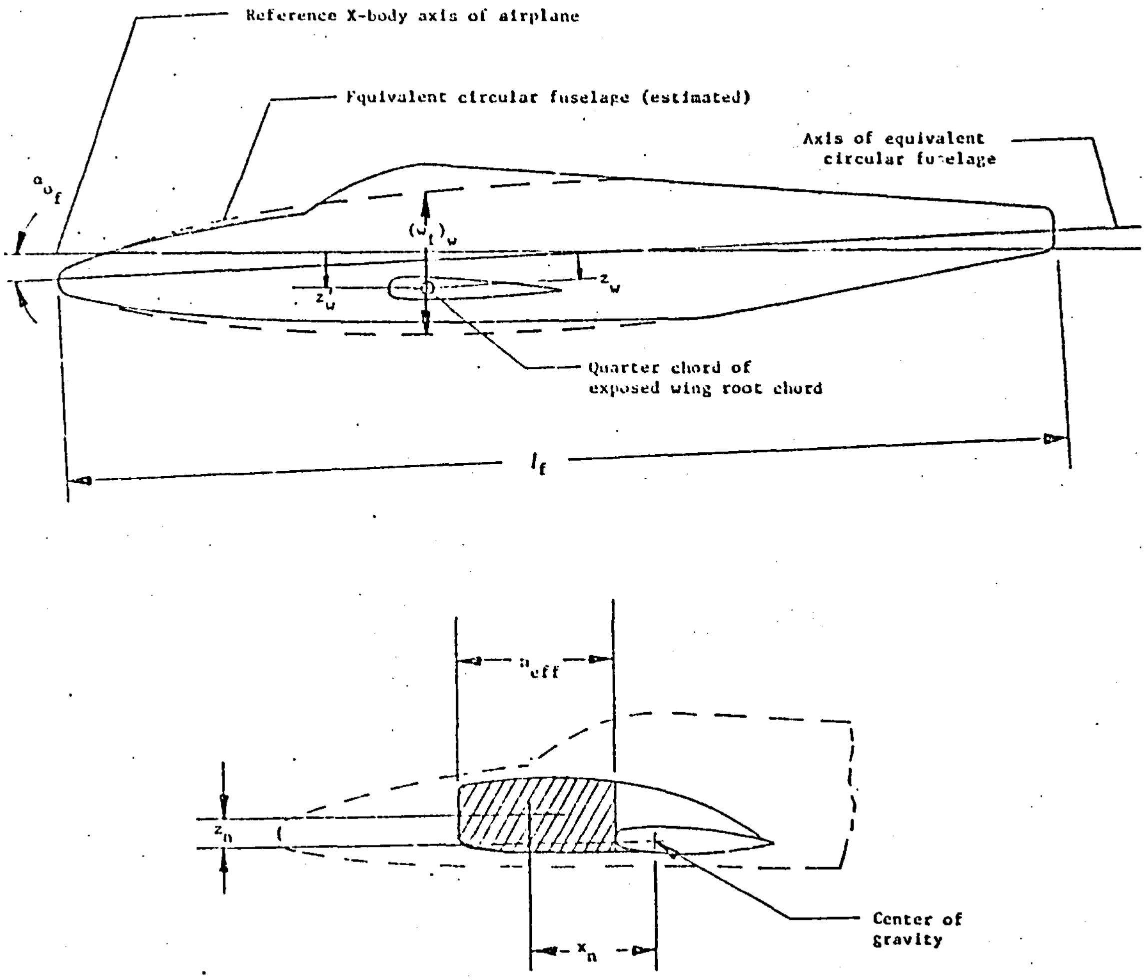

Figure 2.1.4: Definition sketch of the fuselage and nacelles

CHAPTER 3

PRESENTATION OF RESULTS

In this chapter, the predicted lateral-directional characteristics of the ATLIT airplane will be compared with full-scale wind tunnel data of Reference 2.

3.1 Sideslip Derivatives, C_{Y_β}, C_{n_β}, C_{ℓ_β}

The methods used in predicting the sideslip derivatives of the ATLIT airplane are presented in Sections 4.1 to 4.3. In Figures 3.1.1 to 3.1.6 the predicted derivatives C_{Y_β}, C_{n_β}, and C_{ℓ_β} are presented and compared with full-scale wind tunnel data for both propellers off and power-on.

Figures 3.1.1 and 3.1.2 show the propeller off and power-on C_{Y_β}. In general the results show good agreement, although the effect of angle of attack has not been properly accounted for--especially for the power-off case. It is felt that the angle of attack effect on the fuselage and fuselage-vertical tail combination has not been accounted for.

The C_{n_β} of the full-scale wind tunnel test shows a strong variation with angle of attack which the theoretical methods did not predict. While the average values agree fairly well, the predictions show a basically linear change in C_{n_β} with angle of attack. With power on, the prediction is even worse, as the wind tunnel C_{n_β} varied even more with angle of attack. As is discussed in Section 4.2.2, the wing position plays an important role in the fuselage contribution to C_{n_β}. However, there is not enough data available to account accurately for this factor.

Figures 3.1.5 and 3.1.6 show the propellers off and power on C_{ℓ_β} prediction compared with wind tunnel data. For the propellers off case the prediction is somewhat high, but the variation with angle of attack agrees with wind tunnel results. With power on, the wind tunnel tests show a more pronounced variation with angle of attack. At the low angles of attack the prediction is not very good, but it improves as the angle of attack is increased.

3.2 Control Derivatives

The control derivatives for the spoiler and the rudder are predicted in Sections 4.4 and 4.5. Figure 3.2.1 presents the spoiler effectiveness for $\alpha = 0$ as a function of spoiler deflection. The predicted effectiveness is slightly higher than the wind tunnel data. Nevertheless the prediction is considered quite good, considering the general nature of the prediction method and the lack of data for this class of airplane.

Figure 3.2.2 presents the yawing moment due to spoiler deflection. Again the prediction is slightly higher than the wind tunnel data, although the overall trend is predicted quite well.

In Section 6.1.5 it is shown that the effect of power on the spoiler characteristics were significant in the wind tunnel tests; no method was found to predict this effect.

Figures 3.2.3 through 3.2.5 compare the predicted rudder derivatives with full-scale wind tunnel data. In general the predictions are not very good. The predictions show little variation with angle of attack (except, of course, for $C_{\ell_{\delta_R}}$), while the wind tunnel data exhibits considerable variation with angle of attack. There is little variation in the rudder derivatives with power in the wind tunnel data. It was assumed that there was no power effect on the predicted rudder derivatives.

3.3 Dynamic Derivatives

The dynamic derivatives of the ATLIT airplane were originally predicted for comparison with flight test data. This data is not yet available; however, the data is presented here for completeness. Power effects were only considered significant for C_{ℓ_p}. Figures 3.3.1 through 3.3.5 show the predicted derivatives as a function of angle of attack.

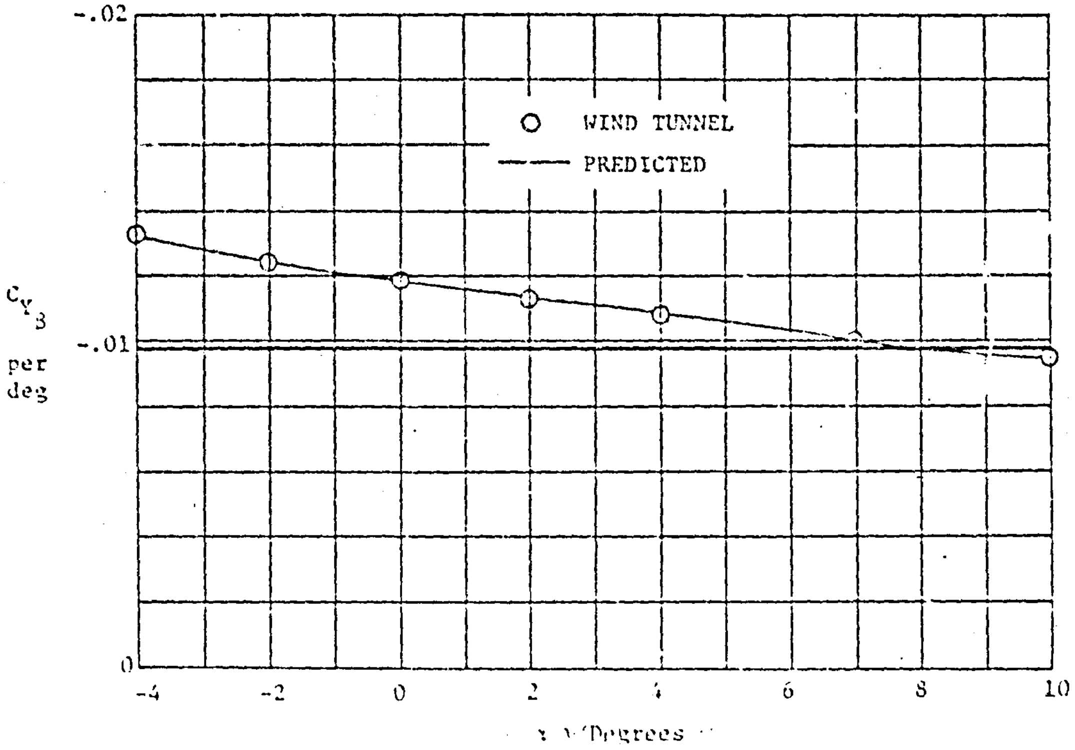

Figure 3.1.1: Comparison of predicted C_{Y_β} with full scale wind tunnel data (propellers removed, N_{Re} = 2.3 million)

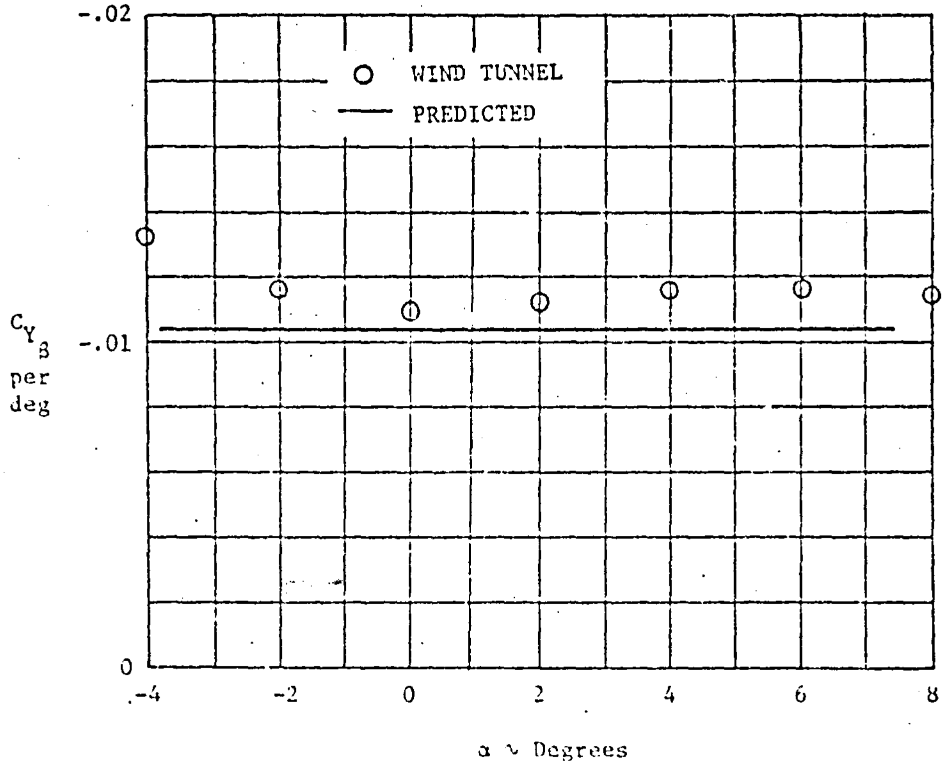

Figure 3.1.2: Comparison of predicted power-on C_{Y_β} with wind tunnel data ($T_c' = .1970$)

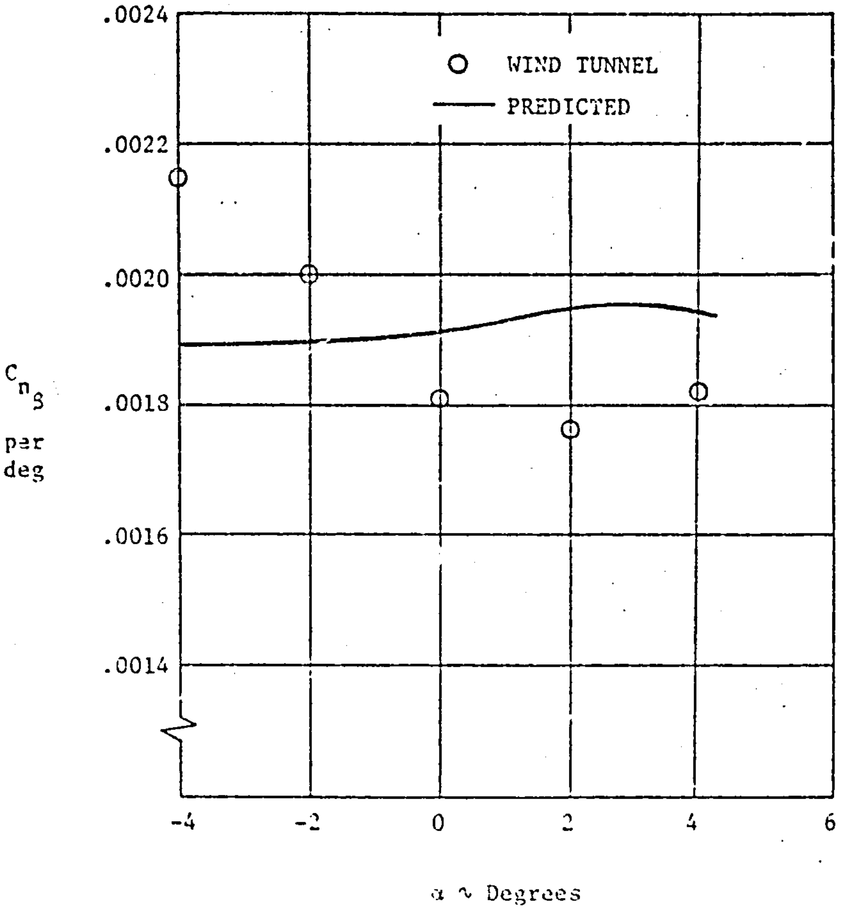

Figure 3.1.3: Comparison of predicted C_{n_β} with full scale wind tunnel data (propellers removed, N_{Re} = 2.3 million)

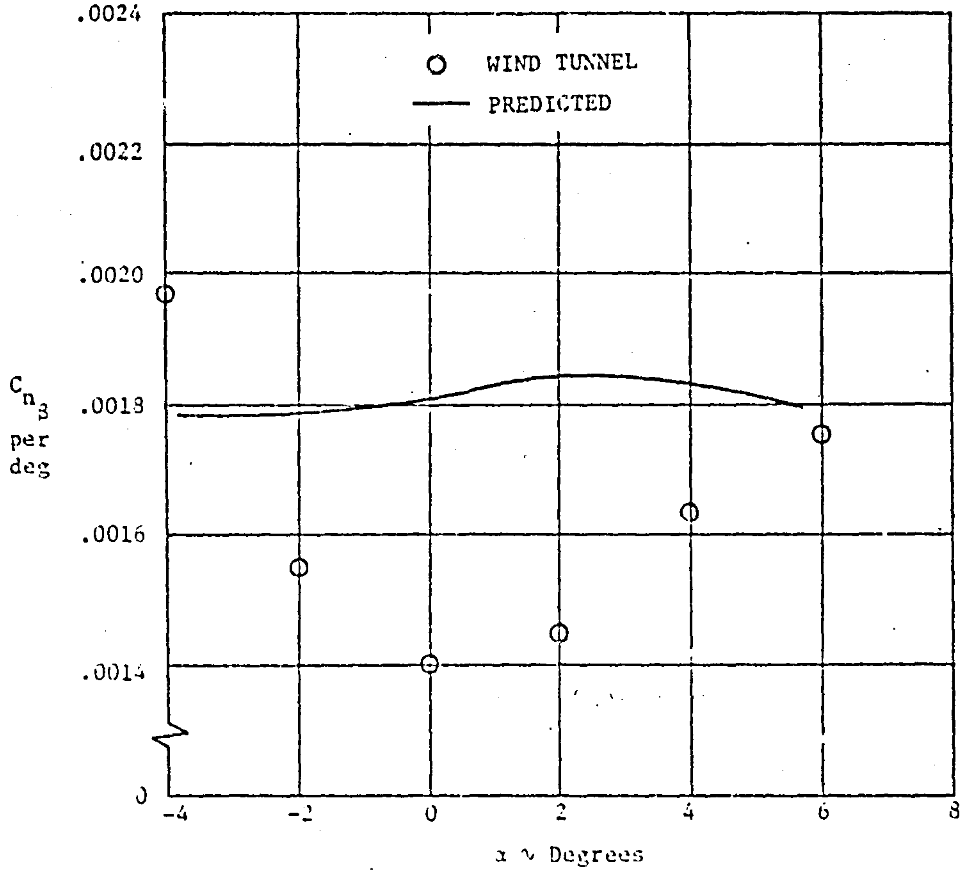

Figure 3.1.4: Comparison of predicted power-on C_{n_β} with wind tunnel data on the ATLIT Airplane (T'_c = .1970)

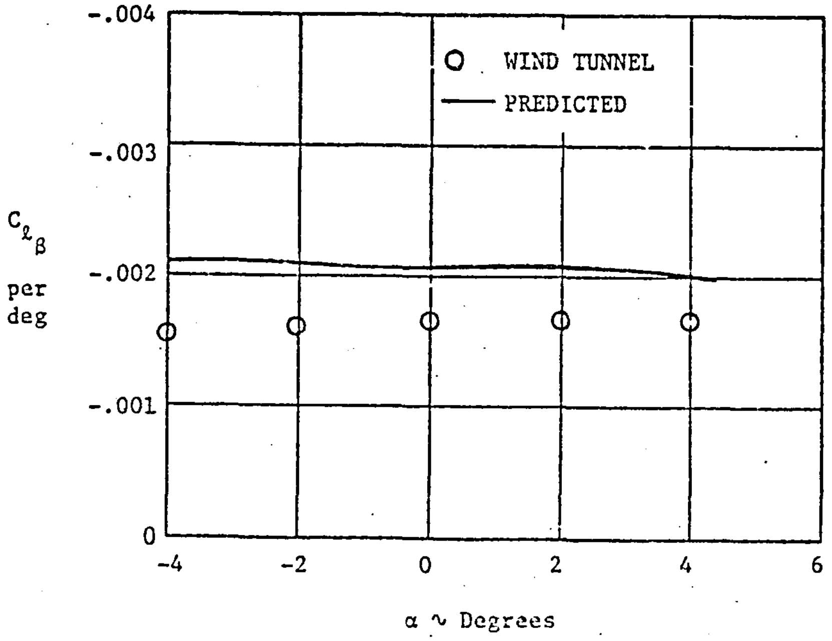

Figure 3.1.5: Comparison of predicted C_{ℓ_β} with full scale wind tunnel data (propellers removed, N_{Re} = 2.3 million)

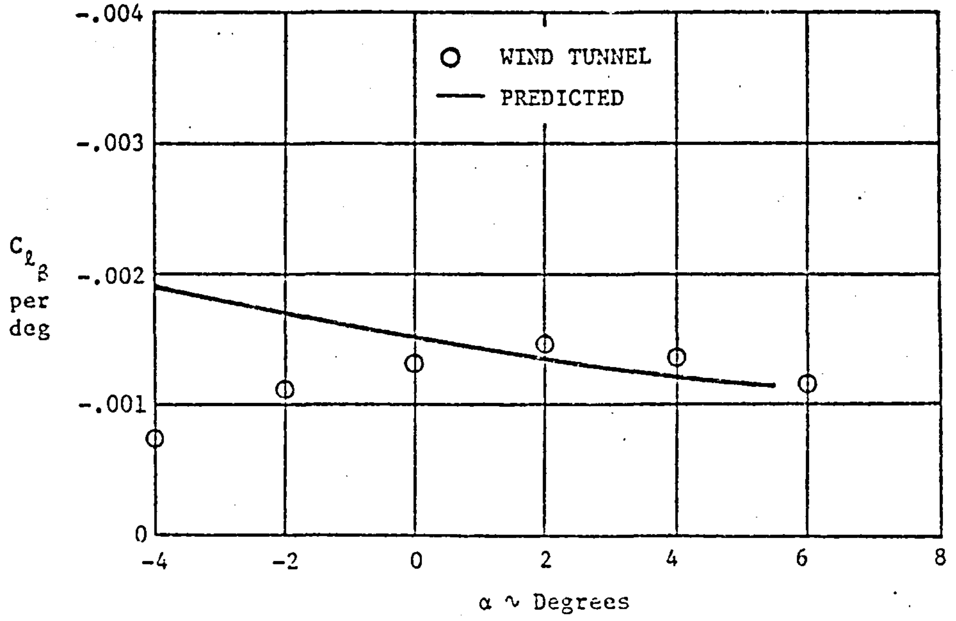

Figure 3.1.6: Comparison of predicted power-on C_{ℓ_β} with wind tunnel data on the ATLIT Airplane (T'_c = .1970)

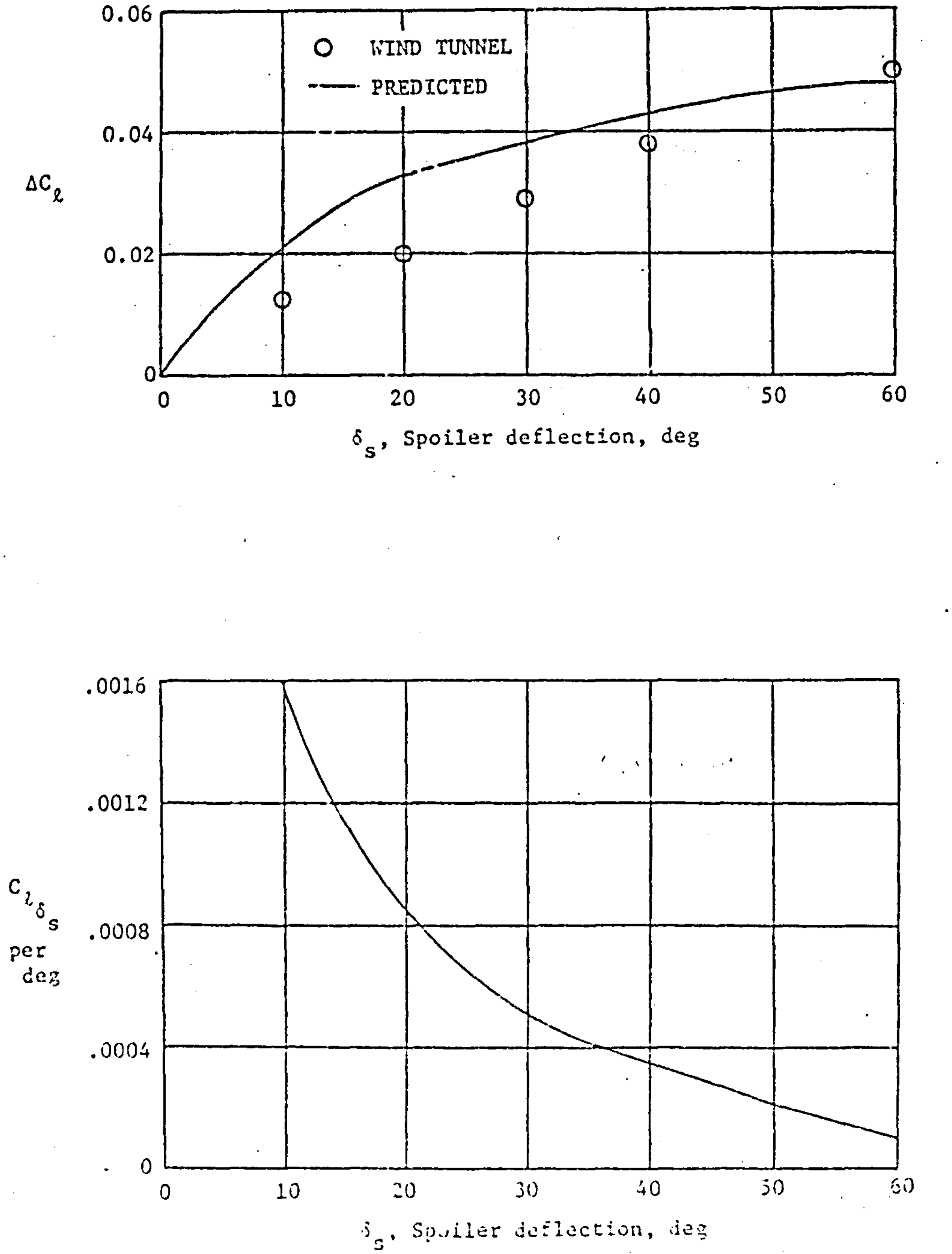

Figure 3.2.1: Comparison of predicted spoiler effectiveness with full-scale wind tunnel data (Power off; $\alpha = 0°$)

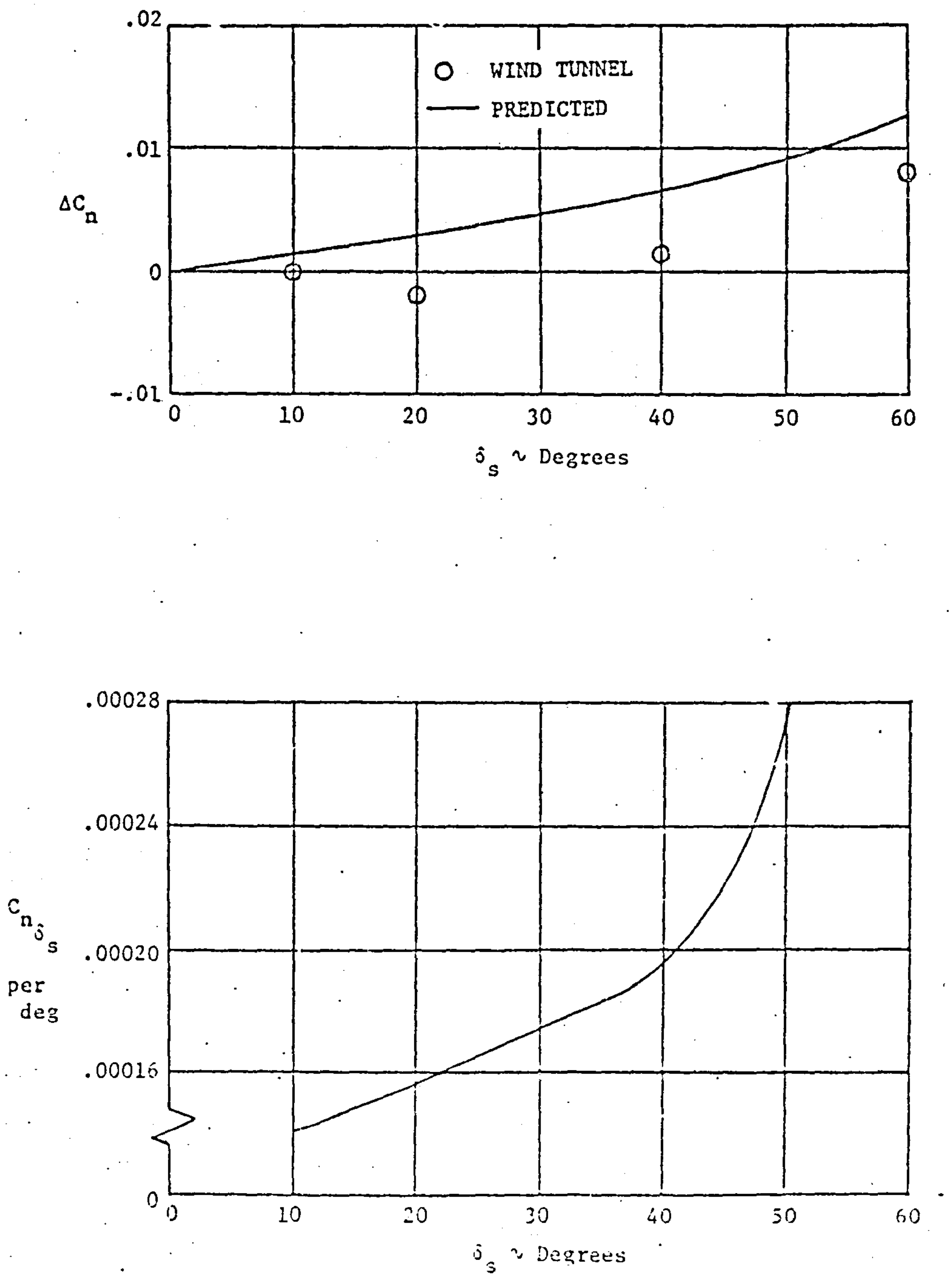

Figure 3.2.2: Comparison of predicted yaw due to spoilers with wind tunnel data (propellers removed, $\alpha=0°$).

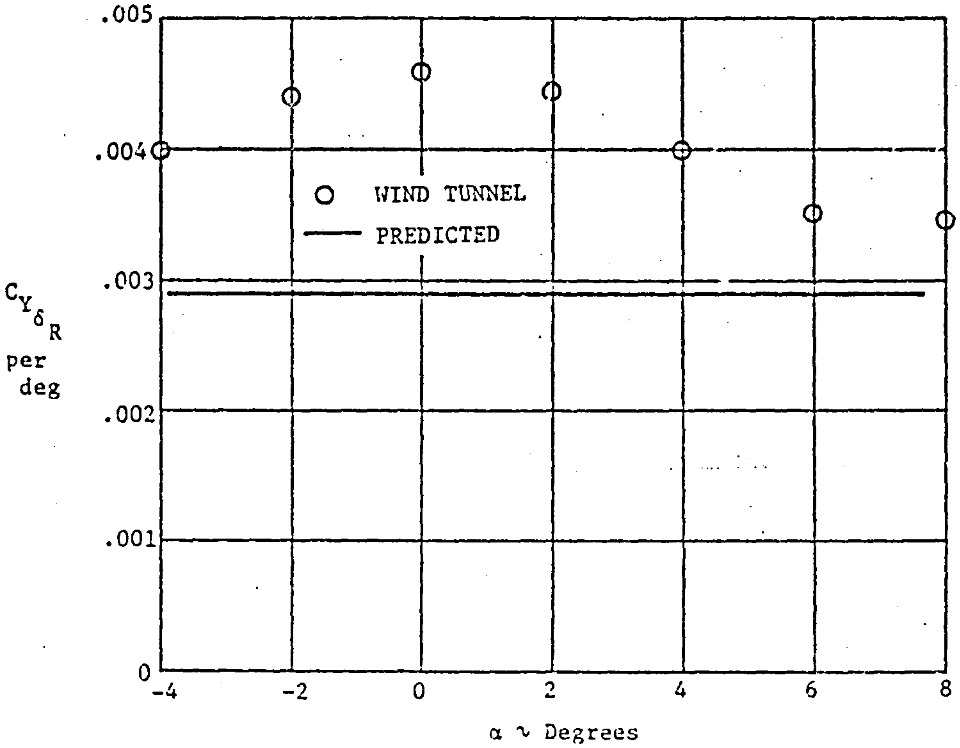

Figure 3.2.3: Comparison of predicted $C_{Y_{\delta_R}}$ with wind tunnel data (δ_R = ±10°, β = 0°)

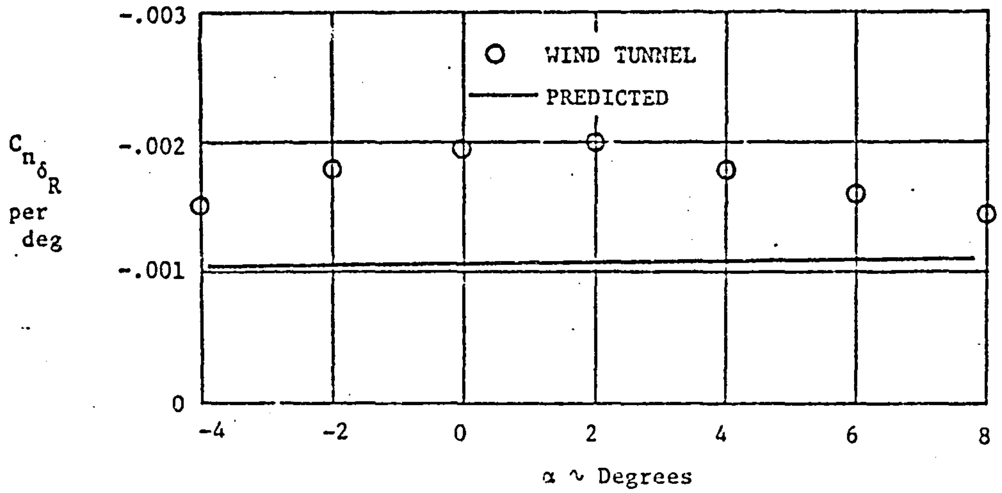

Figure 3.2.4: Comparison of predicted $C_{n_{\delta_R}}$ with wind tunnel data ($\beta = 0°$, $\delta_R = \pm 10°$)

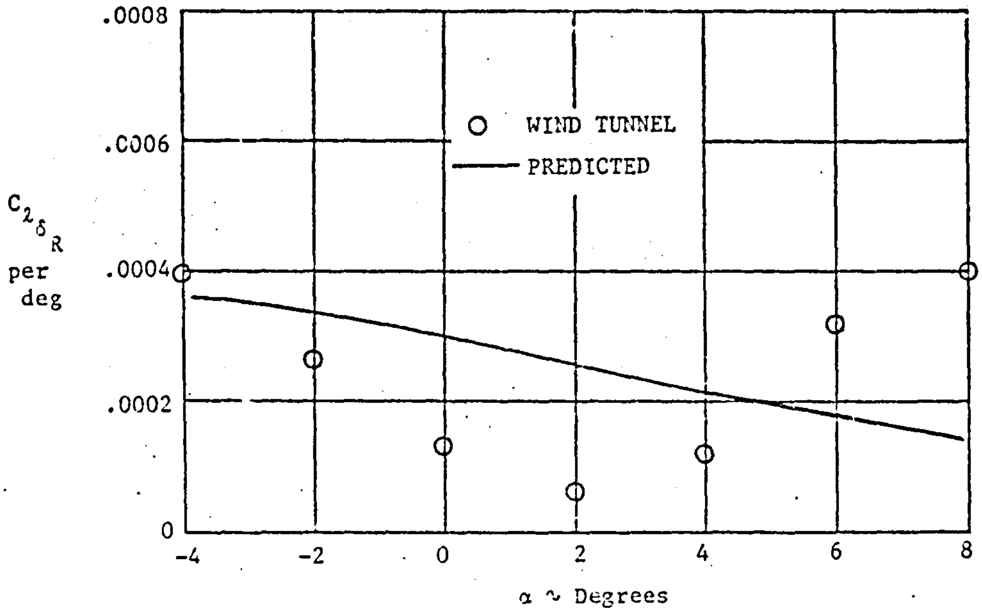

Figure 3.2.5: Comparison of predicted $C_{l_{\delta_R}}$ with wind tunnel data ($\beta = 0°$, $\delta_R = \pm 10°$)

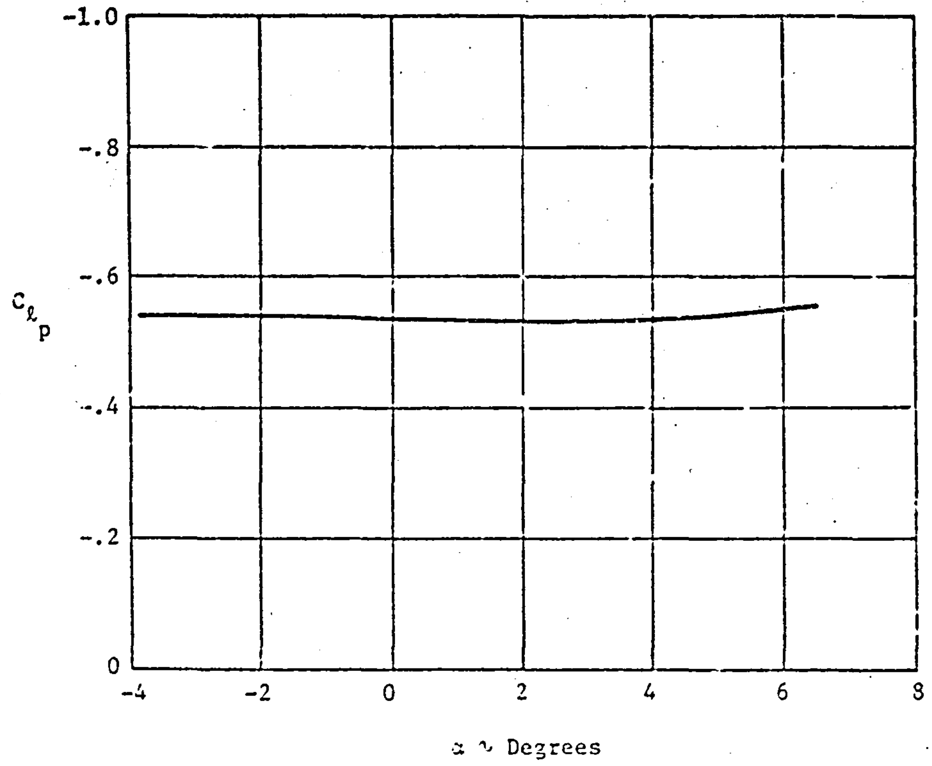

Figure 3.3.1: Predicted C_{ℓ_p} of the ATLIT Airplane (propellers removed)

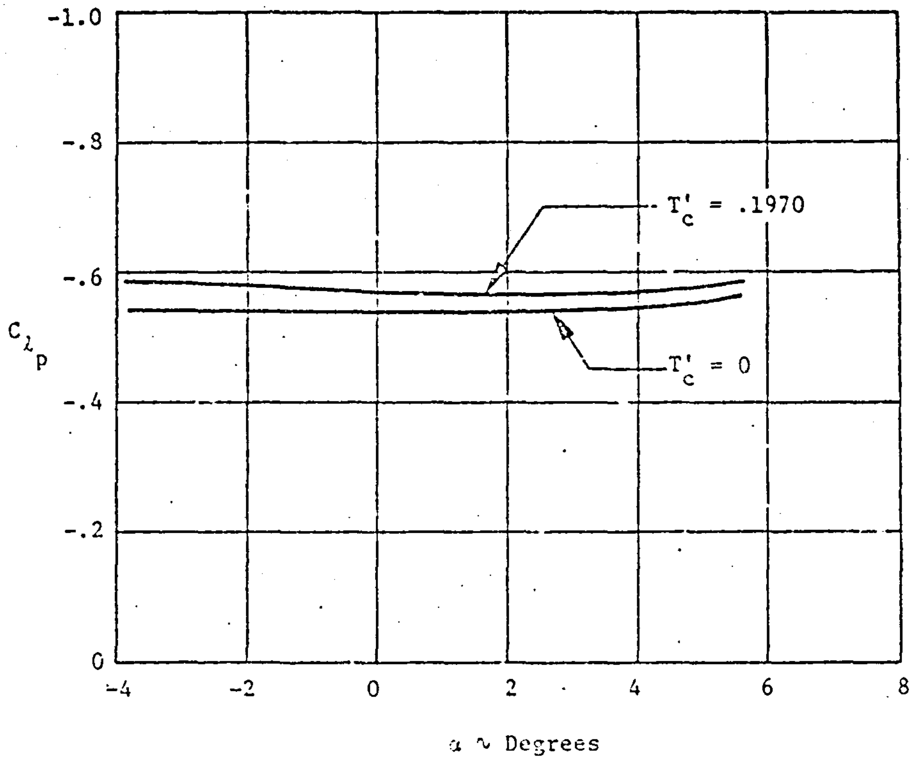

Figure 3.3.2: Effect of power on predicted C_{ℓ_p} of the ATLIT Airplane

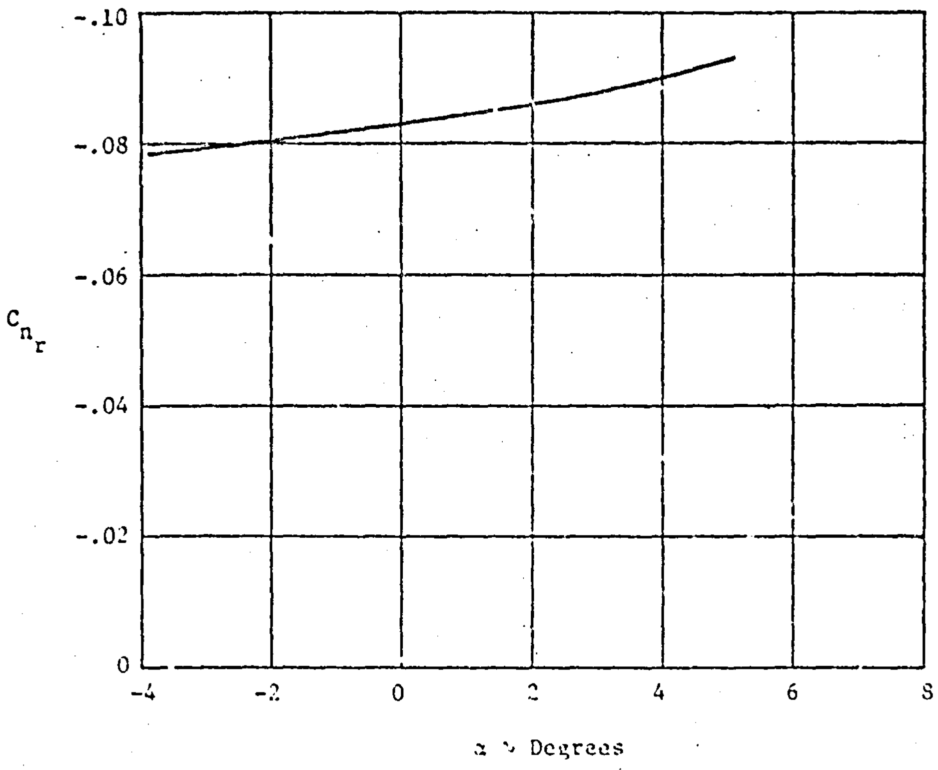

Figure 3.3.3: Predicted C_{n_r} of the ATLIT Airplane (propellers removed)

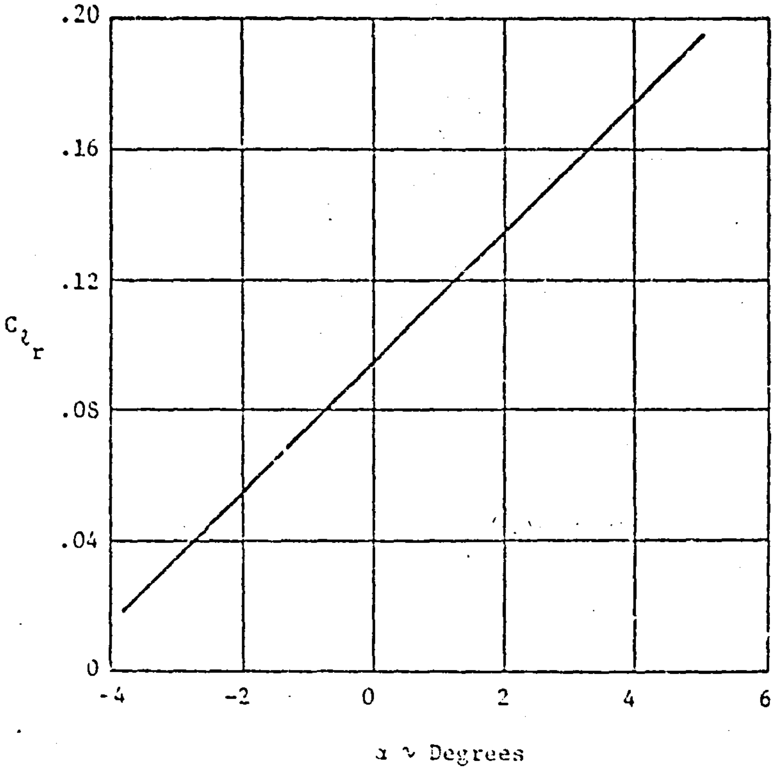

Figure 3.3.4: Predicted C_{ℓ_r} of the ATLIT Airplane (propellers removed)

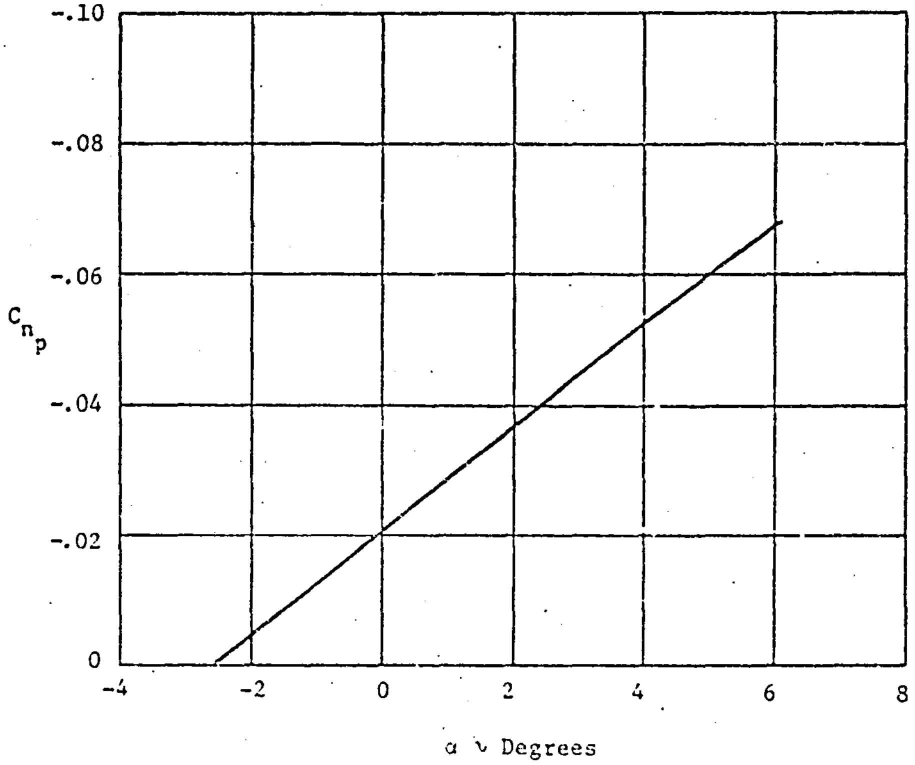

Figure 3.3.5: Predicted C_{n_p} of the ATLIT Airplane (propellers removed)

CHAPTER 4

PREDICTION OF PROPELLER-OFF STATIC STABILITY AND CONTROL CHARACTERISTICS

In this chapter the propeller-off static stability and control characteristics will be discussed. The methods of Reference 3 are used for most all predictions. However, since Reference 3 does not include methods for predicting spoiler control characteristics, Reference 4 will be used.

4.1 Side Force Derivative, C_{Y_β}

The side force due to sideslip derivative, C_{Y_β}, of the complete airplane is found by considering the contributions of the following components:

(1) Wing, including dihedral

(2) Fuselage, including wing-fuselage interference

(3) Nacelles

(4) Vertical tail, including the interference of the wing, fuselage, and horizontal tail.

4.1.1 Wing Contribution, $(C_{Y_\beta})_{w_{\Gamma=0}} + (C_{Y_\beta})_\Gamma$

The wing contribution to C_{Y_β} with no dihedral is found from Equation 4.1.1.1 from Reference 3. This expression is valid for low subsonic mach numbers and includes compressibility effects.

$$(C_{Y_\beta})_{w_{\Gamma=0}} = \frac{C_{L_w}^{2}}{57.3} \quad \frac{6 \tan (\Lambda_{c/4})_w \sin (\Lambda_{c/4})_w}{\pi A_w [A_w B_2 + 4 \cos (\Lambda_{c/4})_w]} \qquad (4.1.1.1)$$

where

C_{L_w} is the wing alone lift coefficient obtained from Figure 4.1.1.1

A_w is the aspect ratio of the wing

$\Lambda_{c/4}$ is the quarter-chord sweep of the wing

$B_2 = \sqrt{1-M^2\cos^2\Lambda_{c/4}}$

where M is the Mach Number.

For typical general aviation aircraft with essentially straight wings and moderate aspect ratio ($A_w > 6$), this contribution is insignificant. For the ATLIT airplane

$$(C_{Y_\beta})_{w_{\Gamma=0}} = 2.32 \times 10^{-7}\ C_{L_w}^{\ 2} \text{ per deg.}$$

The increment in side-force derivative due to wing dihedral may be approximated at low subsonic speeds by the following equation from Reference 3:

$$(C_{Y_\beta})_\Gamma = -0.0001\ \Gamma \qquad (4.1.1.3)$$

For the ATLIT airplane the wing dihedral angle Γ is 7.0°. Therefore,

$$(C_{Y_\beta})_\Gamma = -0.0007 \text{ per deg.}$$

The summary calculation of the wing contributions to C_{Y_β} are given in Table 4.1.1.1.

4.1.2 Fuselage Contribution to C_{Y_β}

The fuselage side-force due to sideslip contribution is the result of the side forces produced by the body and the wing-body interference effects. The fuselage alone is the main contributor and is affected by the size and shape of the body. The wing-body interference contribution is considered to be only a function of wing location. The total fuselage contribution to C_{Y_β} at subsonic Mach numbers is given by Equation 4.1.2.1 from Reference 3 (based on S_w).

$$(C_{Y_\beta})_f = K_1 (C_{Y_\beta})_{f_{\bar{v}^{2/3}}} \left(\frac{\bar{v}^{2/3}}{S_w}\right) \text{ per deg} \qquad (4.1.2.1)$$

where

$(C_{Y_\beta})_{f_{\bar{v}^{2/3}}}$ is the contribution of the fuselage only based on two-thirds of the fuselage volume and is equal to but opposite in sign to the potential flow part of the fuselage lift curve slope from Section 4.3 of Reference 1.

K_1 is the wing-body interference factor obtained from Figure 4.1.2.1

Table 4.1.2.1 summarizes the effects of the fuselage on C_{Y_β}. For the ATLIT airplane

$$(C_{Y_\beta})_f = -.00299 \text{ per deg.}$$

4.1.3 Nacelle Contribution to C_{Y_β}

Due to a lack of definitive methods for calculating the contribution of the nacelles to C_{Y_β}, Reference 3 presents the following empirical procedures:

(1) The effective nacelle length is considered to extend only to the wing leading edge (see Figure 2.1.4).

(2) The nacelle contribution is approximated from Equation 4.1.3.1 for bodies of circular cross section (based on S_w).

$$(C_{Y_\beta})_n = -n_n \frac{2(k_2-k_1)(S_{x_n})_{max}}{57.3\, S_w} \text{ per deg} \qquad (4.1.3.1)$$

where

n_n is the number of nacelles

S_{x_n} is the effective cross section area equal to a circular cross section with a diameter equal to the maximum depth of the nacelle, d_n, from Figure 2.1.4.

(k_2-k_1) is the reduced mass factor obtained from Figure 4.1.3.1 as a function of effective length and maximum depth.

(3) To account for flow interference effects, the $(C_{Y_\beta})_n$ predicted by Equation 4.1.3.1 is reduced by one-third.

$$(C_{Y_\beta})_n = -2/3 \; n_n \left[\frac{2(k_2-k_1)(S_{x_n})_{max}}{57.3 \; S_w} \right] \text{ per deg} \qquad (4.1.3.2)$$

The calculations for the ATLIT airplane are summarized in Table 4.1.3.1. The total nacelle contribution is

$$(C_{Y_\beta})_n = -.00048 \text{ per deg}$$

4.1.4 Vertical-Tail Contributions to C_{Y_β}

The contribution of the vertical tail to C_{Y_β} is affected by the location of the horizontal tail, the fuselage crossflow at the tail, and the wing-body induced sidewash.

The horizontal tail can serve to increase the loading on the vertical tail by the so-called "end plate effect" when the horizontal tail is at a relatively high or low position. For mid span positions the effect of the horizontal tail is insignificant.

The effect of the fuselage in sideslip is to increase the local cross-flow velocity across the top of the body. This increased velocity causes an increase in vertical tail effectiveness.

As the sidewash due to a yawed wing is small, the primary sidewash contribution is from the body and arises from the body vortex system produced in sideslip. This vortex system produces lateral velocity components which affect the vertical tail.

The method of Reference 3 accounts for the horizontal tail and cross flow factors by computing an effective aspect ratio. The effective aspect ratio of the vertical tail is

$$A_{v_{eff}} = A_v\left(\frac{A_{v(f)}}{A_v}\right)\left\{1 + K_h\left[\frac{A_{v(fh)}}{A_{v(f)}} - 1\right]\right\} \qquad (4.1.4.1)$$

where

A_v is the actual geometric aspect ratio of the vertical tail

$\frac{A_{v(f)}}{A_v}$ is the ratio of the aspect ratio of the vertical tail in the presence of the body to that of the isolated vertical tail, obtained from Figure 4.1.4.1(a)

$\frac{A_{v(fh)}}{A_{v(f)}}$ is the ratio of the aspect ratio of the vertical tail in the presence of the horizontal tail and the fuselage to the aspect ratio of the vertical tail in the presence of the fuselage only, obtained from Figure 4.1.4.1(b)

K_h is a factor which accounts for the relative size of the vertical and horizontal tails, obtained from Figure 4.1.4.2

Table 4.1.4.1(a) shows the summary calculations to obtain the effective aspect ratio of the ATLIT airplane. It shows an effective aspect ratio of 2.46 compared to a geometric aspect ratio of 1.19.

The lift curve slope of the vertical tail is found using the standard Polhamus equation (4.1.4.2) by using the effective aspect ratio (based on effective vertical tail area, S_v)

$$(C_{L_\alpha})_{v(hf)} = \frac{2\pi A_{v_{eff}}}{2 + \sqrt{\frac{A_{v_{eff}}}{k_v^2}\left[B_1^2 + \tan^2(\Lambda_{c/2})_v\right] + 4}} \qquad (4.1.4.2)$$

where

$$k_v = \frac{(C_{l_\alpha})_v}{2\pi} \qquad (4.1.4.3)$$

$(C_{l_\alpha})_v$ is the section lift curve slope of the vertical tail obtained from Section 4.1 of Reference 1.

$$B_1^2 = 1 - M^2 \qquad (4.1.4.4)$$

M is the Mach Number

$(\Lambda_{c/2})_v$ is the mid-chord sweep of the vertical tail.

Table 4.1.4.1(b) shows the summary calculations. For the ATLIT airplane (based on S_v)

$$(C_{L_\alpha})_{v(fh)} = .0494 \text{ per deg}$$

The total vertical tail contribution to C_{Y_β} is given in Equation 4.1.4.5 from Reference 3. It modifies the vertical tail lift curve slope to account for wing wake and body sidewash.

$$(C_{Y_\beta})_{v(wfh)} = -k_1'(C_{L_\alpha})_{v(fh)}\left(1 + \frac{\partial\sigma}{\partial\beta}\right)\frac{\bar{q}_v}{\bar{q}_\infty}\frac{S_v}{S_w} \qquad (4.1.4.5)$$

where

k_1' is factor which accounts for the relative size of the body near the vertical tail to the size of the tail, from Figure 4.1.4.3.

$$\left(1 + \frac{\partial\sigma}{\partial\beta}\right)\frac{\bar{q}_v}{\bar{q}_\infty} = 0.725 + 3.06\,\frac{S_v/S_w}{1 + \cos(\Lambda c/4)_w} + 0.4\,\frac{z_w}{(w_f)_w} + 0.009\,A_w \qquad (4.1.4.6)$$

where

$(\Lambda_{c/4})_v$ is the quarter-chord sweep of the vertical tail

z_w is the vertical distance from the centerline of the equivalent fuselage to the quarter-chord point of the root chord of the exposed wing panel, obtained from Figure 2.1.4.

$(w_f)_w$ is the depth of the equivalent circular fuselage at the wing, obtained from Figure 2.1.4.

Table 4.1.4.1(c) shows the summary calculations used to find the vertical tail contribution to C_{Y_β}. For the ATLIT airplane (based on S_w)

$$(C_{Y_\beta})_{v(wfh)} = -0.0056 \text{ per deg}$$

4.1.5 C_{Y_β} of the ATLIT Airplane

The total side-force derivative of the complete airplane (propellers off) is

$$C_{Y_\beta} = (C_{Y_\beta})_{w_{\Gamma=0}} + (C_{Y_\beta})_\Gamma + (C_{Y_\beta})_f + (C_{Y_\beta})_n + (C_{Y_\beta})_{v(wfn)} \qquad (4.1.5.1)$$

Table 4.1.5.1 summarizes the contribution of each component. For the ATLIT airplane

$$(C_{Y_\beta})_{\substack{\text{prop}\\ \text{off}}} = -0.0098 \text{ per deg}$$

The predicted and experimental C_{Y_β} is shown in Figure 4.1.5.1. In general it shows fairly good agreement, although it is obvious that the effect of angle of attack has not been properly accounted for. These effects are probably in the wing-body interference and sidewash contributions.

Table 4.1.1.1: Wing Contribution to C_{Y_β}

Symbol	Description	Reference	Magnitude
M	Mach number	-	0.081
A_w	Wing aspect ratio	Table 2.1.1	10.32
$(\Lambda_{c/4})_w$	Wing quarter-chord sweep angle, deg	Table 2.1.1	1.835
Γ	Geometric dihedral angle, deg	Table 2.1.1	7
C_{L_w}	Wing lift coefficient	Figure 4.1.1.1	variable
Summary: $(C_{Y_\beta})_{w_{\Gamma=0}} + (C_{Y_\beta})_\Gamma = 2.32 \times 10^{-7}\ C_{L_w}^2 - 0.0007$ per deg			

Table 4.1.2.1: Fuselage Contribution to C_{Y_β}

Symbol	Description	Reference	Magnitude
$\frac{2z}{(w_f)_w}$	Wing-body position parameter	Figure 2.1.4	0.326
K_i	Wing-body interference factor	Figure 4.1.2.1	1.16
$(C_{Y_\beta})_{f_{\bar{V}^{2/3}}} \bar{V}^{2/3}$	C_{Y_β} of equivalent circular fuselage based on 2/3 power of fuselage volume [considered aqual to the negative of the potential flow part of $(C_{L_\alpha})_{f_{\bar{V}^{2/3}}}$] times the fuselage volume to 2/3 power	Table 4.3.1 Reference 1	0.002574
S_w	Wing reference area, m^2 (ft^2)	Table 2.1.1	14.40 (155.0)
Summary: $(C_{Y_\beta})_f = -0.002986$ per deg			

Table 4.1.3.1: Nacelle Contribution to C_{Y_β}

Symbol	Description	Reference	Magnitude
n_n	Number of nacelles	-	2
S_w	Wing reference area, m^2 (ft^2)	Table 2.1.1	14.40 (155.0)
$(S_{x_n})_{max}$	Effective nacelle cross-section area, m^2 (ft^2)	Figure 2.1.4	0.292 (3.14)
$\frac{l_n}{d_n}$	Effective nacelle fineness ratio	Figure 2.1.4	2.08
$(k_2 - k_1)$	Nacelle reduced mass factor	Figure 4.1.3.1	0.504

Summary: $(C_{Y_\beta})_n = -0.000476$ per deg

4.1.4.1: Vertical Tail Contribution to C_{Y_β}

(a) Effective Aspect Ratio

Symbol	Description	Reference	Magnitude
S_h	Horizontal tail area, m^2 (ft^2)	Table 2.1	3.60 (38.7)
S_v	Vertical tail area, m^2 (ft^2)	Table 2.1	1.85 (19.9)
b_v	Vertical tail span, m (ft)	Table 2.1	1.52 (5.0)
A_v	Vertical tail aspect ratio	Table 2.1	1.19
$(c_v)_h$	Vertical tail chord at horizontal tail, m (ft)	Figure 2.1.5	1.80 (5.92)
$x_{ac_h}(c_v)/_e$	Distance from leading edge of vertical tail to a.c. of horizontal tail, in plane of horizontal tail, m (ft)	Figure 2.1.5	1.45 (4.75)
$z_{c_{r_h}}(c_{r_v})$	Distance from root chord of vertical tail to root chord of horizontal tail. m (ft)	Figure 2.1.5	-0.051 (-0.167)
$(d_f)_v$	Depth of fuselage at quarter-root chord of vertical tail, m (ft)	Figure 2.1.5	0.661 (2.17)
$\frac{A_v(f)}{A_v}$	Ratio of vertical tail aspect ratio in presence of fuselage to isolated vertical tail aspect ratio	Figure 4.1.4.1 (a)	1.6
$\frac{A_v(fh)}{A_v(f)}$	Ratio of vertical tail aspect ratio in presence of fuselage and horizontal tail to aspect ratio of tail in presence of fuselage alone	Figure 4.1.4.1 (b)	1.26
K_h	Relative tail size factor	Figure 4.1.4.2	1.12

Summary: $A_{v_{eff}} = 2.46$

Table 4.1.4.1: (continued)
(b) Vertical Tail Lift Curve Slope

Symbol	Description	Reference	Magnitude
M	Mach number	-	0.081
β_1^2	$1 - M^2$	Equation 4.1.4.4	0.993
$A_{v_{eff}}$	Effective vertical tail aspect ratio	Table 4.1.4.1 (a)	2.46
$(\Lambda_{c/2})_v$	Vertical tail half-chord sweepback, deg	Table 2.1.1	29.0
$(C_{l_\alpha})_v$	Vertical tail section lift curve slope, per rad	Table 4.1.2 Reference 1	6.246
k_v	$\frac{(C_{l_\alpha})_v}{2\pi}$	Equation 4.1.4.3	0.988

Summary: $(C_{L_\alpha})_{v(th)} = 0.0494$ per deg = 2.83 per rad (based on S_v)

Table 4.1.4.1: Concluded
(c) Vertical Tail Contribution to C_{Y_β}

Symbol	Description	Reference	Magnitude
S_w	Wing reference-area, m^2 (ft^2)	Table 2.1	14.40 (155.0)
$(\Lambda_{c/4})_v$	Vertical tail quarter-chord sweep angle, deg	Table 2.1.1	34.5
z_w	Distance from equivalent fuselage centerline	Figure 2.1.4	0.199 (0.653)
$(w_f)_w$	Width of equivalent fuselage at wing, m (ft)	Figure 2.1.4	1.19 (3.92)
A_w	Wing aspect ratio	Table 2.1	10.32
$(1 + \frac{\partial\sigma}{\partial\beta})\frac{\bar{q}_v}{\bar{q}_\infty}$	Wing wake and fuselage side wash factor	Equation 4.1.4.6	1.097
k_1'	Relative body size to tail size parameter	Figure 4.1.4.3	0.80
Summary: $(C_{Y_\beta})_{v(wfh)}$ = -0.0056 per deg = -0.319 per rad (based on S_w)			

Table 4.1.5.1: C_{Y_β} of the ATLIT Airplane

Symbol	Description	Reference	Magnitude
$(C_{Y_\beta})_{w_{\Gamma=0}}$	Wing contribution without dihedral, per deg	Table 4.1.1.1	2.32×10^{-7} $C_{L_w}^{2}$
$(C_{Y_\beta})_{\Gamma}$	Increment due to dihedral, per deg	Table 4.1.1.1	-0.0007
$(C_{Y_\beta})_{f}$	Fuselage contribution, per deg	Table 4.1.2.1	-0.00299
$(C_{Y_\beta})_{n}$	Nacelle contribution, per deg	Table 4.1.3.1	-0.000476
$(C_{Y_\beta})_{v(wfn)}$	Vertical tail contribution with interference accounted for, per deg	Table 4.1.4.1(c)	-0.0056

Summary: $(C_{Y_\beta})_{\substack{prop\\off}} = -0.00977$ per deg

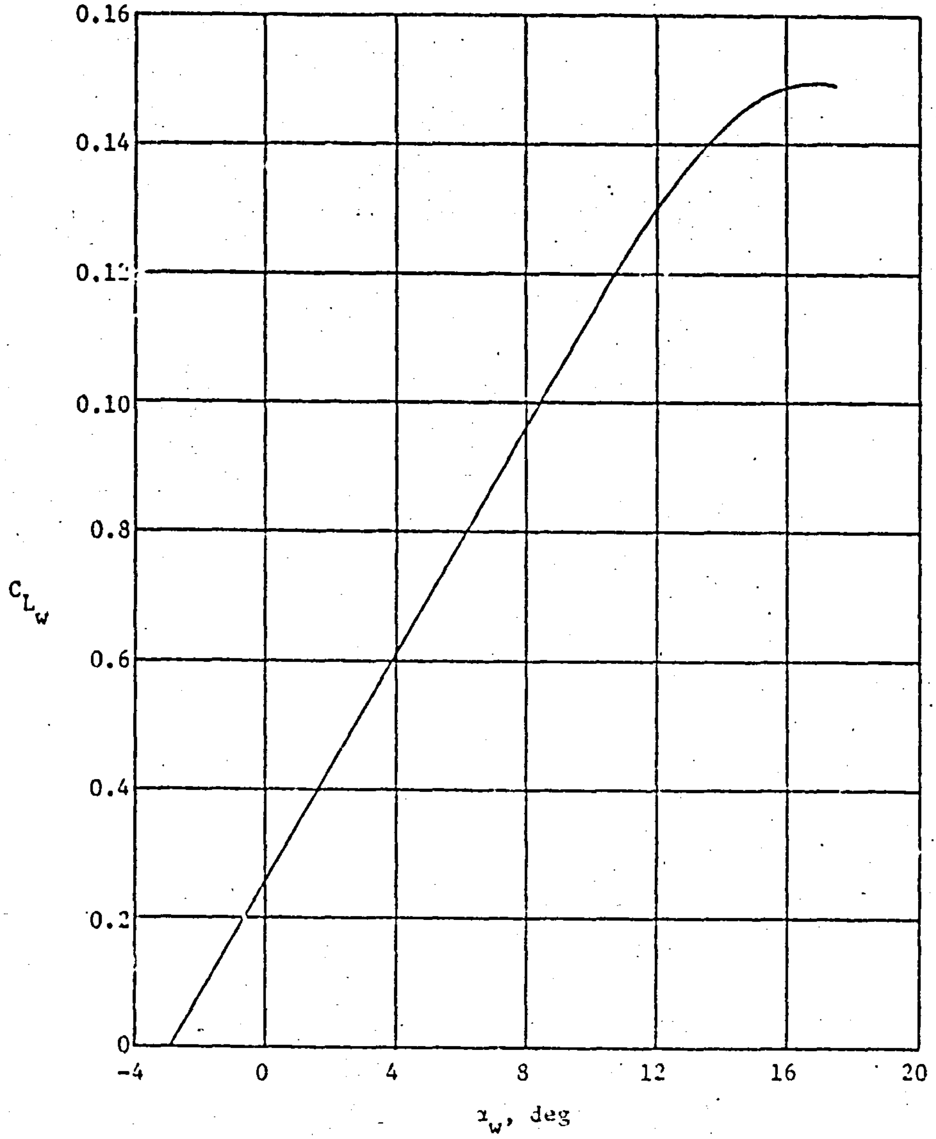

Figure 4.1.1.1: Propeller off lift curve of the wing alone for the ATLIT airplane (Reference 1)

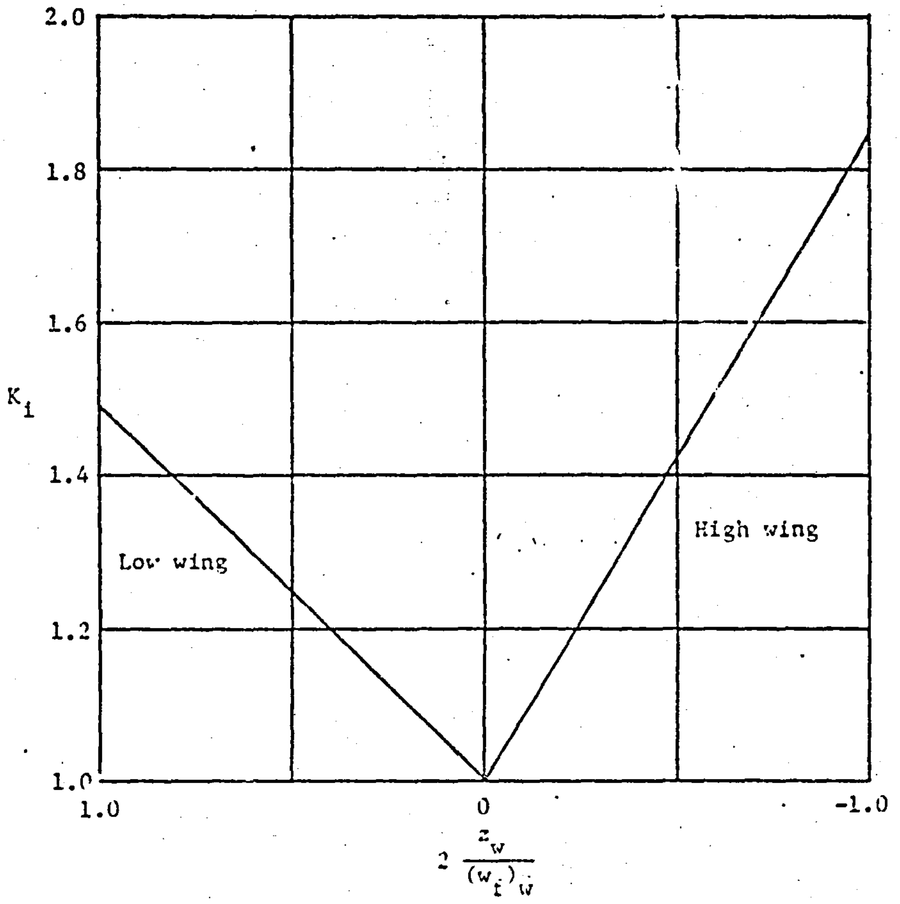

Figure 4.1.2.1: Wing body interference factor (Reference 3)

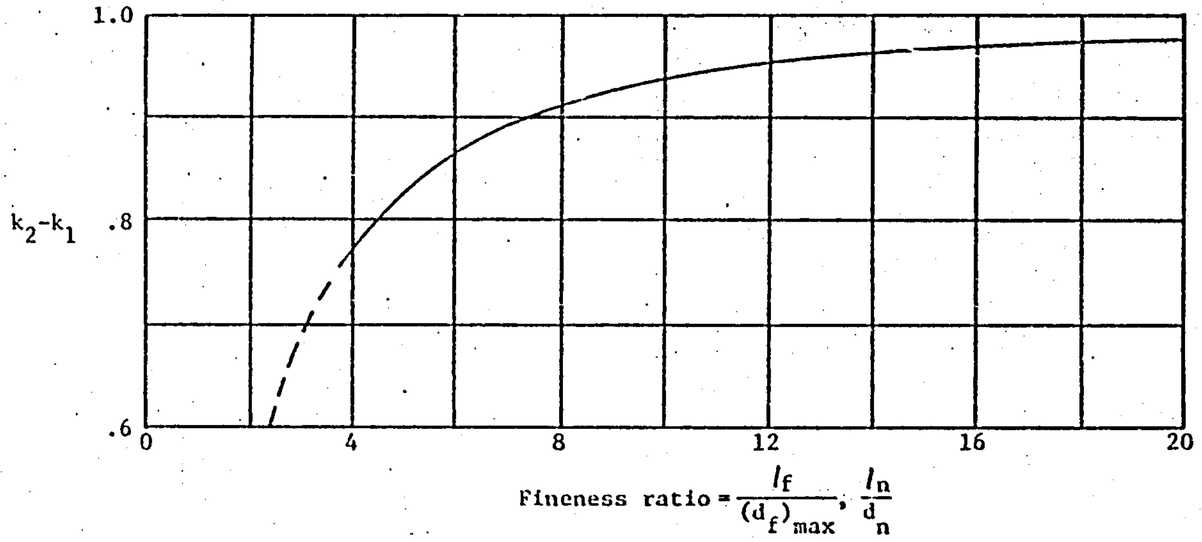

Figure 4.1.3.1: Nacelle reduced mass factor (Reference 3)

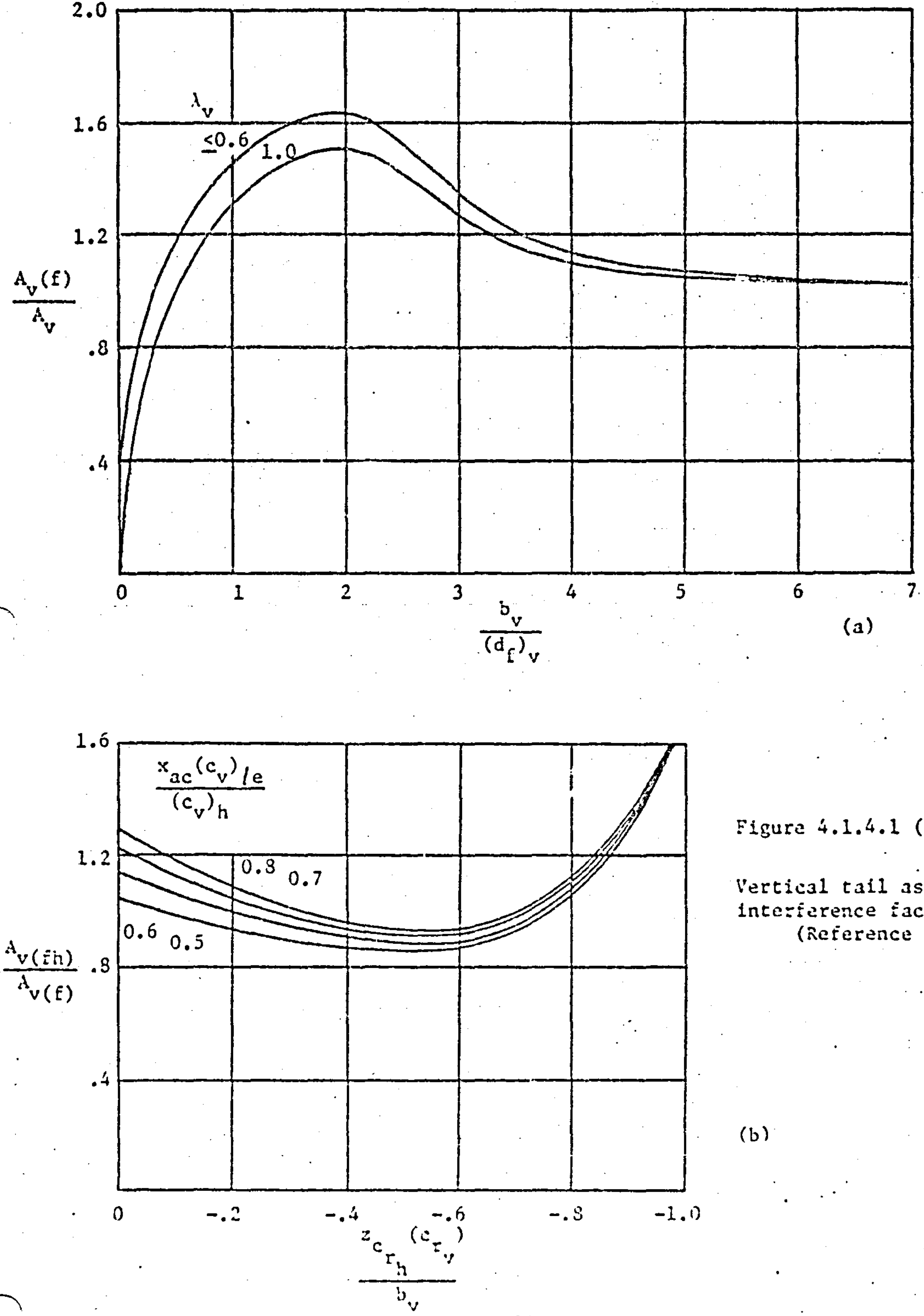

Figure 4.1.4.1 (a) & (b):

Vertical tail aspect ratio interference factors (Reference 3)

(b)

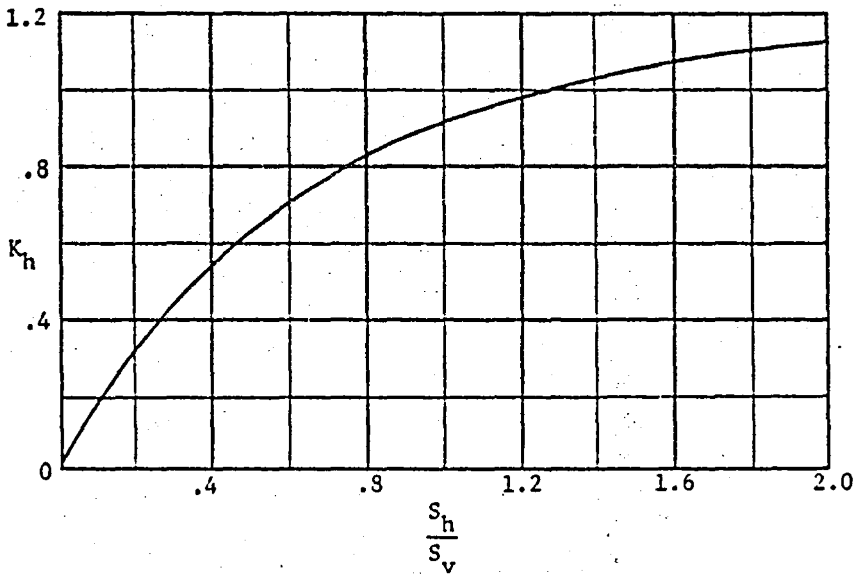

Figure 4.1.4.2: Relative tail size factor (Reference 3)

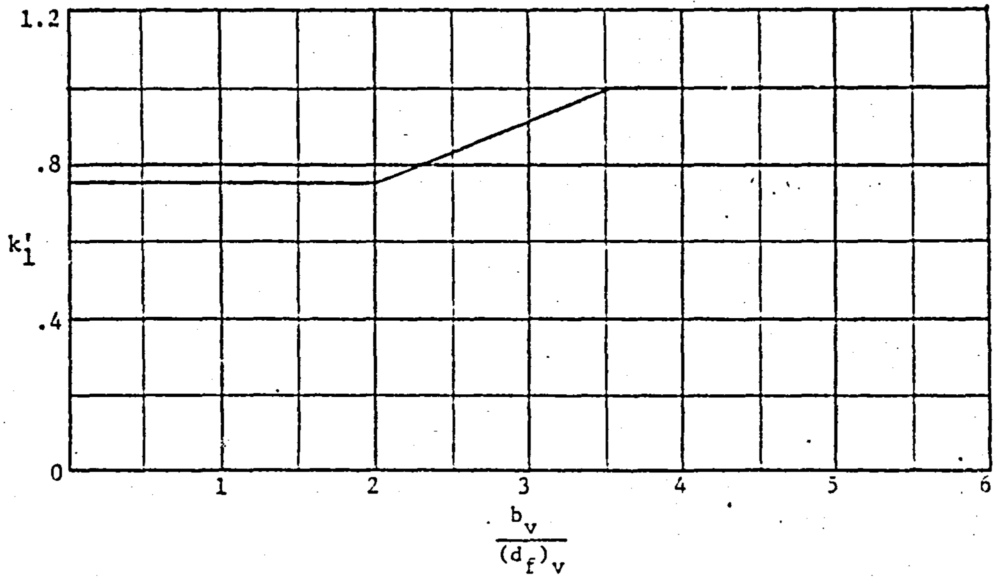

Figure 4.1.4.3: Relative body size factor (Reference 3)

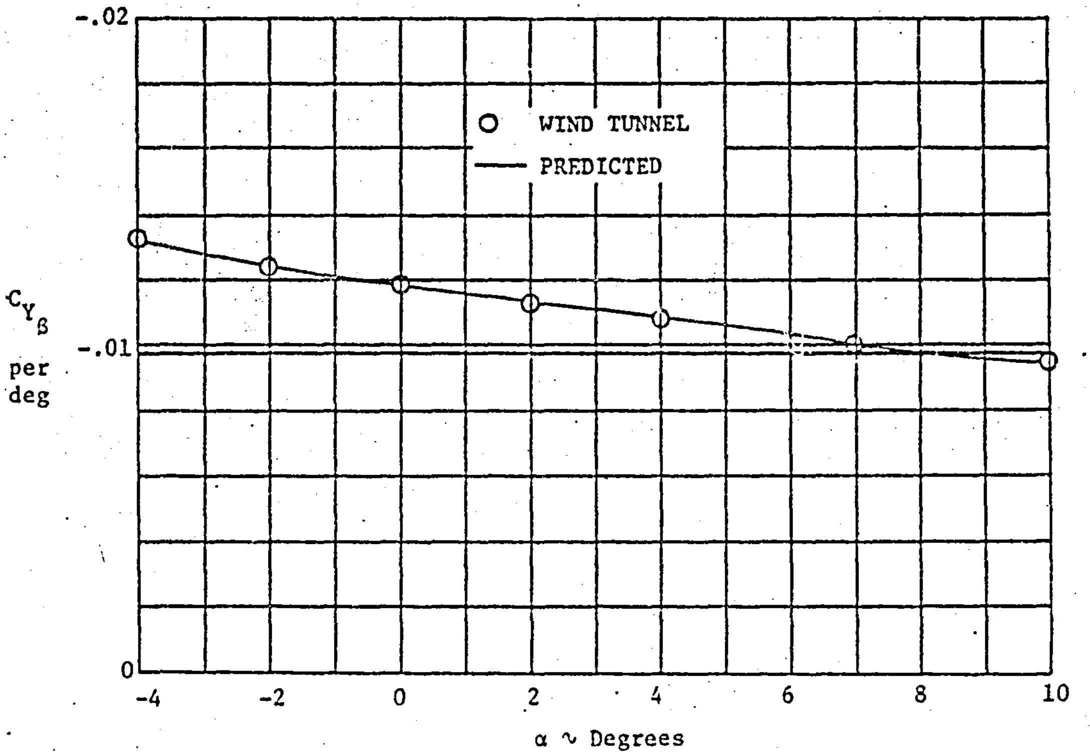

Figure 4.1.5.1: Comparison of predicted C_{Y_β} with full scale wind tunnel data (propellers removed, N_{Re} = 2.3 million).

4.2 Yawing Moment Derivative, C_{n_β}

The yawing moment due to sideslip derivative, C_{n_β}, of the complete airplane is found by considering the contributions of the following components:

(1) Wing

(2) Fuselage, including wing-fuselage interference

(3) Nacelles

(4) Vertical tail, including the interference and sidewash of the vertical tail.

4.2.1 Wing Contribution to C_{n_β}

The wing contribution to C_{n_β} is due to the increased induced drag on the leading wing caused by increased lift on the leading wing. Equation 4.2.1.1 from Reference 3 gives the incompressible $(C_{n_\beta})_w$

$$\frac{C_{n_\beta}}{C_L^2} = \frac{1}{57.3}\left[\frac{1}{4\pi A_w} - \frac{\tan \Lambda_{c/4}}{\pi A_w(A_w + 4\cos \Lambda_{c/4})}\left(\cos \Lambda_{c/4} - \frac{A_w}{2} - \frac{A_w^2}{8\cos \Lambda_{c/4}} + 6\,\frac{\bar{x}}{\bar{c}_w}\,\frac{\sin \Lambda_{c/4}}{A_w}\right)\right] \tag{4.2.1.1}$$

where

A_w is the wing aspect ratio

$\Lambda_{c/4}$ is the quarter chord sweep angle of the wing

$\bar{c}_w$ is the wing mean aerodynamic chord

$\bar{x}$ is the distance (positive rearward) from the center of gravity to the wing aerodynamic center along the mean chord line.

To correct for the three-dimensional effects of compressibility, Equation 4.2.1.2 from Reference 3 gives the wing contribution to C_{n_β}.

$$\left(\frac{C_{n_\beta}}{C_L^2}\right)_M = \left(\frac{A_w + 4 \cos \Lambda_{c/4}}{A_w B_2 + 4 \cos \Lambda_{c/4}}\right)\left(\frac{A_w^2 B_2^2 + 4 A_w B_2 \cos \Lambda_{c/4} - 8 \cos^2 \Lambda_{c/4}}{A_w^2 + 4 A_w \cos \Lambda_{c/4} - 8 \cos^2 \Lambda_{c/4}}\right)\left(\frac{C_{n_\beta}}{C_L^2}\right)_{\substack{\text{low} \\ \text{speed}}} \quad (4.2.1.2)$$

where

$B_2 = \sqrt{1 - M^2 \cos^2 \Lambda_{c/4}}$

C_{L_w} is the wing lift coefficient obtained from Figure 4.1.1.1

The summary calculations of the wing contributions to C_{n_β} are shown in Table 4.2.1.1. For the ATLIT airplane

$$(C_{n_\beta})_w = 0.000156 \; C_{L_w}^2 \text{ per deg} \quad (4.2.1.3)$$

4.2.2 Fuselage Contribution to C_{n_β}

The fuselage plus wing-body interference contribution to C_{n_β} is given in Equation 4.2.2.1, taken from Reference 3. In general, wing sweep, wing taper, and Mach number have no effect.

$$(C_{n_\beta})_{f(w)} = -K_N \frac{(S_f)_s}{S_w} \frac{l_f}{b_w} \quad (4.2.2.1)$$

where

$(S_f)_s$ is the fuselage side area obtained from Figure 2.1.4

S_w is the wing area

b_w is the wing span

l_f is the length of the fuselage from Figure 2.1.4.

There are two ways to obtain the correlation factor K_N. In Reference 4, K_N is given for midwing configurations and it is assumed that $(C_{n_\beta})_{f(w)}$ does not vary with angle of attack. A nomograph for obtaining K_N midwing configurations is shown in Figure 4.2.2.1.

In Reference 3 it was concluded on the basis of wind-tunnel data that angle of attack variations were significant for non midwing configurations. Figure 4.2.2.2 taken from Reference 3 is used to extend the nomograph to obtain K_N based on angle of attack. This graph was constructed for an airplane with $2z_w/(w_f)_w = 0.50$ and is based on tail-off wind-tunnel data. For the ATLIT airplane $2z_w/(w_f)_w = 0.33$; nevertheless, Figure 4.2.2.2 was used to obtain K_N in the absence of tail-off wind-tunnel data. If tunnel data is available, the procedure outlined in Reference 3 could be used to derive K_N for other wing locations.

Table 4.2.2.1 shows the summary calculation for the fuselage contribution to C_{n_β}.

4.2.3 Nacelle Contribution to C_{n_β}

The nacelles contribution to C_{n_β} derives directly from the nacelle side force acting through the nacelles moment arm. Equation 4.2.3.1 from Reference 3 is used to obtain the nacelles contribution.

$$(C_{n_\beta})_n = (C_{Y_\beta})_n \left(\frac{x_n \cos\alpha + z_n \sin\alpha}{b_w}\right) \qquad (4.2.3.1)$$

where

$(C_{Y_\beta})_n$ is the nacelles contribution to side force due to side slip, from Section 4.1.3.

ℓ_n is the longitudinal distance from the nacelle center of pressure to the airplane center of gravity, obtained from Figure 2.1.4

z_n is the vertical distance from the nacelle center of pressure to the airplane center of gravity, from Figure 2.1.4

b_w is the wing span, obtained from Table 2.1.

Table 4.2.3.1 summarizes the contribution of the nacelles to C_{n_β}.

4.2.4 Vertical-Tail Contribution to C_{n_β}

The vertical tail contribution to C_{n_β} is obtained in a similar manner to the nacelle contribution. The vertical tail C_{n_β} is the vertical tail C_{Y_β} times the vertical tail moment arm and is obtained from Equation 4.2.4.1 from Reference 3.

$$(C_{n_\beta})_{v(wfh)} = -(C_{Y_\beta})_{v(wfn)} \left(\frac{l_v \cos\alpha - z_v \sin\alpha}{b_w}\right) \qquad (4.2.4.1)$$

where

$(C_{Y_\beta})_{v(wfh)}$ is the side force due to sideslip of the vertical tail, from Section 4.1.4

l_v is the distance from the center of gravity to the quarter chord of the mean aerodynamic chord of the vertical tail, parallel to the X-body axis, obtained from Figure 2.1.3.

z_v is the distance from the center of gravity to the quarter chord of the mean aerodynamic chord of the vertical tail, parallel to the Z-body axis, obtained from Figure 2.1.3.

Table 4.2.4.1 summarizes the vertical tail contribution to C_{n_β}.

4.2.5 C_{n_β} of the ATLIT Airplane

The total yawing moment derivative of the complete airplane (propellers off) is

$$(C_{n_\beta})_{\substack{\text{prop}\\\text{off}}} = (C_{n_\beta})_w + (C_{n_\beta})_{f(w)} + (C_{n_\beta})_n + (C_{n_\beta})_{v(wfh)} \quad (4.2.5.1)$$

Table 4.2.5.1 summarizes the contribution of each component and the total C_{n_β}.

Table 4.2.1.1: Wing Contribution to C_{n_β}

Symbol	Description	Reference	Magnitude
M	Mach number	-	0.281
A_w	Wing aspect ratio	Table 2.1.1	10.32
$\Lambda_{c/4}$	Wing quarter-chord sweep angle, deg	Table 2.1.1	1.315
$\bar{c}_w$	Mean aerodynamic chord of wing, m (in)	Table 2.1.1	1.225 (48.22)
$\bar{x}$	Distance from wing a.c. to airplane center of gravity; in terms of $\bar{c}_w$	Figure 2.1.1	0
B_2	$\sqrt{1 - M^2 \cos^2 \Lambda_{c/4}}$	-	.997
C_{L_w}	Wing lift coefficient	Figure 4.1.1	variable

Summary $(C_{n_\beta})_w = 0.000156\, C_{L_w}^2$ per deg.

Table 4.2.2.1: Fuselage Contribution to C_{n_β}

Symbol	Description	Reference	Magnitude
$(S_f)_s$	Fuselage side area, m^2 (ft^2)	Table 4.6.1 Reference 1	7.72 (83.1)
S_w	Wing reference area, m^2 (ft^2)	Table 2.1.1	14.40 (135.0)
l_f	Fuselage length, m (ft)	Figure 2.1.4	8.352 (27.40)
b_w	Wing span, m (ft)	Table 2.1.1	12.19 (40.0)
z_w	Vertical distance of wing root chord below the centerline of the equivalent fuselage, m (ft)	Figure 2.1.4	0.194 (0.638)
$(w_f)_w$	Width of the fuselage at the quarter chord of the exposed root chord, m (ft)	Figure 2.1.4	1.19 (3.92)
N_{RE}	Reynolds number based on fuselage length	-	1.37×10^7
x_m, h, h_1, h_2	Geometric fuselage parameters	Figure 4.2.2.1	as listed
K_N	Correction factor for fuselage contribution	Figure 4.2.2.2	variable

α, deg	K_N Fig. 4.2.2.2	$(C_{n_\beta})_f$ Eq. 4.2.2.1
-4	0.00035	-0.00013
-2	0.00039	-0.00014
0	0.00043	-0.00016
2	0.00047	-0.00017
4	0.0006	-0.00022
8	0.00138	-0.00051

Table 4.2.3.1: Nacelle Contribution to C_{n_β}

Symbol	Description	Reference	Magnitude
$(C_{Y_\beta})_n$	Nacelle contribution to C_{Y_β}	Table 4.1.5.1	-0.000476
x_n	Distance from c.g. to nacelle center of pressure, m (ft)	Figure 2.1.4	0.966 (3.17)
z_n	Distance from X-body axis to nacelle center of pressure, m (ft)	Figure 2.1.4	-0.152 (-.50)
b_w	Wing span, m (ft)	Table 2.1.1	12.19 (40.0)

Summary: $(C_{n_\beta})_n = -0.0000377 \cos\alpha + 0.0000060 \sin\alpha$

Table 4.2.4.1: Vertical Tail Contribution to C_{n_β}

Symbol	Description	Reference	Magnitude
$(C_{Y_\beta})_{v(wfn)}$	Vertical tail contribution to C_{Y_β}	Table 4.1.5.1	-0.0056
l_v	Distance along X-body axis from c.g. to quarter-chord of vertical tail mean aerodynamic chord, m (ft)	Figure 2.1.5	4.50 (14.75)
z_v	Distance perpendicular to X-body axis from c.g. to quarter-chord of vertical tail mean aerodynamic chord, m (ft)	Figure 2.1.5	1.22 (4.0)
b_w	Wing span, m (ft)	Table 2.1.1	12.19 (40.0)
Summary: $(C_{n_\beta})_{v(wfn)} = 0.0021 \cos \alpha + 0.00056 \sin \alpha$			

Table 4.2.5.1: C_{n_β} of the ATLIT Airplane

α, deg	$(C_{n_\beta})_w$ Table 4.2.1.1	$(C_{n_\beta})_f$ Table 4.2.2.1	$(C_{n_\beta})_n$ Table 4.2.3.1	$(C_{n_\beta})_{v(wfn)}$ Table 4.2.4.1	$(C_{n_\beta})_{\text{prop off}}$ Eq. 4.2.5.1
-4	0	-0.00013	-0.00004	0.00206	0.00189
-2	0	-0.00014	-0.00004	0.00208	0.00190
0	0.00001	-0.00016	-0.00004	0.00210	0.00191
2	0.00004	-0.00017	-0.00004	0.00212	0.00195
4	0.00007	-0.00022	-0.00004	0.00213	0.00194

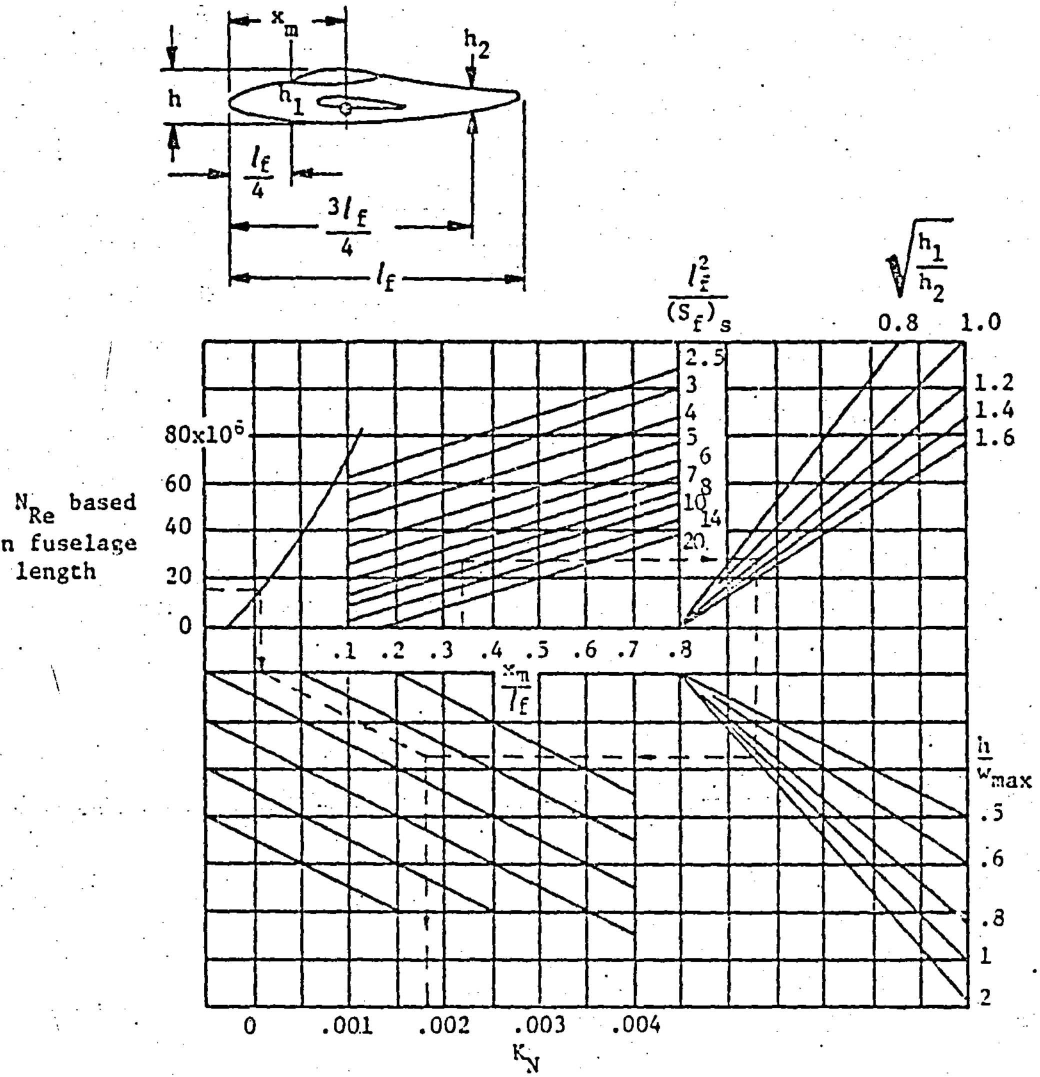

Figure 4.2.2.1: Nomograph for K_N factor for midwing configurations (Reference 3)

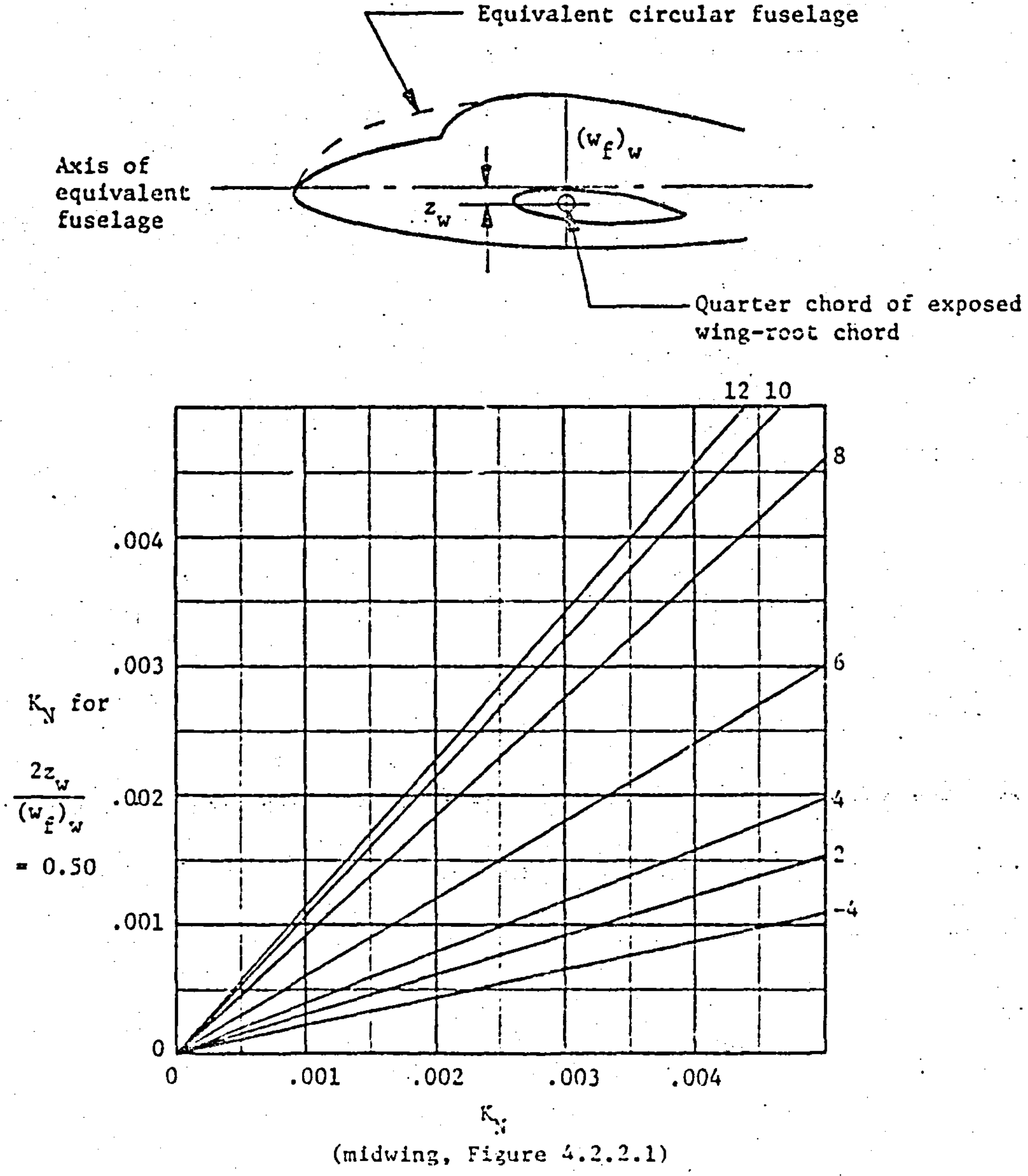

Figure 4.2.2.2: Variation of K_N with angle of attack
(Reference 3)

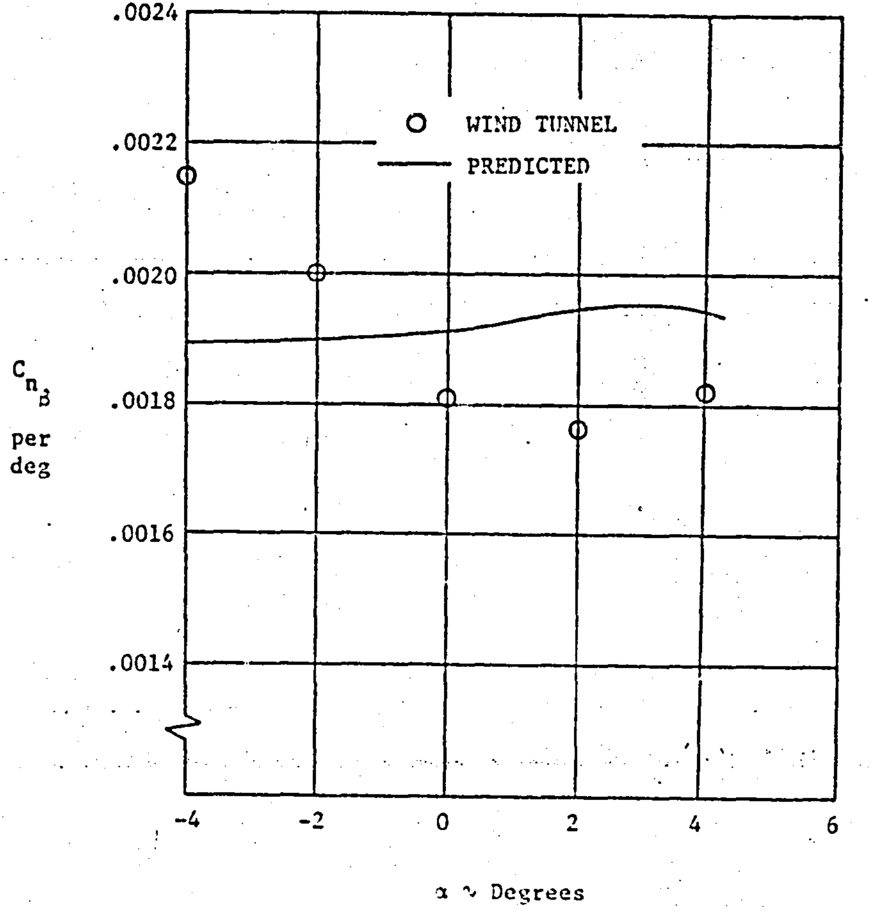

Figure 4.2.5.1: Comparison of predicted C_{n_β} with full scale wind tunnel data (propellers removed, N_{Re} = 2.3 million)

4.3 Rolling Moment Derivative, C_{ℓ_β}

The airplane rolling moment due to sideslip, C_{ℓ_β}, is composed of the following contributions:

(1) Wing (without dihedral plus the effect of dihedral)

(2) The effects of the fuselage on wing contributions

(3) The vertical tail contribution.

For general aviation airplanes without large dihedral angle on the horizontal tail, it can be assumed that there is no significant contribution by the horizontal tail.

4.3.1 Wing Contribution to C_{ℓ_β}

From Reference 3 for subsonic speed in the linear lift range, the wing contribution is given in Equation 4.3.1.1.

$$(C_{\ell_\beta})_w = (C_{\ell_\beta})_{w_{\Gamma=0}} + (C_{\ell_\beta})_\Gamma + (C_{\ell_\beta})_\theta \qquad (4.3.1.1)$$

Generally the effect of twist $(C_{\ell_{\beta_\theta}})$ is not significant.

The wing contribution to C_{ℓ_β} in the absence of geometric dihedral is given by Equation 4.3.1.2 from Reference 3.

$$(C_{\ell_\beta})_{w_{\Gamma=0}} = C_{L_w}\left[\left(\frac{C_{\ell_\beta}}{C_{L_w}}\right)_{M=0} + \left(\frac{\Delta C_{\ell_\beta}}{C_{L_w}}\right)_M\right] \qquad (4.3.1.2)$$

where

C_{L_w} is the wing lift coefficient from Figure 4.1.1.1

$\left(\frac{C_{\ell_\beta}}{C_{L_w}}\right)_{M=0}$ is the low speed portion obtained from Figure 4.3.1.1.

$\left(\frac{\Delta C_{L_\beta}}{C_{L_w}}\right)_M$ is the correction for compressible flow obtained from Equation 4.3.1.3.

$$\left(\frac{\Delta C_{\ell_\beta}}{C_{L_M}}\right)_M = -\frac{1}{2}\bar{y}^* \frac{A_w^2 M^2 \tan \Lambda_{c/4}}{\left[\left(\frac{A_w}{\cos \Lambda_{c/4}}\right)^2 - A_w^2 M^2 + 4\right]^{1/2} \left\{2 + \left[\left(\frac{A_w}{\cos \Lambda_{c/4}}\right)^2 - A_w^2 M^2 + 4\right]^{1/2}\right\}} \quad (4.3.1.3)$$

where $\bar{y}^*$ is the spanwise location of the centroid of the angle of attack load, as a function of semispan, obtained from Figure 4.3.1.2.

The effect of unifrom dihedral is accounted for by Equation 4.3.1.4 from Reference 3.

$$(C_{\ell_\beta})_\Gamma = \Gamma \left(\frac{C_{\ell_\beta}}{\Gamma}\right)_{M=0} K_{M_\Gamma} \text{ per deg} \quad (4.3.1.4)$$

where

Γ is the dihedral angle in degrees

$\left(\frac{C_{\ell_\beta}}{\Gamma}\right)_{M=0}$ is the incompressible effect of uniform dihedral obtained from Figure 4.3.1.3.

K_{M_Γ} is the compressibility correction from Figure 4.3.1.4

The summary calculations of the wing contribution to C_{ℓ_β} are shown in Table 4.3.1.1. For the ATLIT airplane

$$(C_{\ell_\beta})_w = -.000266\ C_{L_w} - .00154 \quad (4.3.1.5)$$

4.3.2 Effect of Fuselage on Wing Contribution to C_{ℓ_β}

While the fuselage itself has negligible C_{ℓ_β}, it does provide three wing-fuselage interference effects which are quite appreciable.

The first effect is caused by the vertical position of the wing. The flow about the fuselage in sideslip induces vertical flow components which cause a change in the effective wing angle of attack. Without geometric dihedral, a high wing will produce a negative C_{ℓ_β}, a low wing will produce positive C_{ℓ_β}, and a mid wing will generally show no change. Equation 4.3.2.1 from Reference 3 is used to obtain this first interference effect.

$$(C_{\ell_\beta})_{f(w)_{\Gamma=0}} = \frac{1.2\sqrt{A_w}}{57.3}\ \frac{z_w}{b_w}\ \frac{(h+w)}{b_w} \qquad (4.3.2.1)$$

where

z_w is the vertical distance from the axis of the equivalent circular fuselage to the quarter chord of the exposed wing panels, positive down, obtained from Figure 2.1.4.

h is the height of the fuselage at the wing location, from Figure 4.3.2.1

w is the width of the fuselage at the wing location, from Figure 4.3.2.1

For wings with geometric dihedral, the position of the wing with respect to the fuselage changes along the span. This is the second fuselage interference effect and is found by Equation 4.3.2 2 from Reference 3.

$$(C_{\ell_\beta})_{f(\Gamma)} = -0.0005\ \sqrt{A_w}\left[\frac{(d_f)_w}{b_w}\right]^2 \Gamma \text{ per deg} \qquad (4.3.2.2)$$

where

$(d_f)_w$ is the diameter of the equivalent circular fuselage at the wing, obtained from Figure 2.1.4.

Γ is the geometric dihedral, in degrees, obtained from Figure 3.2.1.

The third fuselage interference effect is caused by the tendency of the fuselage to straighten the flow and therefore reduce the effective sideslip angle (see Sketch A). Reference 6 shows that this effect is a function of forebody length, l'_f, wing span, and wing sweep. Reference 4 indicates that the parameter $A_w/\cos\Lambda_{c/2}$ is also important. On the basis of Reference 6 this factor is considered zero for no sweep. For most general aviation airplanes this is probably a reasonable assumption until systematic studies are made on this effect.

Table 4.3.2.1 summarizes the fuselage interference contributions to C_{ℓ_β} of the ATLIT airplane.

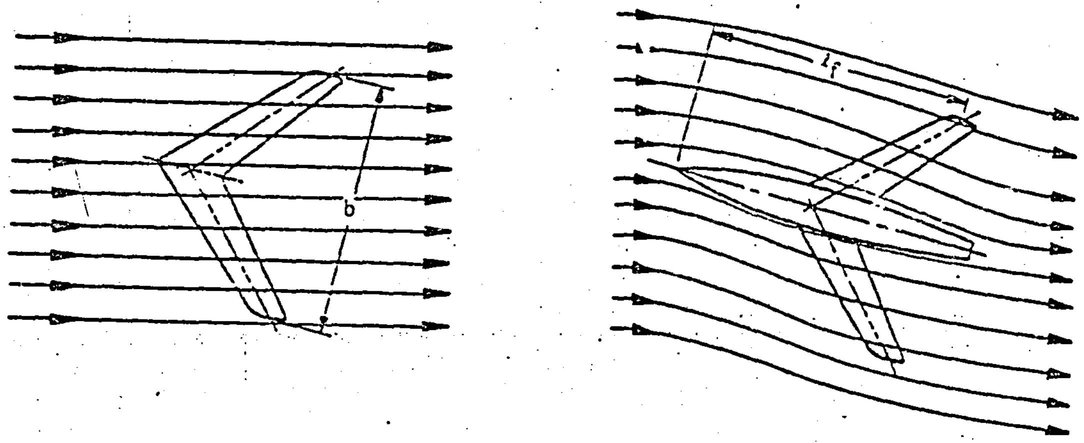

SKETCH A

4.3.3 Vertical Tail Contribution to C_{ℓ_β}

The vertical tail contributes to the airplane C_{ℓ_β} by way of the rolling moment produced by its side force due to sideslip. Equation 4.3.3.1 from Reference 3 is used to find the vertical tail contribution.

$$(C_{\ell_\beta})_{v(wfh)} = -(C_{Y_\beta})_{v(wfh)} \frac{z_v \cos\alpha + l_v \sin\alpha}{b_w} \qquad (4.3.3.1)$$

where

$(C_{Y_\beta})_{v(wfh)}$ is the vertical tail side force due to sideslip in the presence of the wing, fuselage, and horizontal tail, obtained from Table 4.1.4.1(c)

z_v is the distance from the center of gravity to the vertical tail m.a.c. perpendicular to the X-body axis, from Figure 2.1.3.

l_v is the distance from the center of gravity to the vertical tail m.a.c. parallel to the X-body axis, obtained from Figure 2.1.3.

Table 4.3.3.1 summarizes the vertical tail contribution of the ATLIT airplane.

4.3.4 C_{ℓ_β} of the ATLIT Airplane

The total rolling moment due to sideslip of the complete airplane (propellers off) is

$$(C_{\ell_\beta})_{\substack{prop\\off}} = (C_{\ell_\beta})_{w_{\Gamma=0}} + (C_{\ell_\beta})_{\Gamma} + (C_{\ell_\beta})_{f(w)_{\Gamma=0}} + (C_{\ell_\beta})_{f(\Gamma)} + (C_{\ell_\beta})_{v(wfh)} \qquad (4.3.4.1)$$

Table 4.3.4.1 summarizes the contribution of each component and shows the C_{ℓ_β} of the ATLIT airplane. In Figure 4.3.4.1 the predicted C_{ℓ_β} is compared to the wind-tunnel data. Fairly good correlation is shown up to the non-linear lift range.

Table 4.3.1.1: Wing Contribution to C_{l_β}

(a) Zero Dihedral Component

Symbol	Description	Reference	Magnitude
M	Mach number	-	0.081
C_{L_w}	Wing lift coefficient	Figure 4.1.1.1	variable
A_w	Wing aspect ratio	Table 2.1.1	10.32
λ_w	Wing taper ratio	Table 2.1.1	0.5
$\left(\frac{C_{l_\beta}}{C_{L_w}}\right)_{M=0}$	Variation of C_{l_β} with wing lift, per deg	Figure 4.3.1.1	-0.000226
$\bar{y}^*$	Spanwise position of the centroid of span loading as a fraction of semispan	Figure 4.3.1.2	0.42
Summary: $(C_{l_\beta})_{w_{\Gamma=0}} = -0.000226\ C_{L_w}$, per deg.			

(b) Dihedral Component

Symbol	Description	Reference	Magnitude
Γ	Wing dihedral angle, deg	Table 2.1.1	7
$\Lambda_{c/2}$	Wing half-chord sweep angle, deg	Table 2.1.1	0
$\left(\frac{C_{\ell_\beta}}{\Gamma}\right)_{M=0}$	Low speed effect of dihedral	Figure 4.3.1.3	-0.00022
K_{M_Γ}	Compressibility correction factor	Figure 4.3.1.4	1.0
Summary: $(C_{\ell_\beta})_\Gamma = -0.00154$, per deg.			

Table 4.3.2.1: Fuselage Effect on Wing C_{l_β}

Symbol	Description	Reference	Magnitude
A_w	Wing aspect ratio	Table 2.1.1	10.32
b_w	Wing span, m (ft)	Table 2.1.1	12.19 (40.0)
z_w	Vertical distance of wing root chord below centerline of the equivalent circular fuselage, m (ft)	Figure 2.1.4	0.194 (0.638)
$(d_f)_w = h = w$	Diameter of equivalent circular fuselage at wing, m (ft)	Figure 2.1.4	1.22 (4.0)
Γ	Wing dihedral angle, deg	Table 2.1.1	7
Summary: $(C_{l_\beta})_{f(w)_{\Gamma=0}} + (C_{l_\beta})_{f(\Gamma)} = 0.000219 - 0.000112 = 0.000107$, per deg			

Table 4.3.3.1: Vertical Tail Contribution to C_{ℓ_β}

Symbol	Description	Reference	Magnitude
$(C_{Y_\beta})_{v(wfn)}$	Vertical tail contribution to C_{Y_β}	Table 4.1.5.1	-0.0056
z_v	Distance perpendicular to X-body axis from c.g. to quarter-chord of mean aerodynamic chord of vertical tail, m (ft)	Figure 2.1.5	4.50 (14.75)
l_v	Distance along X-body axis from c.g. to quarter chord of mean aerodynamic chord of vertical tail, m (ft)	Figure 2.1.5	1.22 (4.0)
b_w	Wing span, m (ft)	Table 2.1.1	12.19 (40.0)
Summary: $(C_{\ell_\beta})_{v(wfn)} = 0.002065 \sin\alpha - 0.00056 \cos\alpha$, per deg			

Table 4.3.4.1: C_{l_β} of the ATLIT Airplane

α, deg	C_{L_w} Fig. 4.1.1.1	$(C_{l_\beta})_{w_{\Gamma=0}}$ Table 4.3.1.1 (a)	$(C_{l_\beta})_\Gamma$ Table 4.3.1.1 (b)	$(C_{l_\beta})_{f(w)}$ Table 4.3.2.1	$(C_{l_\beta})_{v(wfh)}$ Table 4.3.3.1	$(C_{l_\beta})_{prop\ off}$ Eq. 4.3.4.1
-4	-0.0533	0.000012	-0.00154	0.000107	-0.00703	-0.002124
-2	0.1243	-0.000028	-0.00154	0.000107	-0.000632	-0.002093
0	0.3019	-0.000068	-0.00154	0.000107	-0.000560	-0.002061
2	0.4795	-0.000108	-0.00154	0.000107	-0.000488	-0.002029
4	0.6571	-0.000149	-0.00154	0.000107	-0.000415	-0.001997
15.9	1.494	-0.000338	-0.00154	0.000107	0.000027	-0.001744

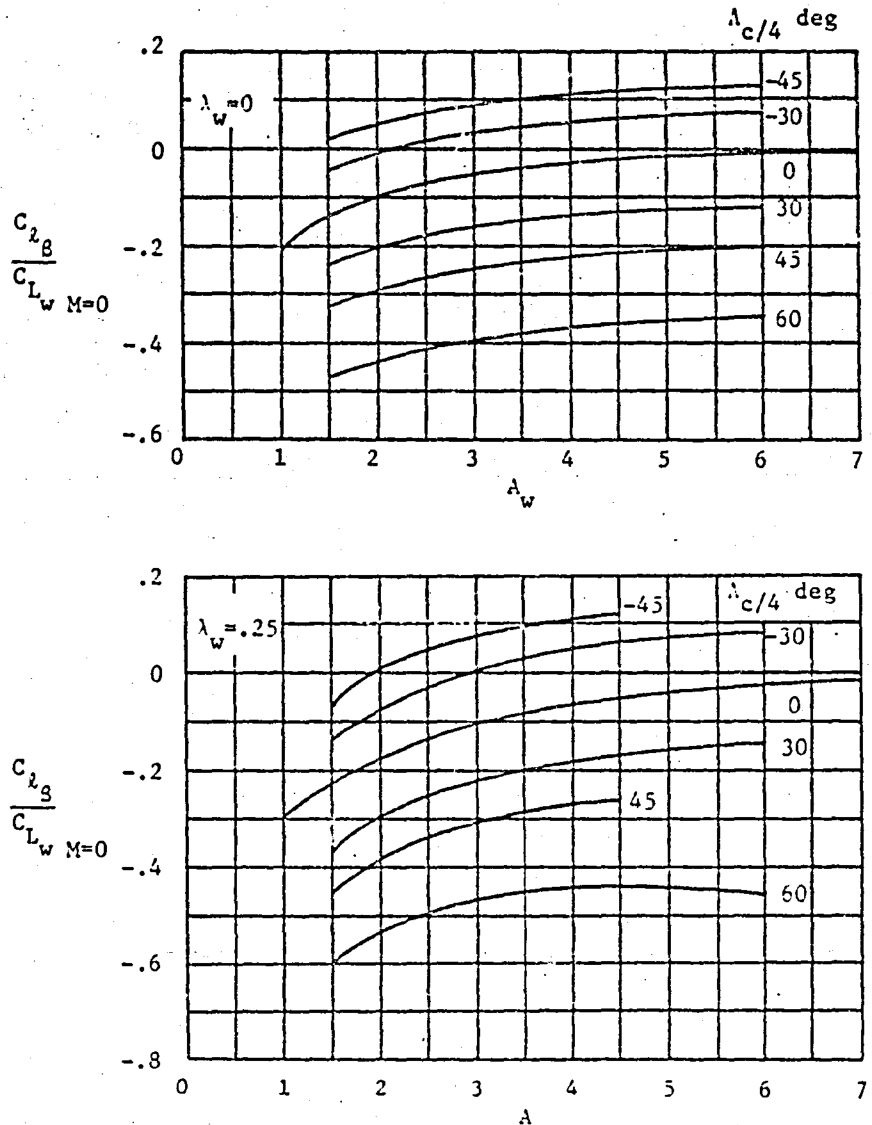

Figure 4.3.1.1: Incompressible variation of C_{ℓ_β} with wing lift (Reference 3)

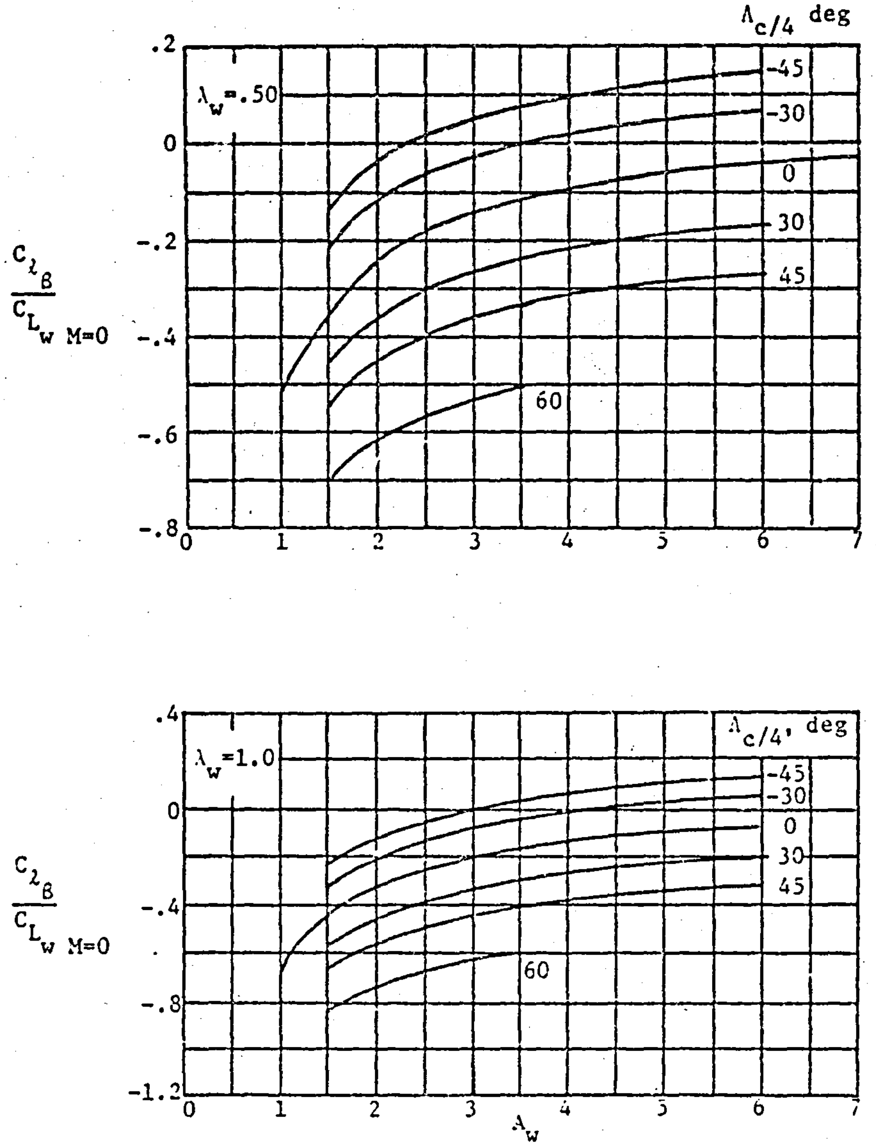

Figure 4.3.1.1: (continued)

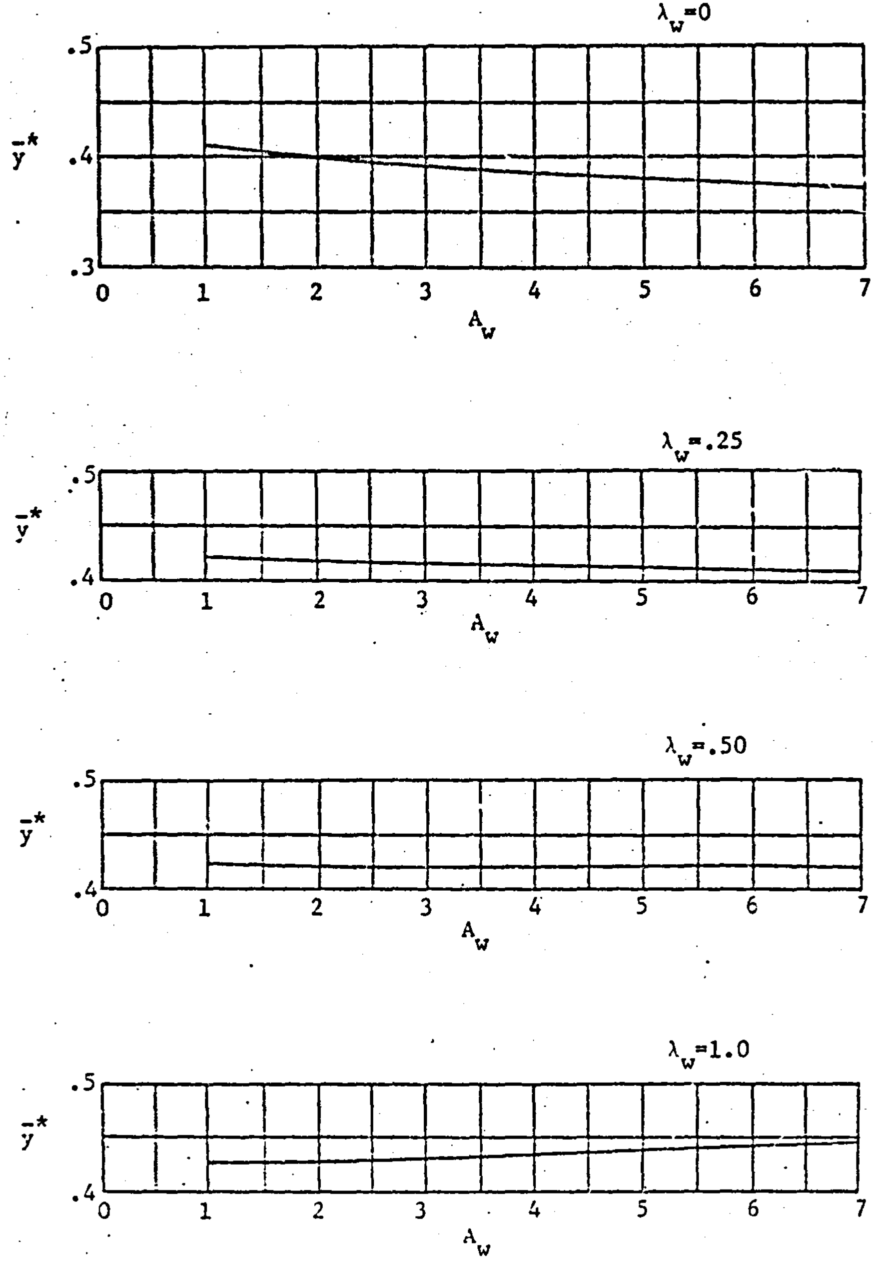

Figure 4.3.1.2: Spanwise location of centroid of angle of attack of loading for unswept wings (Reference 3)

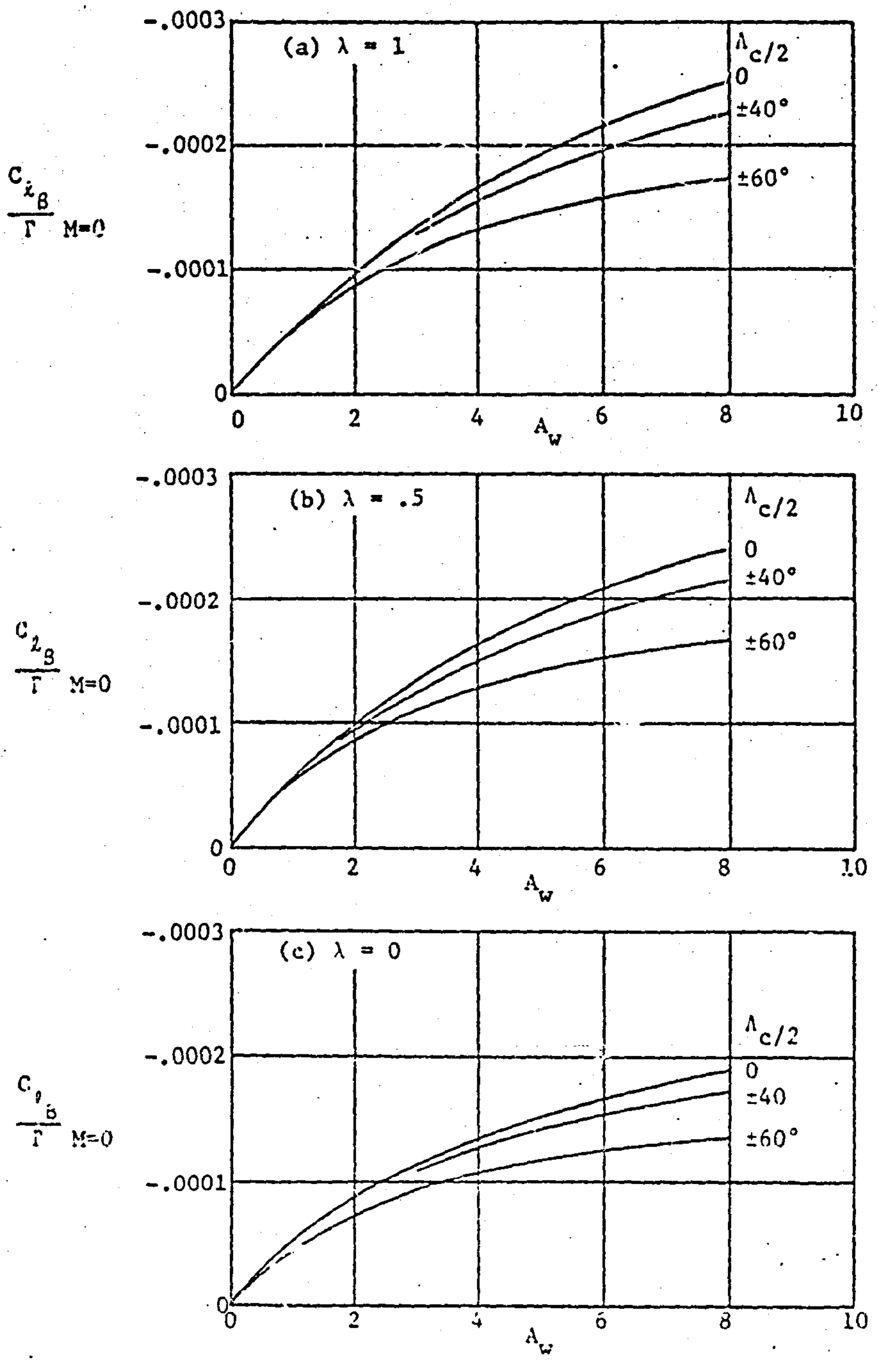

Figure 4.3.1.3: Effect of Uniform Geometric Dihedral on Wing C_{l_β} (Reference 3)

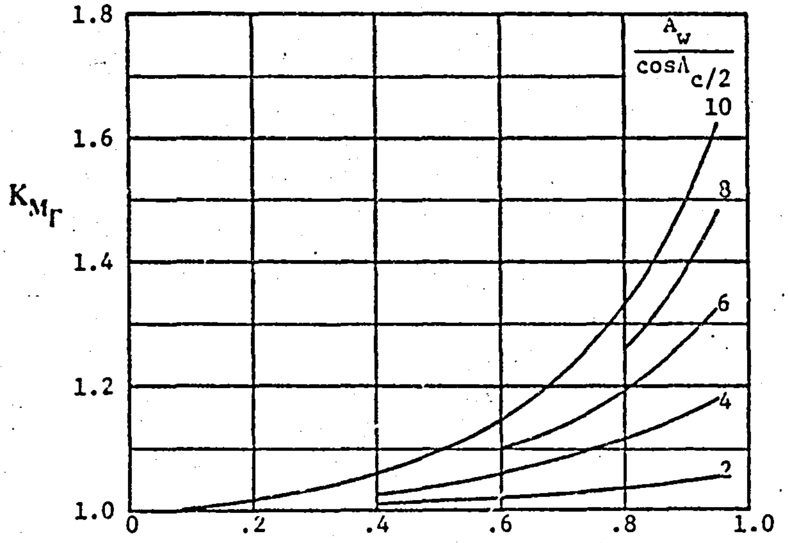

Figure 4.3.1.4: Compressibility correction for dihedral contribution to C_{ℓ_β}

(Reference 3)

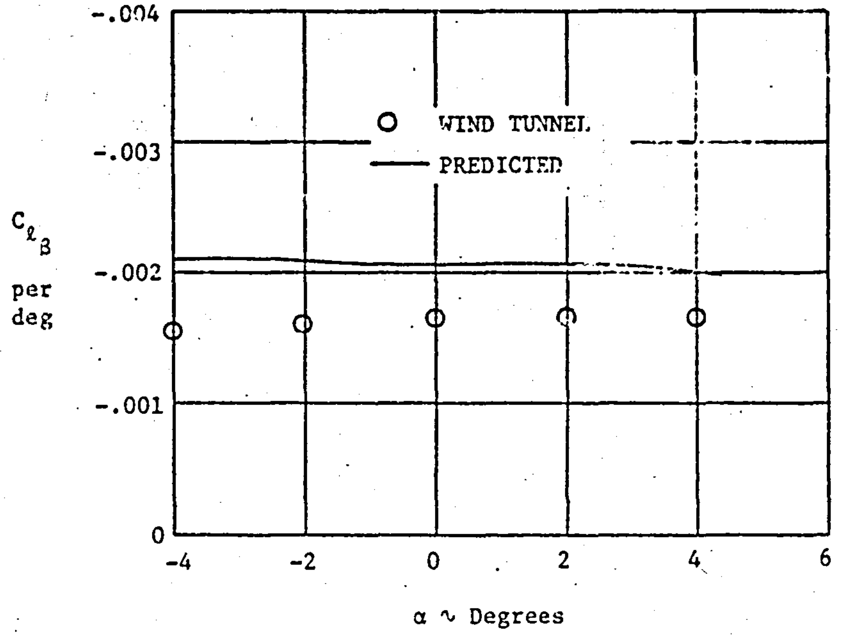

Figure 4.3.4.1: Comparison of predicted C_{ℓ_β} with full scale wind tunnel data (propellers removed, N_{Re} = 2.3 million)

4.4 Spoiler Derivatives, $C_{\ell_{\delta_s}}$, $C_{n_{\delta_s}}$

In order to free the entire trailing edge of the wing for high-lift devices, spoilers were used to provide roll control. The spoilers used are vented, gapped, upper-surface roll-control spoilers. For a discussion of the design decisions made in developing the spoiler system, see Reference 5. Figure 4.4.1 shows the spoiler installation.

4.4.1 Rolling Moment Due to Spoilers, $C_{\ell_{\delta_s}}$

The method used in obtaining the spoiler derivative $C_{\ell_{\delta_s}}$ is taken from Reference 4 and is based on a simplified lifting surface theory. This method is valid only for attached flow conditions. Reference 5 outlines some of the characteristics of spoiler in the stall region.

The rolling moment produced by deflecting one spoiler is given in Equation 4.4.1.1.

$$C_\ell = \frac{C'_{\ell_\delta}}{2}\,\Delta\alpha'_s \qquad (4.4.1.1)$$

where

$\Delta\alpha'_s$ is the spoiler lift effectiveness in terms of the change in zero-lift angle of attack, obtained from Figure 4.4.1.1

C'_{ℓ_δ} is the rolling moment effectiveness of two full chord controls deflected antisymmetrically, obtained from Figure 4.4.1.2 based on the effective inboard and outboard ends of the control. For partial span controls, this parameter is obtained as shown in Sketch A.

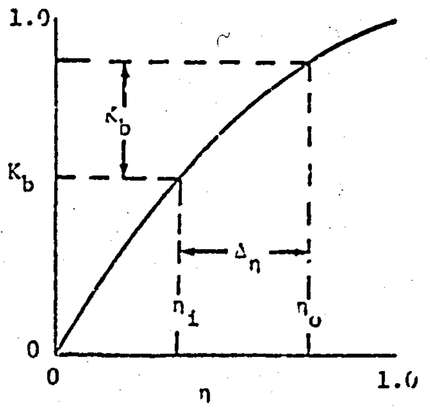

Sketch A

The effective inboard and outboard spoiler locations are given in Equation 4.4.1.2 from Reference 4.

$$\eta_{i_{eff}} = \eta_i + \Delta\,\eta_i$$
$$\eta_{o_{eff}} = \eta_o + \Delta\,\eta_o \qquad (4.4.1.2)$$

where

η_i, η_o are the actual inboard and outboard ends of the spoiler given by $\eta = \frac{y}{b/2}$

$\Delta\,\eta_i$, $\Delta\,\eta_o$ are the effective increments of the spoiler locations due to the spanwise flow of the spoiler wake, obtained from Equation 4.4.1.3.

$$\left.\begin{aligned} \Delta\eta_i &= \frac{4(1 - \frac{x'_s}{c})}{A(1 + \lambda)}\,[1 - (1 - \lambda)\eta_i]\,\frac{\cos\Lambda_{TE}\sin\theta}{\cos(\Lambda_{TE} + \theta)} \\ \Delta\eta_o &= \frac{4(1 - \frac{x'_s}{c})}{A(1 + \lambda)}\,[1 - (1 - \lambda)\eta_o]\,\frac{\cos\Lambda_{TE}\sin\theta}{\cos(\Lambda_{TE} + \theta)} \end{aligned}\right\} \qquad (4.4.1.3)$$

where

θ is determined from Figure 4.4.1.3 as a function of spoiler sweepback given in Equation 4.4.1.4.

$$\tan\Lambda_s = \tan\Lambda_{c/4} - \frac{4[0.75 - (1 - \frac{x'_s}{c})]}{A}\left(\frac{1-\lambda}{1+\lambda}\right) \qquad (4.4.1.4)$$

Using the above procedure, the spoiler rolling moment can be determined for various spoiler deflections and $C_{\ell_{\delta_s}}$ then found.

For the ATLIT spoiler deflections of 10, 20, 40, and 60 degrees were used. Table 4.4.1.1 summarizes the calculations for the ATLIT airplane. The predicted values are presented in Figure 4.4.1.4 and compared with wind tunnel data.

4.4.2 Yawing Moment Due to Spoilers, $C_{n_{\delta_s}}$

The yawing moment due to spoilers comes from two effects. The first is due to a decrease in induced drag on one wing; the second is an increase in profile drag on the wing with the deflected spoiler. The method used, taken from Reference 4, includes both effects.

For unswept wing at low angle of attack, the yawing moment is found directly from Figure 4.4.2.1. As in the case of the rolling moment, C_n should be computed for several spoiler deflection angles and $C_{n_{\delta_s}}$ then found as a function of δ_s.

Table 4.4.2.1 summarizes the ATLIT $C_{n_{\delta_s}}$ calculations. Figure 4.4.2.2 shows a comparison with wind-tunnel results.

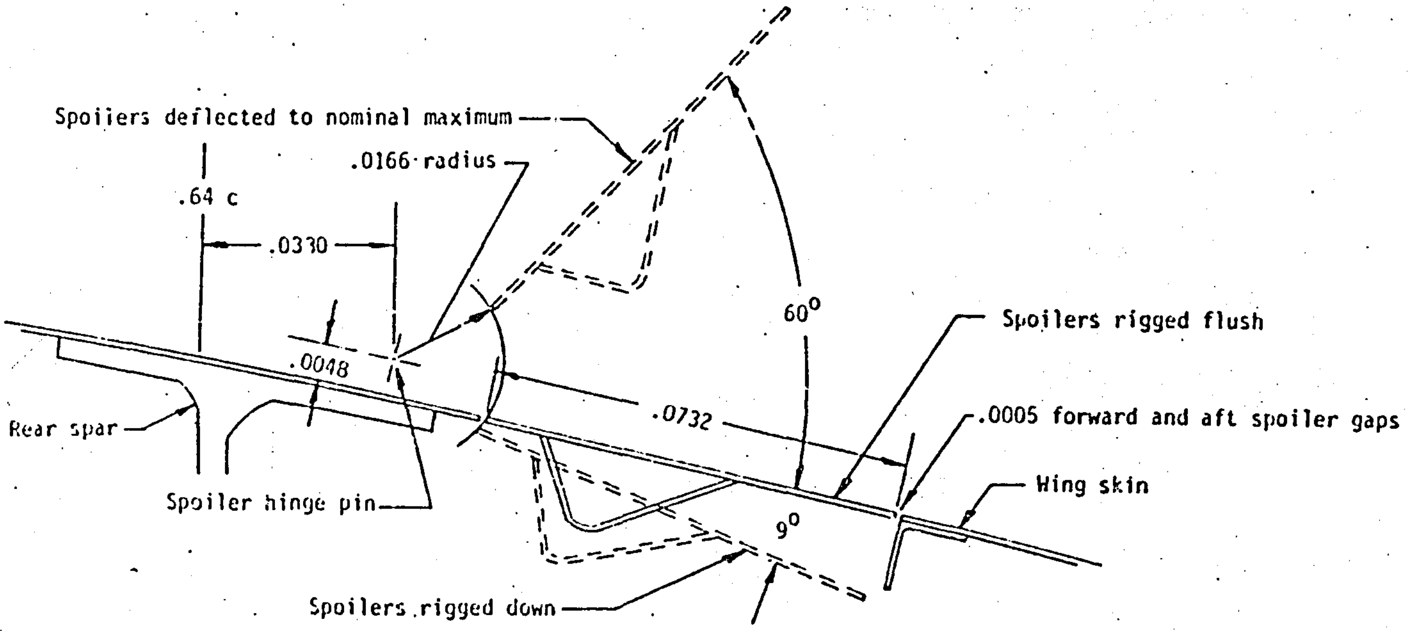

Figure 4.4.1: Spoiler Installation (Reference 7)

Table 4.4.1.1: Spoiler Effectiveness of the ATLIT Airplane

Symbol	Description	Reference	Magnitude
$\Delta\alpha'_s$	Change in zero-lift angle of attack due to spoiler deflection, radians	Figure 4.4.1.1	variable
C_{ℓ_δ}	Rolling moment effectiveness of two full chord spoilers, per rad	Figure 4.4.1.2	0.7507
η_i, η_o	Inboard and outboard nondimensional spoiler locations, $\eta = 2y/b$	Figure 2.1	0.421, 0.95
$\eta_{i_{eff}}$, $\eta_{o_{eff}}$	Effective spoiler locations	Equation 4.4.1.2	0.410, 0.943
θ	Spanwise deflection of spoiler wake, deg	Figure 4.4.1.3	-7
Λ_s	Spoiler sweep angle, deg	Equation 4.4.1.3	-1.5
δ_s	Spoiler deflection angle, deg		variable
$\frac{h_s}{c}$	Distance from airfoil mean line to end of spoiler	Figure 4.4.1	variable
$\frac{x_s}{c}$	Distance from airfoil leading edge to end of spoiler	Figure 4.4.1	variable

δ_s, deg	$\frac{x_s}{c}$	$\frac{h_s}{c}$	$\Delta\alpha'_s$	C_ℓ
10	0.771	0.054	0.056	0.021
20	0.768	0.066	0.087	0.033
40	0.755	0.090	0.108	0.041
60	0.736	0.110	0.128	0.048

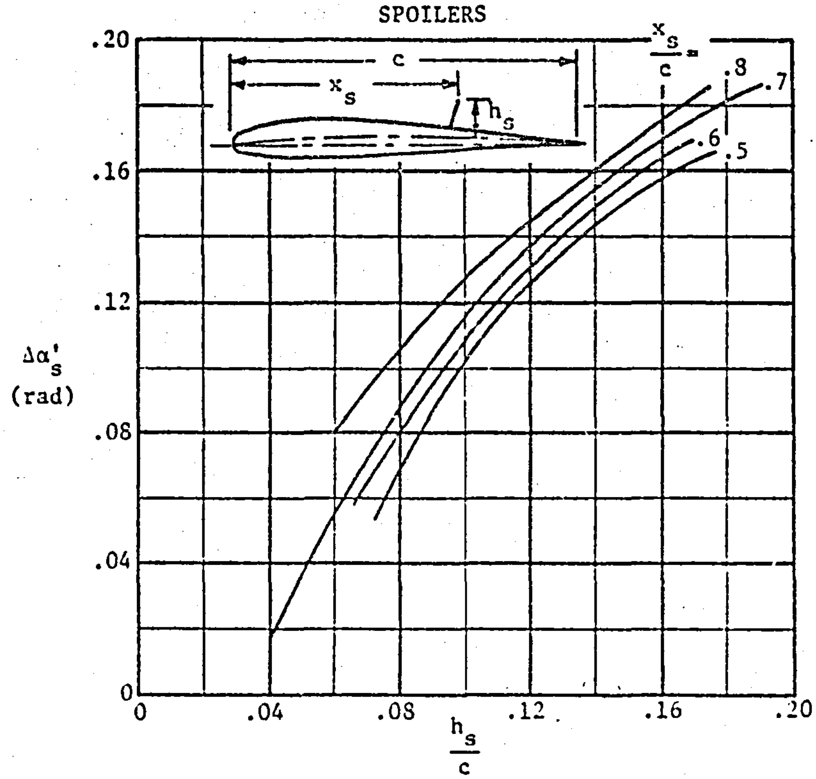

Figure 4.4.1.1: Spoiler lift effectiveness
(Reference 4)

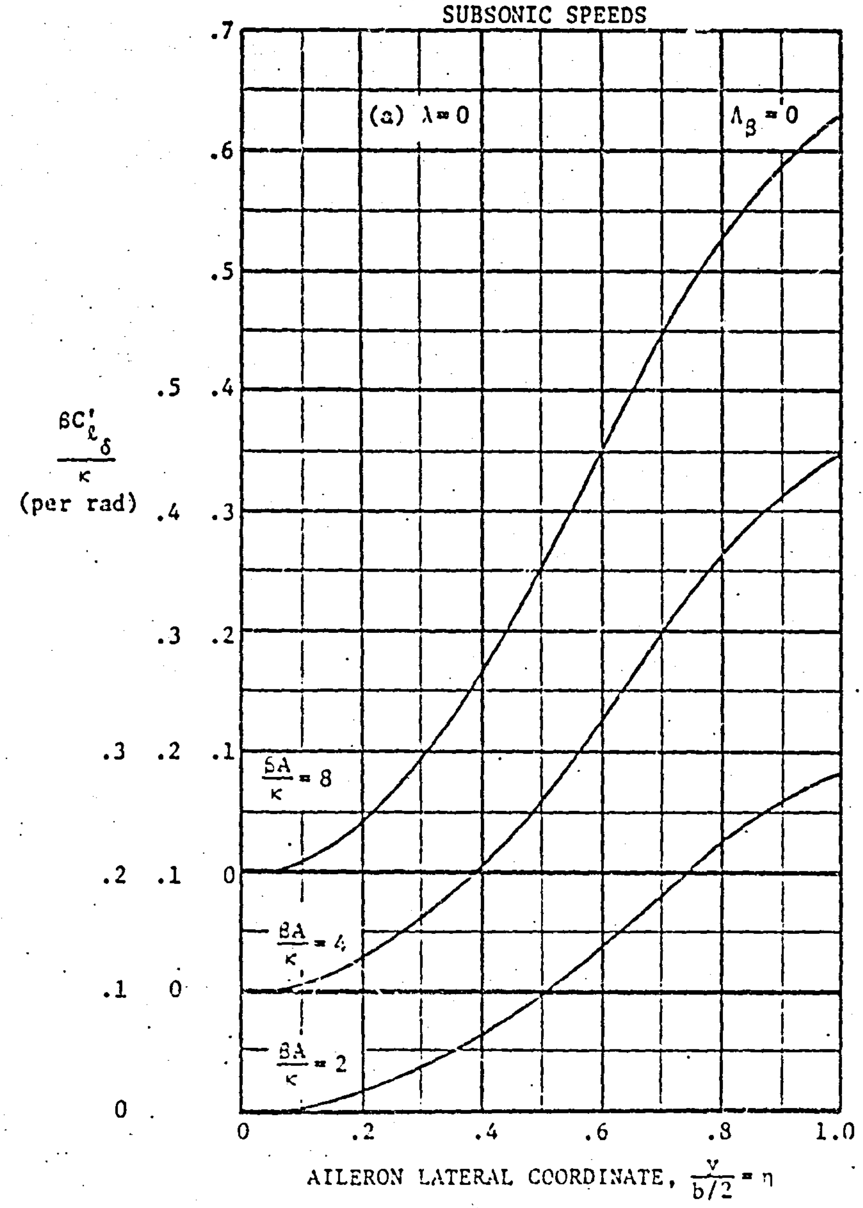

Figure 4.4.1.2(a): Rolling moment effectiveness (Reference 4)

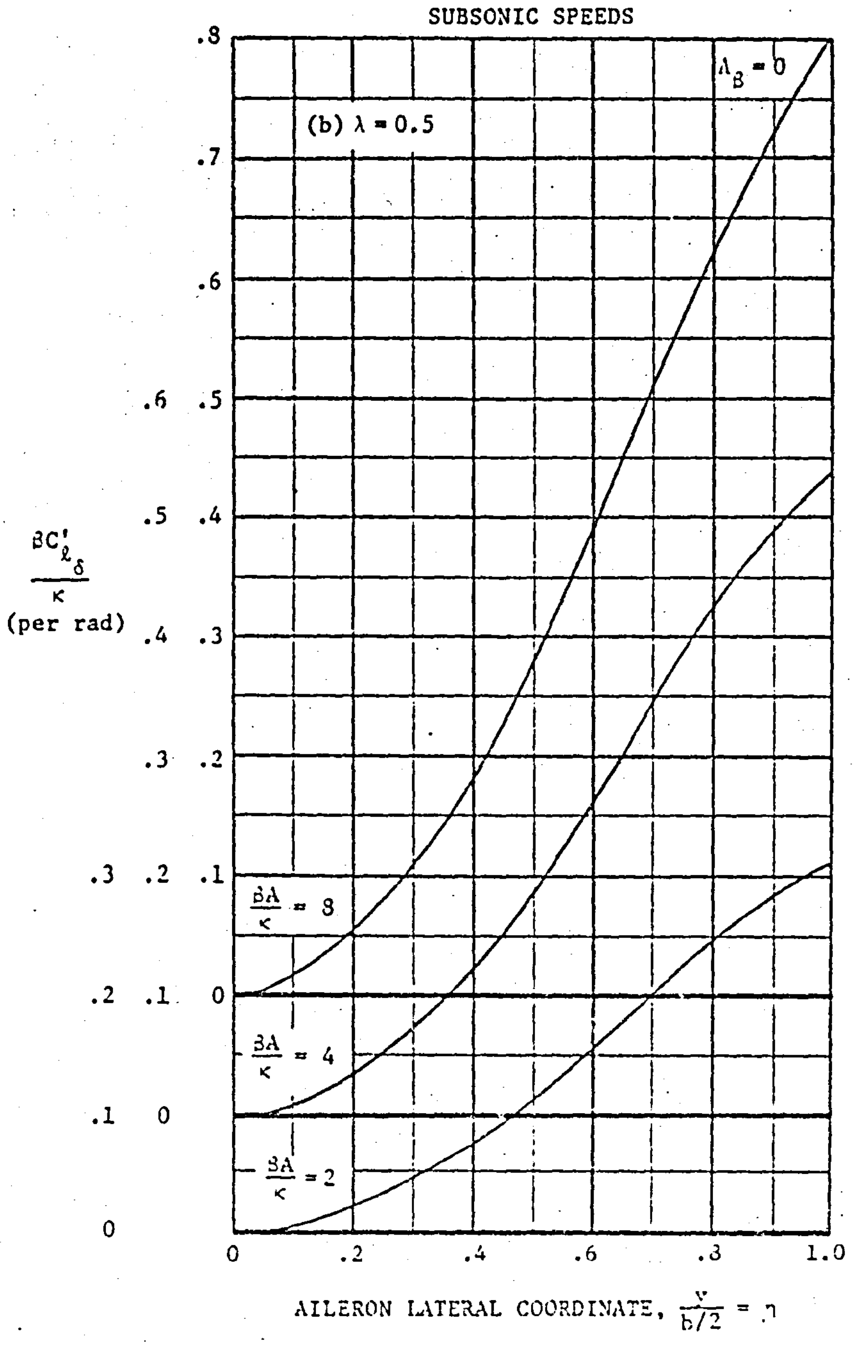

Figure 4.4.1.2(b): Rolling moment effectiveness
(Reference 4)

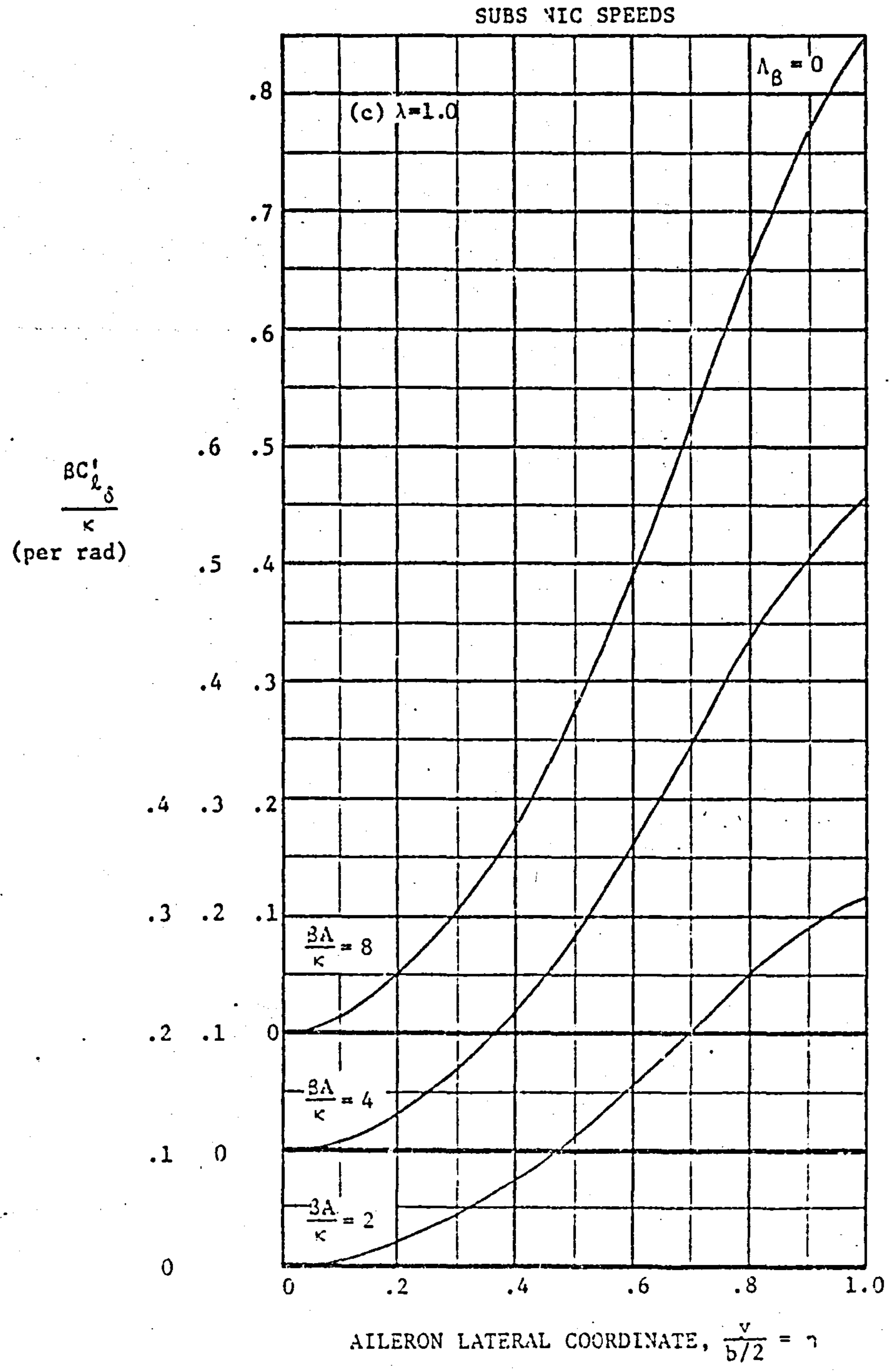

Figure 4.4.1.2(c): Rolling moment effectiveness (Reference 4)

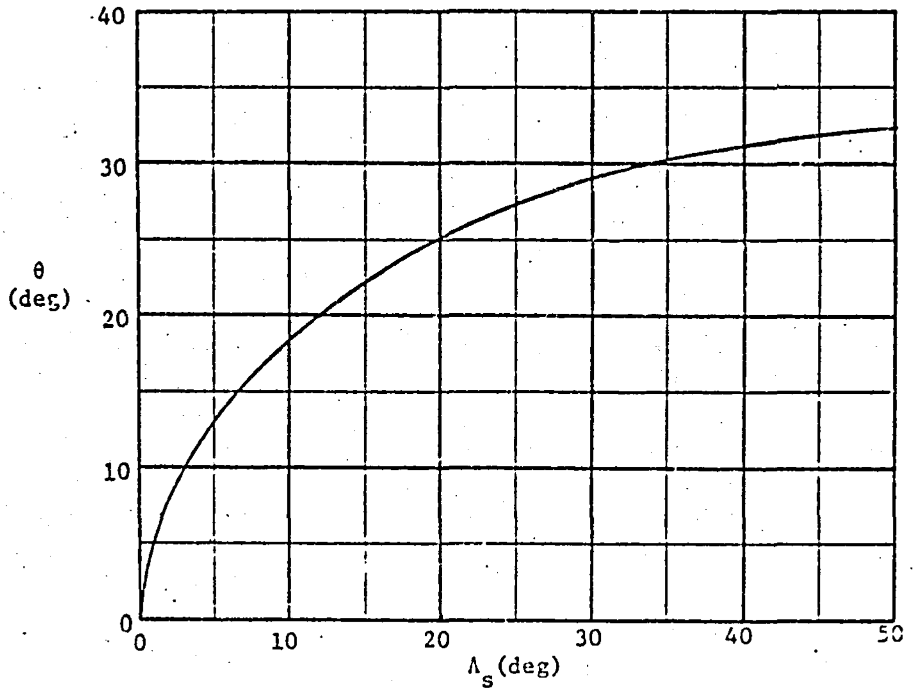

Figure 4.4.1.3: Variation of θ with spoiler sweep (Reference 4)

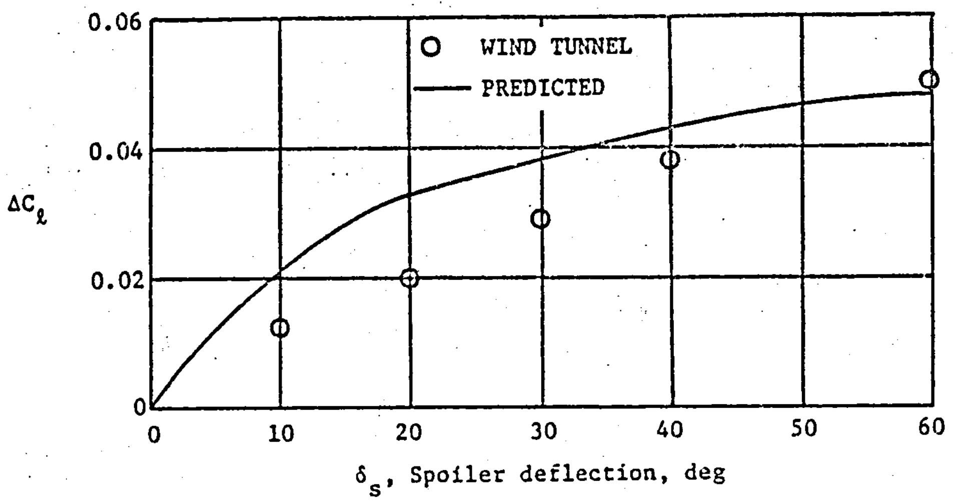

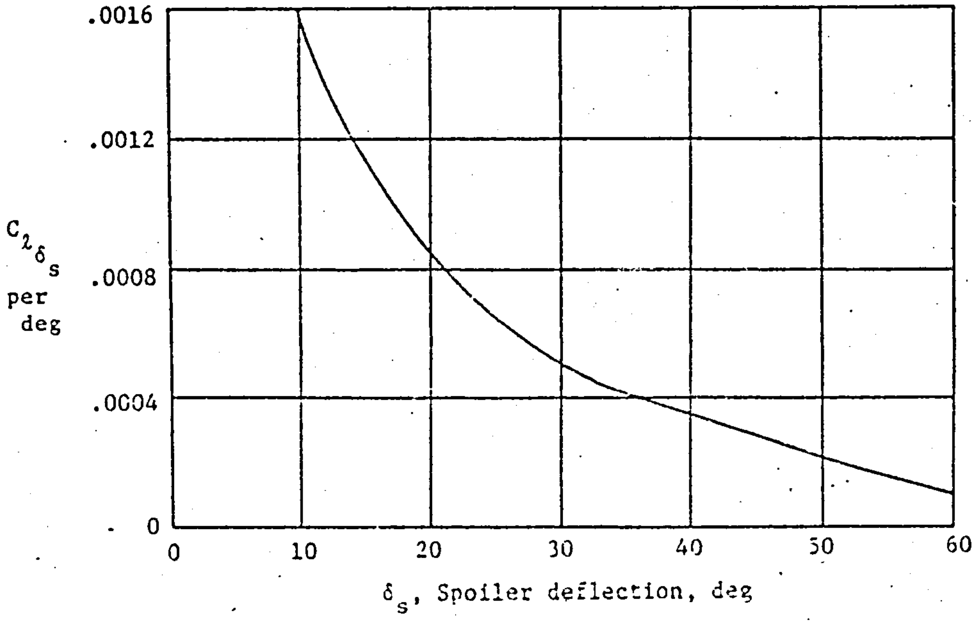

Figure 4.4.1.4 Comparison of predicted spoiler effectiveness with full-scale wind tunnel data (Power off; $\alpha = 0°$)

Table 4.4.2.1: Yawing Moment Due to Spoilers on the ATLIT Airplane

Symbol	Description	Reference	Magnitude
b_s	Spoiler span, m (ft)	Table 2.1	3.22 (10.58)
λ_w	Wing taper ratio	Table 2.1	0.5
$\frac{x_s}{c}$	Distance from airfoil leading edge to end of spoiler	Figure 4.4.1	variable
$\frac{h_s}{c}$	Distance from airfoil mean line to end of spoiler	Figure 4.4.1	variable

δ_s, deg	$\frac{x_s}{c}$	$\frac{h_s}{c}$	C_n
10	0.771	0.054	0.0013
20	0.768	0.066	0.0027
40	0.755	0.090	0.0061
60	0.736	0.110	0.0127

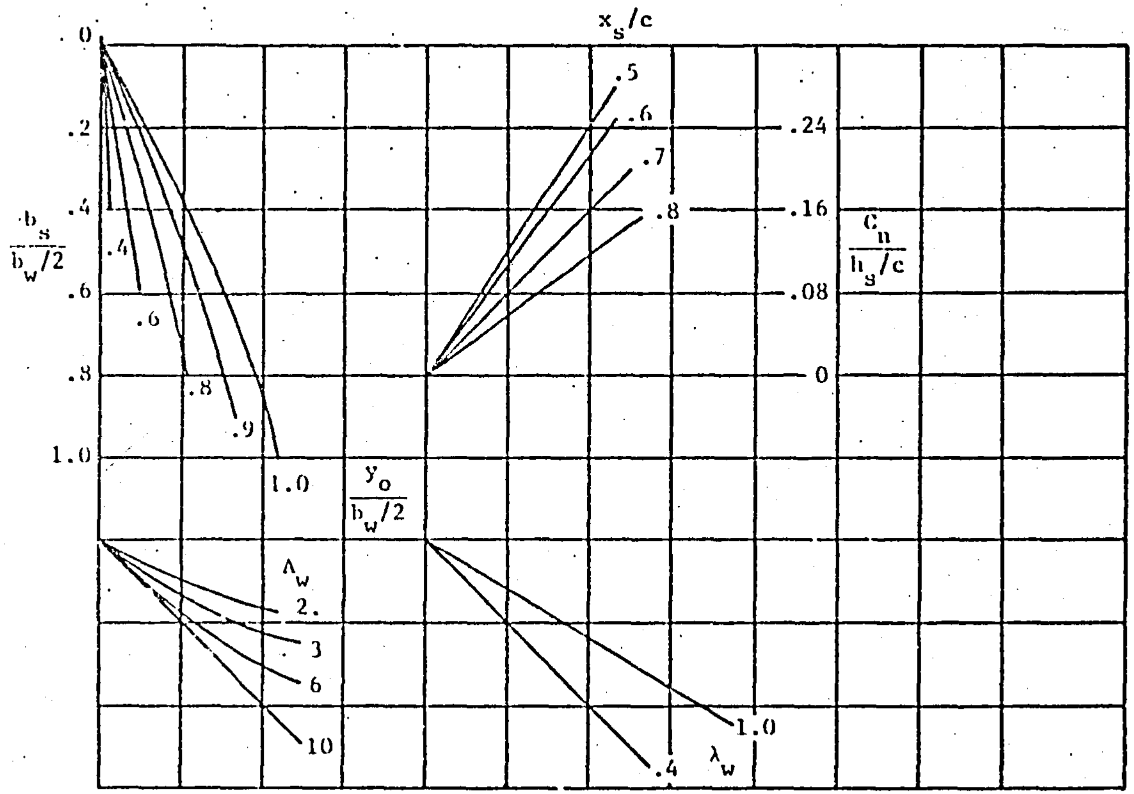

Figure 4.4.2.1: Yawing moment due to spoiler deflection (Reference 4)

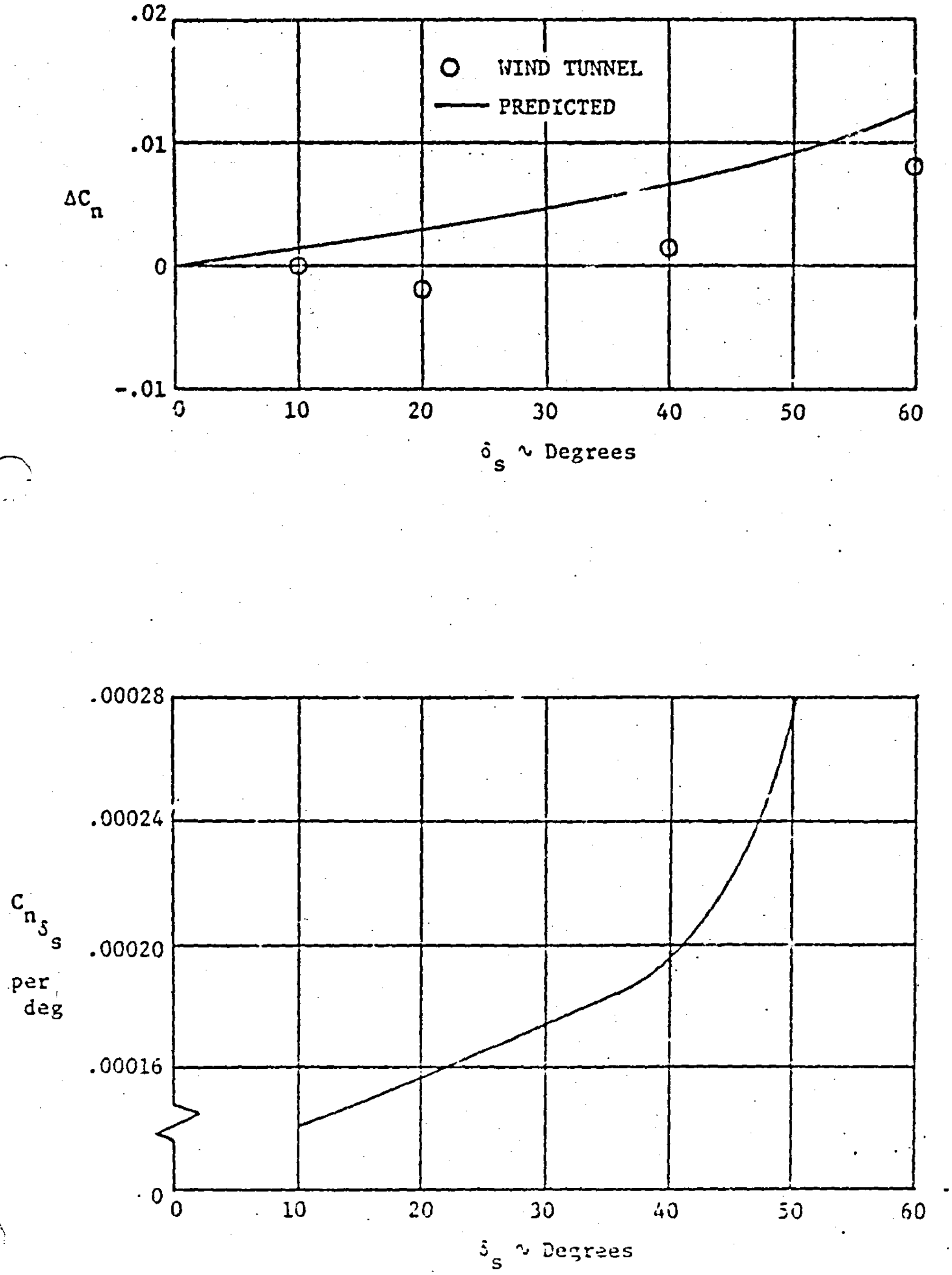

Figure 4.4.2.2 Comparison of predicted yaw due to spoilers with wind tunnel data (propellers removed, α=0°).

4.5 Rudder Control Derivatives, $C_{Y_{\delta_R}}$, $C_{n_{\delta_R}}$, $C_{\ell_{\delta_R}}$

The rudder derivatives are found by assuming that the rudder is a simple flap. The side force is determined directly and the yawing and rolling moments are found by considering the side force acting through the appropriate moment arm.

4.5.1 Side Force Due to Rudder

The side force due to rudder deflection is found by Equation 4.5.1.1 from Reference 3.

$$C_{Y_{\delta_R}} = C_{l_{\delta_R}} \frac{(C'_{L_\alpha})_v}{(C_{l_\alpha})_v} \left[\frac{(\alpha_{\delta_r})_{C_L}}{(\alpha_{\delta_r})_{C_l}}\right]_v K_b \qquad (4.5.1.1)$$

where

$(C'_{L_\alpha})_v$ is the effective lift curve slope of the vertical tail, obtained from Equation 4.5.1.2. This is the same as $-(C_{Y_\beta})_{v(wfh)}$ from Equation 4.1.4.5 with $\partial\sigma/\partial\beta = 0$.

$$(C'_{L_\alpha})_v = K'_1 (C_{L_\alpha})_{v(fh)} \frac{\bar{q}_v}{\bar{q}_\infty} \frac{S_v}{S_w} \qquad (4.5.1.2)$$

$(C_{l_\alpha})_v$ is the section lift curve slope of the vertical tail from Reference 1, Section 4.1

K_b is the rudder span factor obtained from Figure 4.5.1.1

$\left[\frac{(\alpha_{\delta_r})_{C_L}}{(\alpha_{\delta_r})_{C_l}}\right]_v$ is the rudder chord factor obtained from Figure 4.5.1.2 as a function of effective vertical tail aspect ratio and the ratio of rudder chord to vertical tail chord $\frac{c_r}{c_v}$. If $\frac{c_r}{c_v}$ is not constant, an average value should be used.

$C_{l_{\delta_r}}$ is the section lift effectiveness of the rudder obtained from Equation 4.5.1.3

$$C_{l_{\delta_r}} = \frac{1}{B_1} \cdot \frac{C_{l_\delta}}{(C_{l_\delta})_{theory}} (C_{l_\delta})_{theory} K' \qquad (4.5.1.3)$$

where

$(C_{l_\delta})_{theory}$ is the theoretical value of section lift effectiveness obtained from Figure 4.5.1.3

$\frac{C_{l_\delta}}{(C_{l_\delta})_{theory}}$ is a correction factor obtained from Figure 4.5.1.4 as a function of c_r/c_v and

$\frac{C_{l_\alpha}}{(C_{l_\alpha})_{theory}}$, where $(C_{l_\alpha})_{theory}$ is obtained from Equation 4.5.1.3 as a function of thickness ratio and trailing edge angle ϕ_{TE}

$$(C_{l_\alpha})_{theory} = 6.20 + 4.7(t/c)(1 + 0.00375\ \phi_{TE}) \text{ per radian} \qquad (4.5.1.3)$$

K' is a correction factor for reduced effectiveness at high deflection angles, obtained from Figure 4.5.1.5.

$$B_1 = \sqrt{1 - M^2}$$

The summary calculations for $C_{Y_{\delta_R}}$ of the ATLIT airplane are shown in Table 4.5.1.1. Figure 4.5.1.6 compares the calculations with full-scale wind-tunnel results for power off.

4.5.2 Rolling Moment Due to Rudder, $C_{\ell_{\delta_R}}$

The rolling moment due to rudder deflection is given by Equation 4.5.2.1 from Reference 3.

$$C_{\ell_{\delta_R}} = -C_{Y_{\delta_R}} \frac{l_v' \cos\alpha + z_v' \sin\alpha}{b_w} \qquad (4.5.2.1)$$

where

l_v' is the distance parallel to the X-body axis from the center of gravity to the quarter chord of the mean aerodynamic chord of the portion of the vertical tail spanned by the rudder.

z_v' is the distance parallel to the Z-body axis from the center of gravity to the quarter chrod of the mean aerodynamic chord of the portion of the vertical tail spanned by the rudder.

Note that for full span rudders, l_v' and z_v' are the same as l_v and z_v defined in Section 4.2.4.

Table 4.5.2.1 summarizes the ATLIT airplane's $C_{\ell_{\delta_R}}$. Figure 4.5.2.1 shows the comparison with full-scale wind-tunnel results.

4.5.3 Yawing Moment Due to Rudder, $C_{n_{\delta_R}}$

The yawing moment due to rudder deflection is given by Equation 4.5.3.1 from Reference 3.

$$C_{n_{\delta_R}} = -C_{Y_{\delta_R}} \frac{l_v' \cos\alpha - z_v' \sin\alpha}{b_w} \qquad (4.5.3.1)$$

where l_v' and z_v' are defined in Section 4.5.2.

The summary calculations for $C_{n_{\delta_R}}$ of the ATLIT airplane are shown in Table 4.5.3.1. In Figure 4.5.3.1 the predicted values are compared with wind-tunnel results.

Table 4.5.1.1: $C_{Y_{\delta_r}}$ for the ATLIT Airplane

Symbol	Description	Reference	Magnitude
S_v	Vertical tail area	Table 2.1.1	1.85 (19.9)
S_w	Wing area	Table 2.1.1	14.40 (155.0)
$C'_{L_{\alpha_v}}$	Effective lift curve slope of the vertical tail, per rad	Equation 4.5.1.2	0.2905
$(C_{l_\alpha})_v$	Section lift curve slope of the vertical tail, per rad	Table 4.2.4.1 Reference 1	6.245
K_b	Rudder span factor	Figure 4.5.1.1	1
$\left[\frac{(\alpha_{\delta_r})_{C_L}}{(\alpha_{\delta_r})_{C_L}}\right]_v$	Rudder chord factor	Figure 4.5.1.2	1.13
λ_v	Vertical tail taper ratio	Table 2.1.1	0.459
$\frac{c_r}{c_v}$	Ratio of rudder chord to vertical tail chord	Table 2.1	= 0.20
B_1	$\sqrt{1-M^2}$	-	0.997
$\frac{C_{l_\delta}'}{(C_{l_\delta})_{\text{theory}}}$	Correction factor for lift effectiveness	Figure 4.5.1.4	0.88
$(C_{l_\delta})_{\text{theory}}$	Theoretical section lift effectiveness, per rad	Equation 4.5.1.3	3.60
K'	Deflection angle correction factor	Figure 4.5.1.5	1.0
$C_{l_{\delta_r}}$	Section lift effectiveness or rudder, per rad	Equation 4.5.1.3	3.18

Summary: $C_{Y_{\delta_r}} = 0.00289$ per.deg

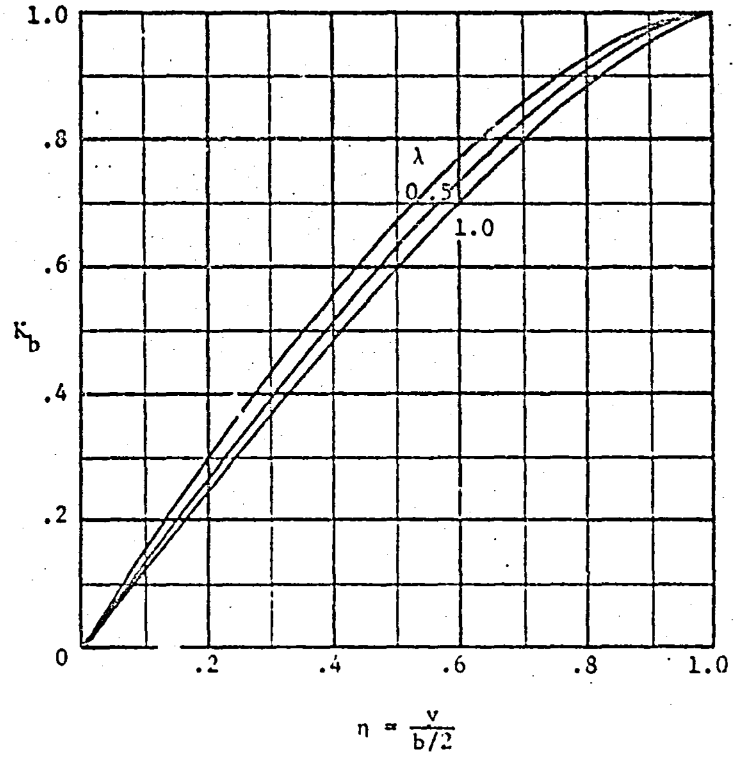

Figure 4.5.1.1: Rudder span factor (Reference 3)

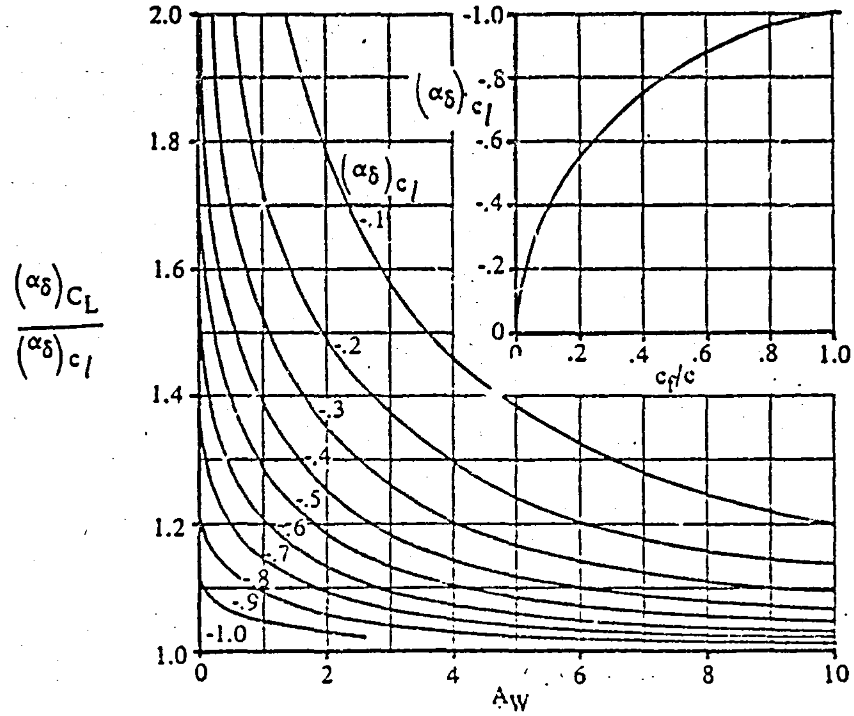

Figure 4.5.1.2: Rudder chord factor (Reference 3)

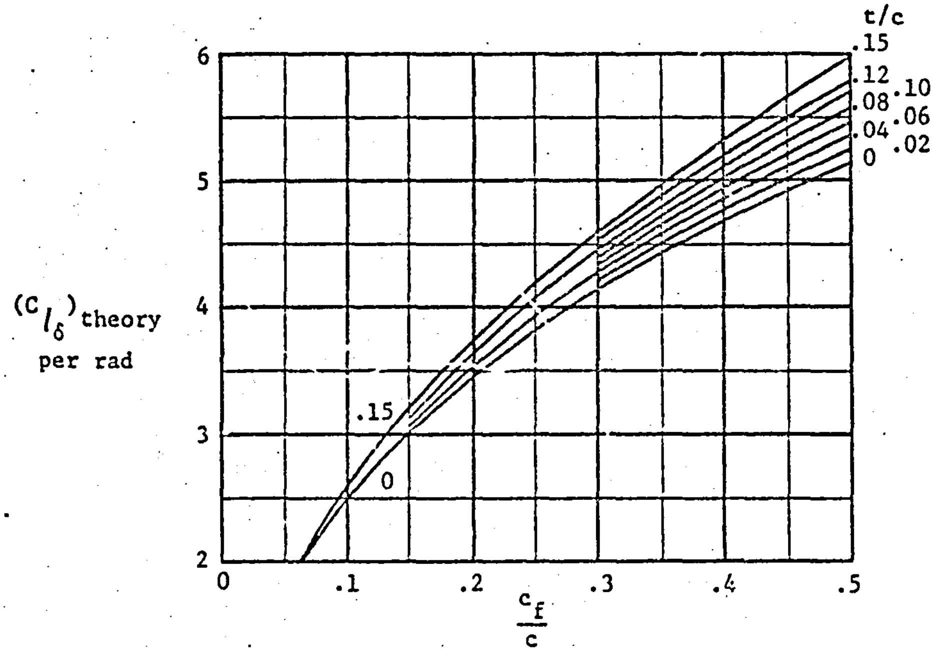

Figure 4.5.1.3: Theoretical section lift effectiveness (Reference 3)

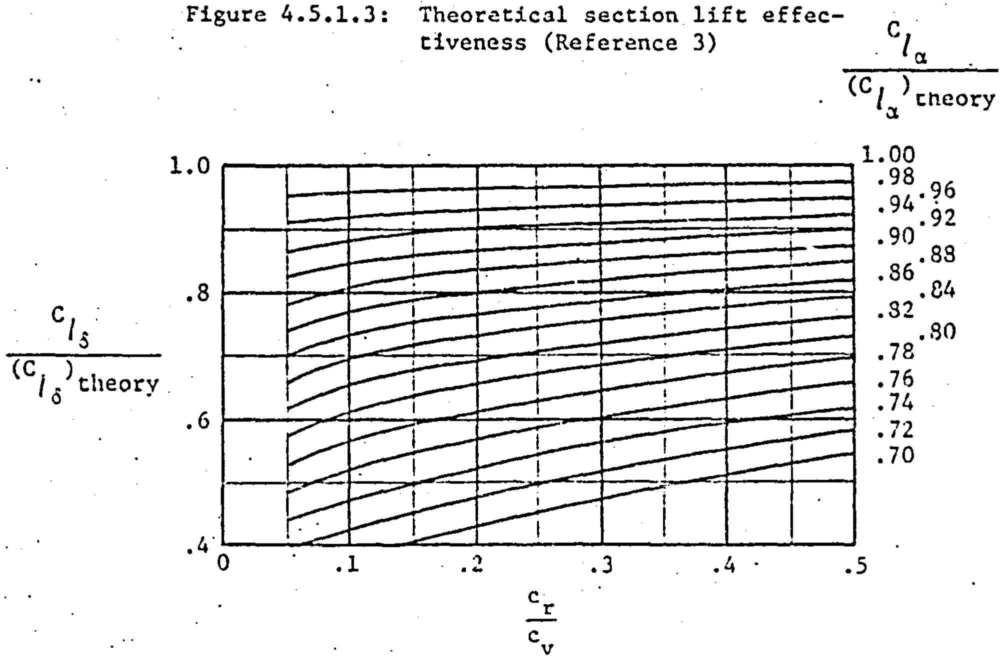

Figure 4.5.1.4: Empirical lift effectiveness correction (Reference 3)

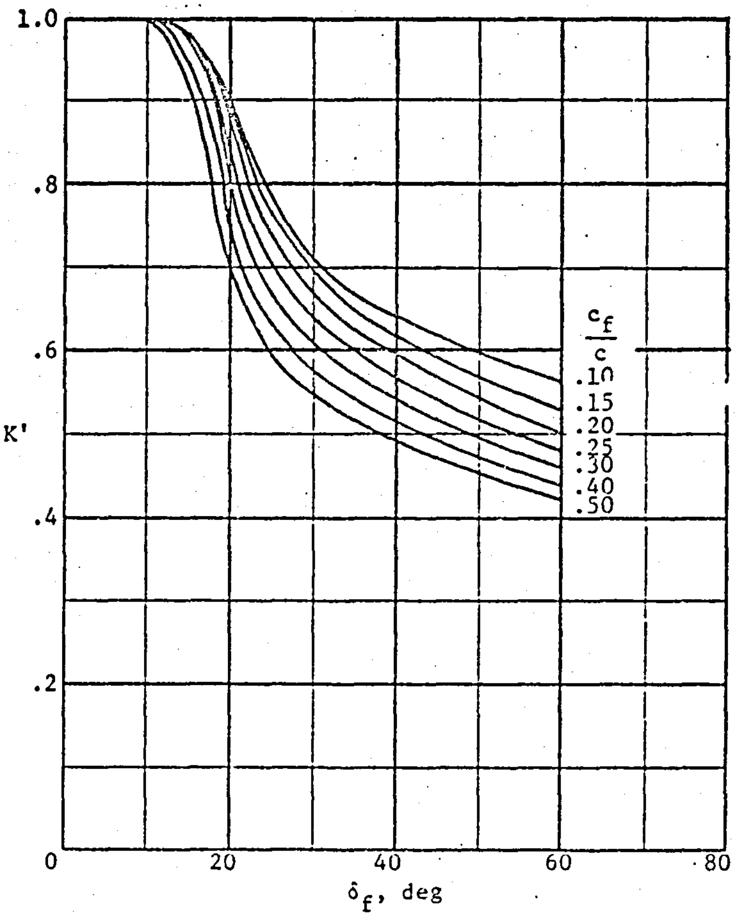

Figure 4.5.1.5: Empirical correction for high deflection angles (Reference 3)

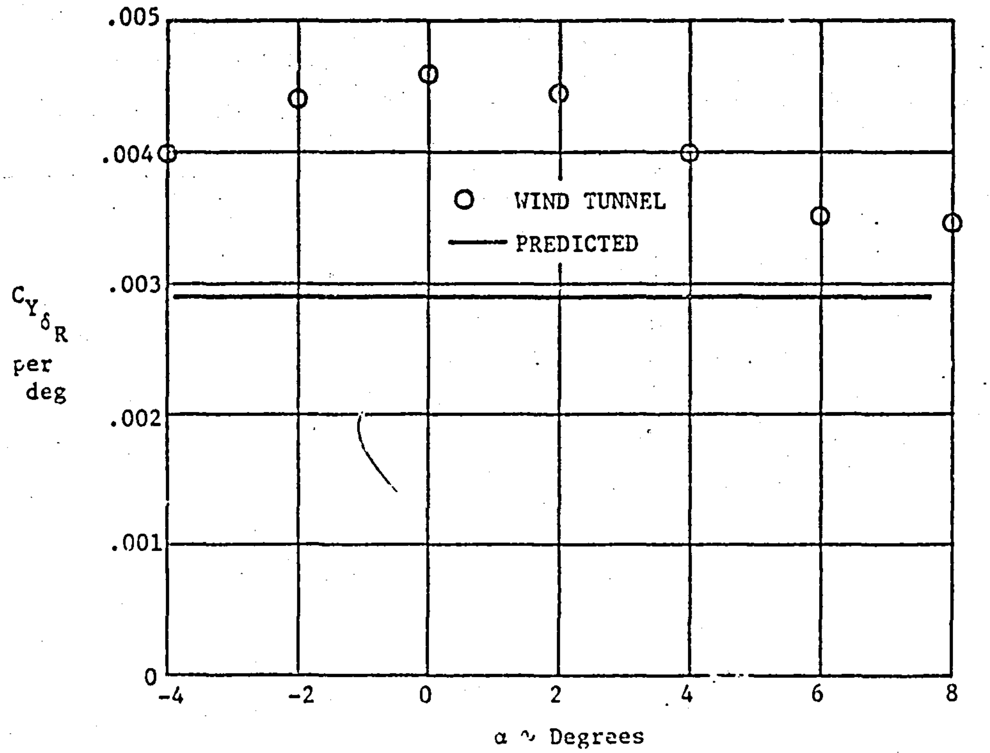

Figure 4.5.1.6: Comparison of predicted $C_{Y_{\delta_R}}$ with wind tunnel data ($\delta_R = \pm 10°$, $\beta = 0°$)

Table 4.5.2.1: $C_{\ell_{\delta_r}}$ of the ATLIT Airplane

Symbol	Description	Reference	Magnitude
$C_{Y_{\delta_r}}$	Change in side force with rudder deflection, per deg	Table 4.5.1.1	0.00289
l_v'	Distance parallel to the X-body axis from the c.g. to the quarter-chord of the mean aerodynamic chord of the portion of the vertical tail spanned by the rudder, m (ft)	Figure 2.1.5	4.50 (14.75)
z_v'	Distance parallel to the Z-body axis from the c.g. to the quarter chord of the mean aerodynamic chord of the portion of vertical tail spanned by the rudder, m (ft)	Figure 2.1.5	-1.22 (-4.0)
b_w	Wing span, m (ft)	Table 2.1.1	12.19 (40.0)

α, deg	$C_{\ell_{\delta_r}}$ per deg
-4	0.00036
-2	0.00033
0	0.00029
2	0.00025
4	0.00021
8	0.00014
15.9	-0.00001

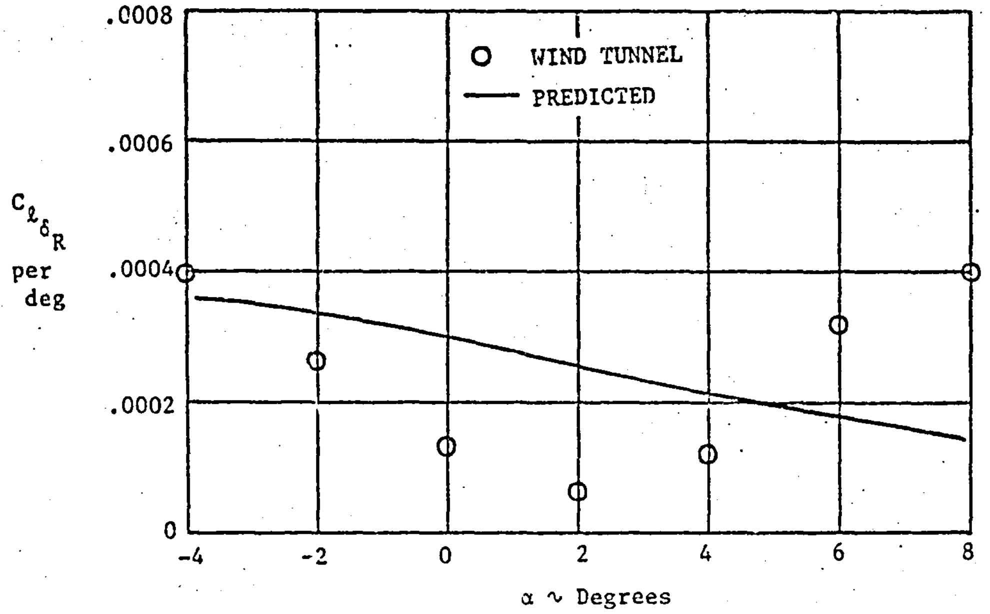

Figure 4.5.2.1: Comparison of predicted $C_{\ell_{\delta_R}}$ with wind tunnel data ($\beta = 0°$, $\delta_R = \pm 10°$)

Table 4.5.3.1: $C_{n_{\delta_r}}$ of the ATLIT Airplane

Symbol	Description	Reference	Magnitude
$C_{Y_{\delta_r}}$	Change in side force with rudder deflection, per deg	Table 4.5.1.1	0.00289
l'_v	Distance parallel to the X-body axis from the c.g. to the quarter-chord of the mean aerodynamic chord of the portion of the vertical tail spanned by the rudder, m (ft)	Figure 2.1.5	4.50 (14.75)
z'_v	Distance parallel to the Z-body axis from the c.g. to the quarter chord of the mean aerodynamic chord of the portion of vertical tail spanned by the rudder, m (ft)	Figure 2.1.5	-1.22 (-4.0)
b_w	Wing span, m (ft)	Table 2.1.1	12.19 (40.0)

α, deg	$C_{n_{\delta_r}}$ per deg
-4	-0.00104
-2	-0.00105
0	-0.00107
2	-0.00108
4	-0.00108
8	-0.00110
15.9	-0.00110

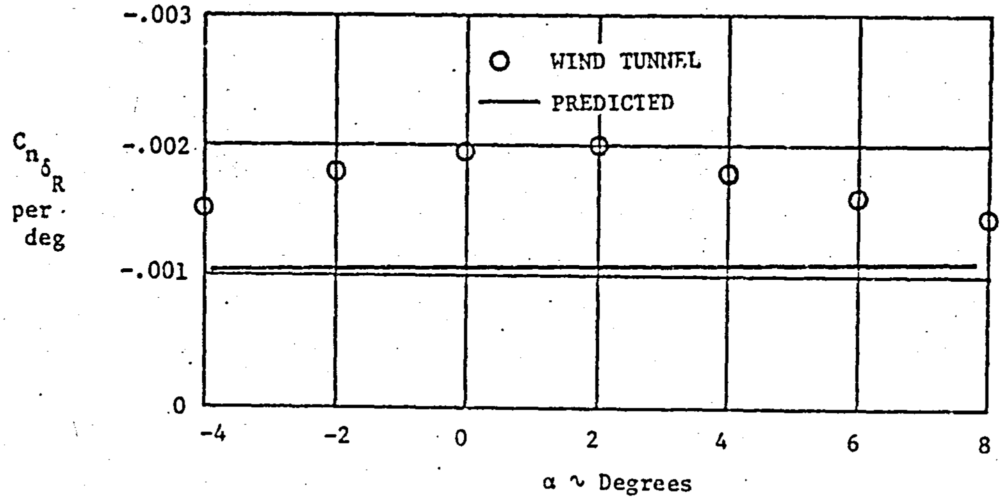

Figure 4.5.3.1: Comparison of predicted $C_{n_{\delta_R}}$ with wind tunnel data ($\beta = 0°$, $\delta_R = \pm 10°$)

CHAPTER 5

PREDICTION OF PROPELLER-OFF DYNAMIC DERIVATIVES

In this chapter the propeller-off dynamic (rate) derivatives are calculated. The methods of Reference 3 are used in all cases. The methods are based upon lifting-surface theory and are considered valid for attached flow conditions. It is assumed that the flow will remain attached up to near stall for conventional general aviation airplanes of moderate to high aspect ratio. All computed derivatives are in the stability axis system.

5.1 Roll Damping Derivative, C_{ℓ_p}

The roll damping of the airplane is found by considering the contributions of the following components:

1. Wing-body
2. Horizontal tail
3. Vertical tail
4. Nacelles

5.1.1 Wing-Body Contribution to C_{ℓ_p}

For conventional general aviation airplanes with fuselage-width to wing-span ratios of 0.25 or less, the wing is the dominating factor and the fuselage may be ignored. For zero lift, C_{ℓ_p} of the wing may be found from Figure 5.1.1.1.

To account for dihedral and non-zero lift conditions, Equation 5.1.1.1 from Reference 3 is used.

$$\left[(C_{\ell_p})_{wf}\right]_{M=0} = (C_{\ell_p})_{w_{C_L=0}} \frac{(C_{L_\alpha})_{w_{C_L}}}{(C_{L_\alpha})_{w_{C_L=0}}} \frac{(C_{\ell_p})_\Gamma}{(C_{\ell_p})_{\Gamma=0}} + (\Delta C_{\ell_p})_{drag} \qquad (5.1.1.1)$$

where

$(C_{\ell_p})_{w_{C_L=0}}$ is the zero lift C_{ℓ_p} obtained from Figure 5.1.1.1

$(C_{L_\alpha})_{w_{C_L}}$ is the propeller off lift curve slope of the wing at the lift coefficient being considered, obtained from Figure 4.1.1.1.

$(C_{L_\alpha})_{w_{C_L=0}}$ is the propeller off lift curve slope of the wing at zero lift

$\frac{(C_{\ell_p})_\Gamma}{(C_{\ell_p})_{\Gamma=0}}$ is a correction factor which accounts for wing dihedral, obtained from Figure 5.1.1.2

$(\Delta C_{\ell_p})_{drag}$ is the drag-induced rolling moment caused by wing drag in roll, obtained from Equation 5.1.1.2 from Reference 3. This increment is small for high aspect ratios.

$$(\Delta C_{\ell_p})_{drag} = -\frac{1}{8}\frac{C_{L_w}^{\ 2}}{\pi A_w \cos^2(\Lambda_{c/4})_w}\left[1 + 2\sin^2\Lambda_{c/4}\frac{A_w + 2\cos(\Lambda_{c/4})_w}{A_w + 4\cos(\Lambda_{c/4})_w}\right] - \frac{1}{8}(C_{D_o})_w \qquad (5.1.1.2)$$

where

$(C_{D_o})_w$ is the wing zero lift drag coefficient, obtained from Reference 1.

The low speed wing-body contribution to C_{ℓ_p} is next modified to account for non-zero Mach number according to Equation 5.1.1.3.

$$\left[(C_{\ell_p})_{wf}\right]_M = \frac{A_w + 4\cos(\Lambda_{c/4})_w}{A_w B_{2_w} + 4\cos(\Lambda_{c/4})_w}\left[(C_{\ell_p})_{wf}\right]_{M=0} \qquad (5.1.1.3)$$

where

$$B_{2_w} = \sqrt{1 - M^2\cos^2(\Lambda_{c/4})_w}$$

Table 5.1.1.1 summarizes the calculations for the wing-body contribution to C_{ℓ_p} for the ATLIT airplane.

5.1.2 Horizontal-Tail Contribution to C_{ℓ_p}

In general the horizontal tail contribution can be found in an analogous manner to the wing contribution. For normal tails it is of the order of one percent on the wing contribution.

For zero dihedral tails in the linear lift region, Equation 5.1.2.1 (from Reference 3) gives the horizontal tail C_{ℓ_p}, referenced to the wing area. It also accounts for wing interference effects.

$$(C_{\ell_p})_{hf} = 0.5 \frac{S_h}{S_w} \left(\frac{b_h}{b_w}\right)^2 \frac{\bar{q}_h}{\bar{q}_\infty} \left[\frac{A_h + 4\cos(\Lambda_{c/4})_h}{A_h B_{2_h} + 4\cos(\Lambda_{c/4})_h}\right] \left[(C_{\ell_p})_{h_{C_L=0}} + (\Delta C_{\ell_p})_{d_{drag}}\right] \qquad (5.1.2.1)$$

where all quantities are referenced to the horizontal tail and defined in Section 5.1.1.

In Table 5.1.2.1 the horizontal tail calculations are summarized for the ATLIT airplane.

5.1.3 Vertical Tail Contribution to C_{ℓ_p}

During rolling, the wing induces sidewash on the vertical tail due to unsymmetrical span loading. The equation used to determine the vertical tail contribution, from Reference 3, is

$$(C_{\ell_p})_v = -57.3(C'_{L_\alpha})_v \left(\frac{z_v\cos\alpha + l_v\sin\alpha}{b_w}\right)\left(\frac{2(z_v\cos\alpha + l_v\sin\alpha)}{b_w} + \frac{\partial\sigma}{\partial\frac{pb_w}{2V}}\right)$$

(5.1.3.

where

$(C'_{L_\alpha})_v$ is the vertical tail effective lift curve slope obtained from Section 4.3.1.

z_v is the vertical distance parallel to the Z-body axis from the c.g. to the vertical tail mean aerodynamic chord, obtained from Figure 2.1.3.

l_v is the horizontal distance (parallel to the X-body axis) from the center of gravity to the quarter chord of the mean aerodynamic chord of the vertical tail, from Figure 2.1.3.

$\frac{\partial\sigma}{\partial\frac{pb_w}{2V}}$ is the rate of change of sidewash with wing-tip helix angle.

There is no easy way to calculate $\frac{\partial\sigma}{\partial\frac{pb_w}{2V}}$. This factor varies with angle of attack and is influenced by aspect ratio, sweepback, and tail geometry. A value of .20 was used in Reference 3 and thus was also used here due to lack of better guidelines and the similarity of the airplane in Reference 3 with the ATLIT airplane.

The summary calculations for the vertical tail contribution are given in Table 5.1.3.1 for the ATLIT airplane. It can be seen that the effect of the tail is small.

5.1.4 Nacelle Contribution to C_{ℓ_p}

The nacelle contribution to C_{ℓ_p} is caused by the change in angle of attack induced by the roll rate. Equation 5.1.4.1 from Reference 3 gives this effect.

$$(C_{\ell_p})_n = -114.6(C_{L_\alpha})_n \left(\frac{y_T}{b_w}\right)^2 \qquad (5.1.4.1)$$

where

y_T is the distance parallel to the Y-axis from the thrust line to the center of gravity

$(C_{L_\alpha})_n$ is the lift curve slope of the nacelles

The value of $(C_{L_\alpha})_n$ was found by taking the derivative of Equation 5.1.4.2 from Reference 1 (Equation 4.3.5).

$$C_{L_n} = 0.002031\ \alpha + 0.0000201\ \alpha^2 \tag{5.1.4.2}$$

therefore

$$(C_{L_\alpha})_n = 0.002031 + 0.0000402\ \alpha \tag{5.1.4.3}$$

The nacelle contributions are summarized in Table 5.1.4.1.

5.1.5 C_{ℓ_p} of the ATLIT Airplane

The propeller-off C_{ℓ_p} of the entire airplane is given by Equation 5.1.5.1.

$$(C_{\ell_p})_{\substack{prop\\off}} = (C_{\ell_p})_{wf} + (C_{\ell_p})_{hf} + (C_{\ell_p})_v + (C_{\ell_p})_n \tag{5.1.5.1}$$

Table 5.1.5.1 summarizes the propeller-off C_{ℓ_p} of the ATLIT. Figure 5.1.5.1 presents C_{ℓ_p} as a function of angle of attack. There is no wind tunnel data available for comparison.

Table 5.1.1.1: Wing-Body Contribution to C_{ℓ_p}

Symbol	Description	Reference	Magnitude
M	Mach number	-	0.081
B_{2_w}	$\sqrt{1-M^2\cos\Lambda_{c/4}}$	-	0.997
A_w	Wing aspect ratio	Table 2.1.1	10.32
$\Lambda_{c/4}$	Wing quarter-chord sweep angle, deg.	Table 2.1.1	1.835
λ_w	Wing taper ratio	Table 2.1.1	0.5
b_w	Wing span, m (ft)	Table 2.1.1	12.19 (40.0)
d_w	Fuselage width at wing, m (ft)	Figure 2.1.4	1.22 (4.0)
$(C_{\ell_p})_{w_{C_L=0}}$	Zero lift wing-body C_{ℓ_p}, per rad	Figure 5.1.1.1	-0.525
z'_w	Vertical distance from c.g. to quarter-chord of wing root chord, m (ft)	Figure 2.1.4	0.25 (0.86)
Γ	Wing dihedral angle, deg	Table 2.1.1	7.0
$\frac{(C_{\ell_p})_\Gamma}{(C_{\ell_p})_{\Gamma=0}}$	Dihedral effect on C_{ℓ_p}	Figure 5.1.1.2	1.0
$(C_{L_\alpha})_{w_{C_L=0}}$	Wing lift curve slope at zero lift, per rad	Figure 4.1.1.1	5.09
$(C_{L_\alpha})_{w_{C_L}}$	Wing lift curve slope at C_L, per rad	Figure 4.1.1.1	5.09
$(C_{D_o})_w$	Zero lift wing drag	Table 4.12.1.2 Reference 1	0.0097

Summary: $(C_{\ell_p})_{wf} = -0.5262 - 0.003866\ C_{L_w}{}^2$ per rad

Table 5.1.2.1: Horizontal Tail Contribution to C_{ℓ_p}

Symbol	Description	Reference	Magnitude
S_h	Horizontal tail area, m^2 (ft^2)	Table 2.1.1	3.60 (38.7)
S_w	Wing area, m^2 (ft^2)	Table 2.1.1	14.40 (155.0)
A_h	Horizontal tail aspect ratio	Table 2.1.1	4.75
b_h	Horizontal tail span, m (ft)	Table 2.1.1	4.13 (13.56)
b_w	Wing span, m (ft)	Table 2.1.1	12.19 (40.0)
$\frac{\bar{q}_h}{\bar{q}_\infty}$	Dynamic pressure ratio at horizontal tail	Table 4.9.3.3 Reference 1	1.0
$\Lambda_{c/4_h}$	Horizontal tail quarter-chord sweep angle, deg	Table 2.1.1	0
$(C_{\ell_p})_{h_{C_L=0}}$	Zero lift C_{ℓ_p} of the horizontal tail	Figure 5.1.1.1	-0.38
$(\Delta C_{\ell_p})_{h_{drag}}$	Increment in C_{ℓ_p} due to drag	Equation 5.1.1.2	variable
Summary: $(C_{\ell_p})_{hf} = -0.005475 - 0.000120\, C_{L_h}^{2}$, per rad			

Table 5.1.3.1: Vertical Tail Contribution to C_{l_p}

Symbol	Description	Reference	Magnitude
$(C_{L_\alpha}')_v$	Vertical tail effective lift curve slope, per deg	Table 4.5.1.1	0.00507
z_v	Vertical distance from the c.g. to the vertical tail mean aerodynamic chord, m (ft)	Figure 2.1.5	-1.22 (-4.0)
l_v	Horizontal distance from the c.g. to the quarter-chord of the vertical tail mean aerodynamic chord, m (ft)	Figure 2.1.5	-4.50 (14.75)
b_w	Wing span, m (ft)	Table 2.1.1	12.19 (40.0)
$\frac{\partial\sigma}{\partial\frac{pb_w}{2V}}$	Rate of change of sidewash with wingtip helix angle	-	0.20

α, deg	$(C_{l_p})_v$, per rad (Eq. 5.1.3.1)
-4	-0.00186
-2	-0.00084
0	0.0
2	0.00065
4	0.00112
15.9	-0.00030

Table 5.1.4.1: Nacelle Contribution to C_{ℓ_p}

Symbol	Description	Reference	Magnitude
$(C_{L_\alpha})_n$	Nacelle lift curve slope, per deg	Equation 5.1.4.3	variable
y_T	Distance parallel to Y-axis from thrust line to c.g., m (ft)	Figure 2.1.1	1.90 (6.2)
b_w	Wing span, m (ft)	Table 2.1.1	12.19 (40.0)

α, deg	$(C_{\ell_p})_n$, per deg Eq. 5.1.4.1
-4	-0.00515
-2	-0.00537
0	-0.00559
2	-0.00581
4	-0.00603
15.9	-0.00735

Table 5.1.5.1: C_{ℓ_p} of the ATLIT Airplane

α, deg	$(C_{\ell_p})_{wf}$ Table 5.1.1.1	$(C_{\ell_p})_{hf}$ Table 5.1.2.1	$(C_{\ell_p})_{v}$ Table 5.1.3.1	$(C_{\ell_p})_{n}$ Table 5.1.4.1	$(C_{\ell_p})_{prop\ off}$ Eq. 5.1.5.1
-4	-0.5273	-0.0055	-0.00186	-0.00515	-0.5398
-2	-0.5274	-0.0055	-0.00084	-0.00537	-0.5391
0	-0.5277	-0.0055	0.0	-0.00559	-0.5388
2	-0.5282	-0.0055	0.00065	-0.00581	-0.5289
4	-0.5290	-0.0055	0.00112	-0.00603	-0.5394
15.9	-0.5359	-0.0055	-0.00030	-0.00735	-0.5491

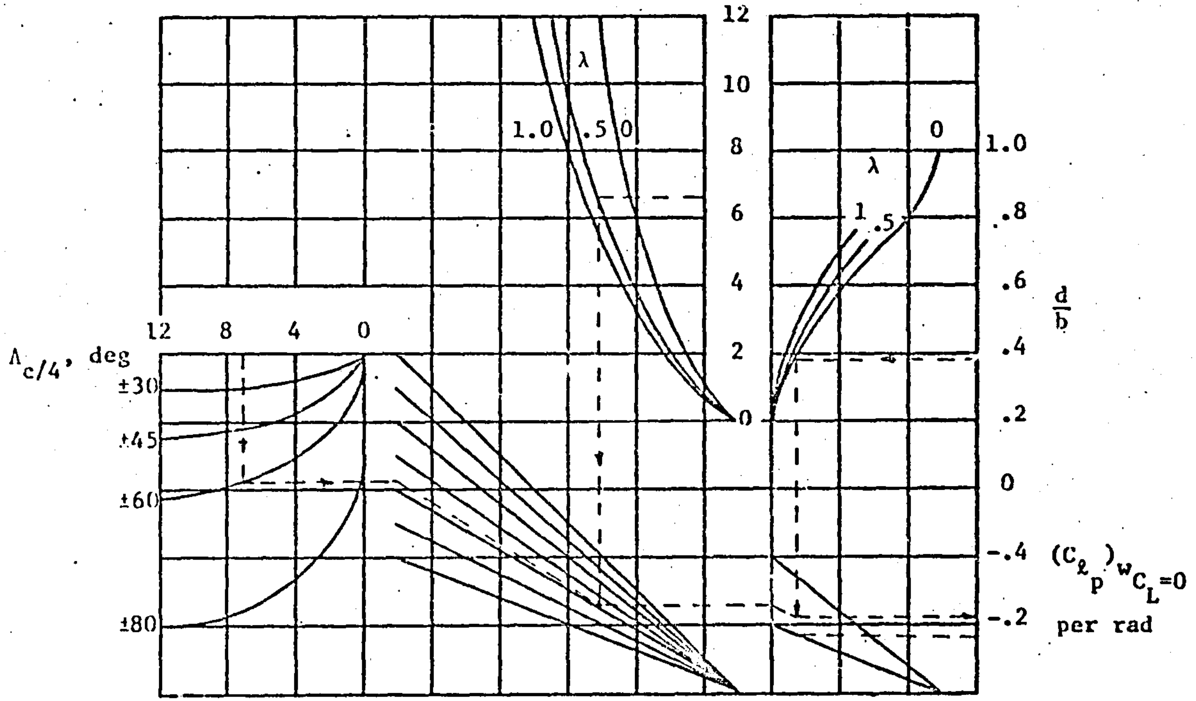

Figure 5.1.1.1: Zero lift wing and horizontal tail C_{ℓ_p}, including fuselage effects (Reference 3)

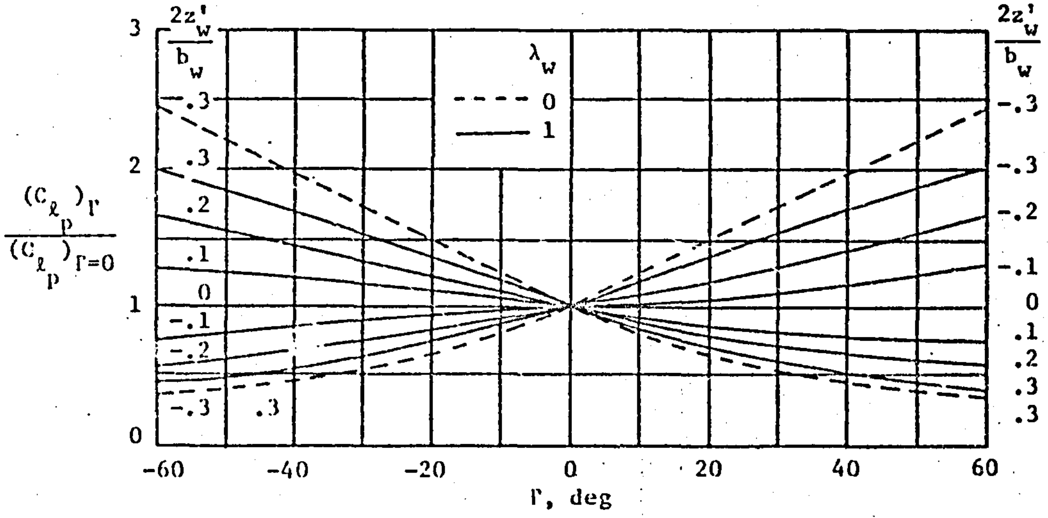

Figure 5.1.1.2: Dihedral contribution to C_{ℓ_p} (Reference 3)

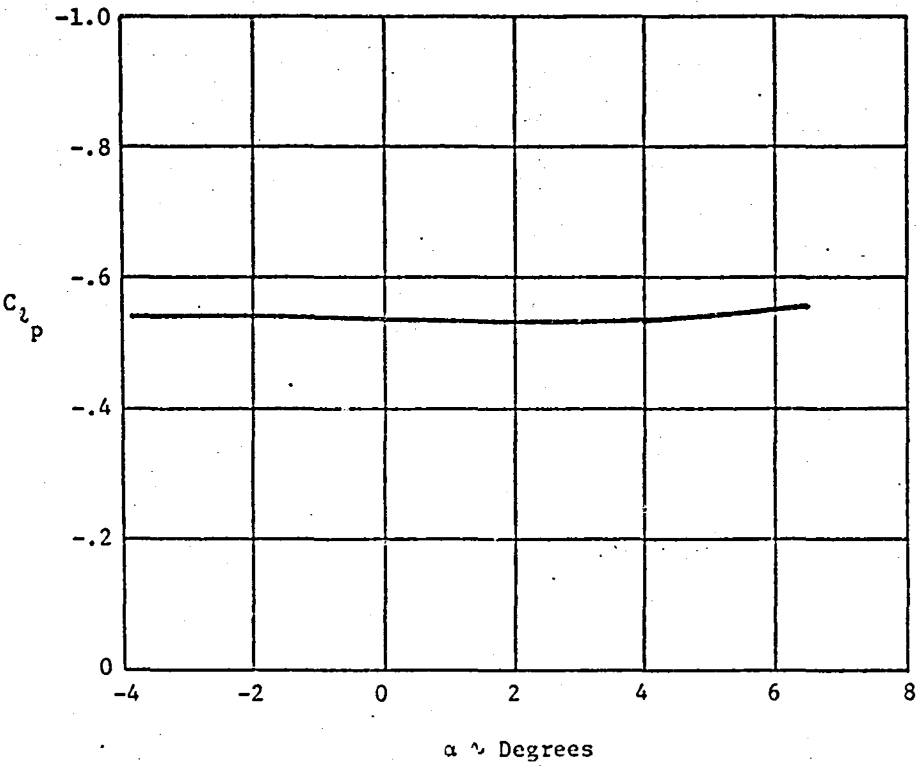

Figure 5.1.5.1: Predicted C_{ℓ_p} of the ATLIT Airplane
(propellers removed)

5.2 Yaw Damping Derivative, C_{n_r}

The yaw damping derivative is largely caused by the vertical tail and to some extent by the wing. The fuselage is of minor importance for conventional general aviation aircraft.

5.2.1 Wing Contribution to C_{n_r}

A wing undergoing yaw rate will experience asymmetric lift distributions due to changes in velocity. These lift changes cause induced drag changes which produce a yawing moment. Equation 5.2.1.1 from Reference 3 gives the incompressible wing contribution. However, the profile drag term, $(C_{D_o})_w$, should be at the appropriate Mach number.

$$(C_{n_r})_w = \left[\frac{(C_{n_r})_1}{{C_{L_w}}^2}\right] {C_{L_w}}^2 + \left[\frac{(\Delta C_{n_r})_2}{(C_{D_o})_w}\right] (C_{D_o})_w \qquad (5.2.1.1)$$

where

$\frac{(C_{n_r})_1}{{C_{L_w}}^2}$ accounts for the C_{n_r} due to induced forces resulting from yawing of an isolated wing about its aerodynamic center, obtained from Figure 5.2.1.1.

$\frac{(\Delta C_{n_r})_2}{(C_{D_o})_w}$ accounts for the unsymmetrical spanwise distribution of profile drag, obtained from Figure 5.2.1.2.

If the airplane c.g. does not coincide with the wing aerodynamic center, then the factor $(C_{n_r})_1/{C_{L_w}}^2$ must be corrected with the following increment:

$$\left[\frac{(\Delta C_{n_r})_1}{C_{L_w}^{\;2}}\right]_{\bar{x}} = -\left\{\left(\frac{4\cos\Lambda_{c/4}}{A_w + 4\cos\Lambda_{c/4}} + \frac{A_w}{2\cos\Lambda_{c/4}}\right)\frac{\bar{x}}{\bar{c}_w}\;\frac{\tan\Lambda_{c/4}}{A_w} + \right.$$

$$\left. + \frac{4\cos\Lambda_{c/4}}{A_w + 4\cos\Lambda_{c/4}}\left[4\left(\frac{\bar{x}}{\bar{c}_w}\right)^2\frac{\tan^2\Lambda_{c/4}}{A_w^{\;2}}\right]\right\}\left[\frac{(C_{n_r})_1}{C_{L_w}^{\;2}}\right]_{\Lambda_{c/4}=0} \qquad (5.2.1.2)$$

where

$\bar{x}$ is the longitudinal distance from the c.g. to the wing aerodynamic center.

$\left[\frac{(C_{n_r})_1}{C_{L_w}^{\;2}}\right]_{\Lambda_{c/4}=0}$ is the zero sweep wing damping parameter obtained from Figure 5.2.1.1 for $\Lambda_{c/4}=0$.

The general wing contribution equation is now

$$(C_{n_r})_w = C_{L_w}^2\left\{\left[\frac{(C_{n_r})_1}{C_{L_w}^2}\right]_{\bar{x}=0} + \left[\frac{(C_{n_r})_1}{C_{L_w}^2}\right]_{\bar{x}}\right\} + (C_{D_o})_w\left[\frac{(\Delta C_{n_r})_2}{(C_{D_o})_w}\right] \qquad (5.2.1.3)$$

For the ATLIT the c.g. was assumed to be at the wing aerodynamic center.

Table 5.2.1.1 summarizes the wing contribution to C_{n_r} for the ATLIT.

5.2.2 Fuselage Contribution to C_{n_r}

For conventional general aviation fuselages the fuselage contribution to C_{n_r} is small compared to the vertical tail. No analytical design method is presented to calculate $(C_{n_r})_f$.

5.2.3 Vertical Tail Contribution to C_{n_r}

The vertical tail is the primary contributor to C_{n_r}. Its effect comes from a straight restoring moment due to the sideslip induced by yaw rate and from the lag of wing-fuselage sidewash, $\frac{\partial\sigma}{\partial\frac{rb_w}{2V}}$. In general there is no method to calculate the oscillating sidewash, and in fact Reference 3 suggests that it may not be important. Assuming that the wing cancels the fuselage sidewash, the vertical tail C_{n_r} is given by Equation 5.2.3.1.

$$(C_{n_r})_v = -114.6(C'_{L_\alpha})_v\left(\frac{l_v \cos\alpha - z_v \sin\alpha}{b_w}\right) \qquad (5.2.3.1)$$

where
where $(C'_{L_\alpha})_v$, l_v, and z_v are defined the same as in Section 5.1.3.

Table 5.2.3.1 shows the summary calculations for the vertical tail C_{n_r} of the ATLIT airplane.

5.2.4 C_{n_r} of the ATLIT Airplane

The propeller-off C_{n_r} of the ATLIT airplane is given by Equation 5.2.4.1.

$$(C_{n_r})_{\substack{\text{prop}\\\text{off}}} = (C_{n_r})_w + (C_{n_r})_f + (C_{n_r})_v \qquad (5.2.4.1)$$

Table 5.2.4.1 summarizes the propeller-off C_{n_r} of the ATLIT Figure 5.2.4.1 shows C_{n_r} as a function of angle of attack. No wind tunnel data is available for comparison.

Table 5.2.1.1 Wing Contribution to C_{n_r}

Symbol	Description	Reference	Magnitude
A_w	Aspect ratio	Table 2.1.1	10.32
λ_w	Wing taper ratio	Table 2.1.1	0.50
$\Lambda_{c/4}$	Wing quarter-chord sweep angle, deg.	Table 2.1.1	1.835
$\bar{x}$	$\bar{x}_{a.c.} - \bar{x}_{c.g.}$	-	0
$\left[\frac{(C_{n_r})_1}{C_{L_w}^2}\right]_{\bar{x}=0}$	Wing lift damping parameter	Figure 5.2.1.1	-0.0143
$\left[\frac{(C_{n_r})_1}{C_{L_w}^2}\right]_{\Lambda_{c/4}=0}$	Zero sweep wing damping parameter	Figure 5.2.1.1	-
$\left[\frac{(\Delta C_{n_r})_2}{C_{L_w}^2}\right]$	Profile drag damping parameter	Figure 5.2.1.2	-0.289
C_{L_w}	Wing lift coefficient	Figure 4.1.1.1	variable
$(C_{D_o})_w$	Wing profile drag coefficient	Table 4.12.1.2 Reference 1	0.00907
Summary: $(C_{n_r})_w = -0.0143\ C_{L_w}^2 - 0.0028$ per rad			

Table 5.2.3.1: Vertical Tail Contribution to C_{n_r}

Symbol	Description	Reference	Magnitude
$(C_{L_\alpha}')_v$	Vertical tail effective lift curve slope, per deg	Table 4.5.1.1	0.00507
z_v	Vertical distance from the c.g. to the vertical tail mean aerodynamic chord, m (ft)	Figure 2.1.5	-1.22 (-4.0)
l_v	Horizontal distance from the c.g. to the quarter-chord of the vertical tail mean aerodynamic chord, m (ft)	Figure 2.1.5	4.50 (14.75)
b_w	Wing span, m (ft)	Table 2.1.1	12.19 (40.0)

α, deg	$(C_{n_r})_v$, per rad (Eq. 5.2.3.1)
-4	-0.0757
-2	-0.0774
0	-0.0790
2	-0.0804
4	-0.0816
15.9	-0.0848

Table 5.2.4.1: C_{n_r} of the ATLIT Airplane

α,deg	$(C_{n_r})_w$ (Table 5.2.1.1)	$(C_{n_r})_v$ Table 5.2.1.2	$(C_{n_r})_{\text{prop off}}$ (Eq. 5.2.4.1)
-4	-0.0028	-0.0757	-0.0785
-2	-0.0030	-0.0774	-0.0804
0	-0.0040	-0.0790	-0.0830
2	-0.0058	-0.0804	-0.0862
4	-0.0084	-0.0816	-0.0900
15.9	-0.0318	-0.0848	-0.1166

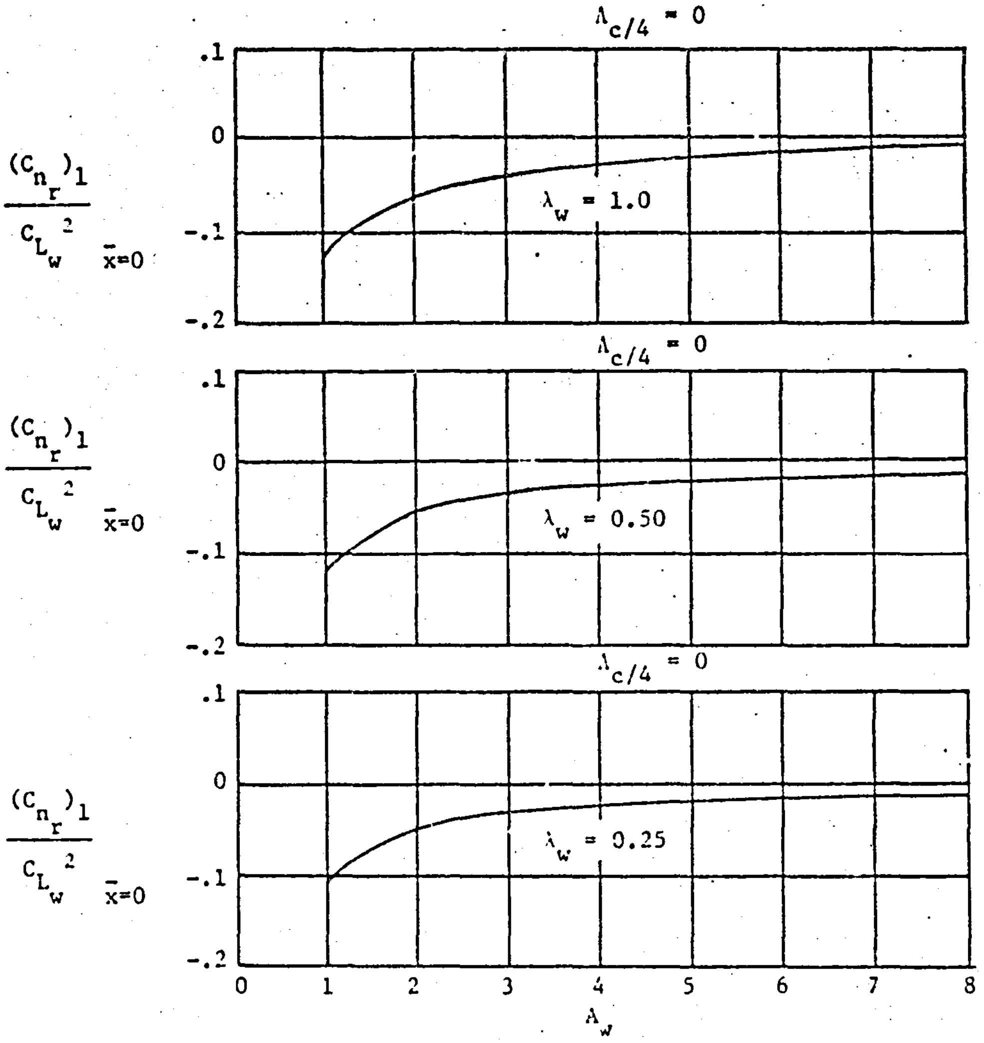

Figure 5.2.1.1: Wing contribution to C_{n_r} due to lift and induced drag with $\bar{x} = 0$ (Reference 3)

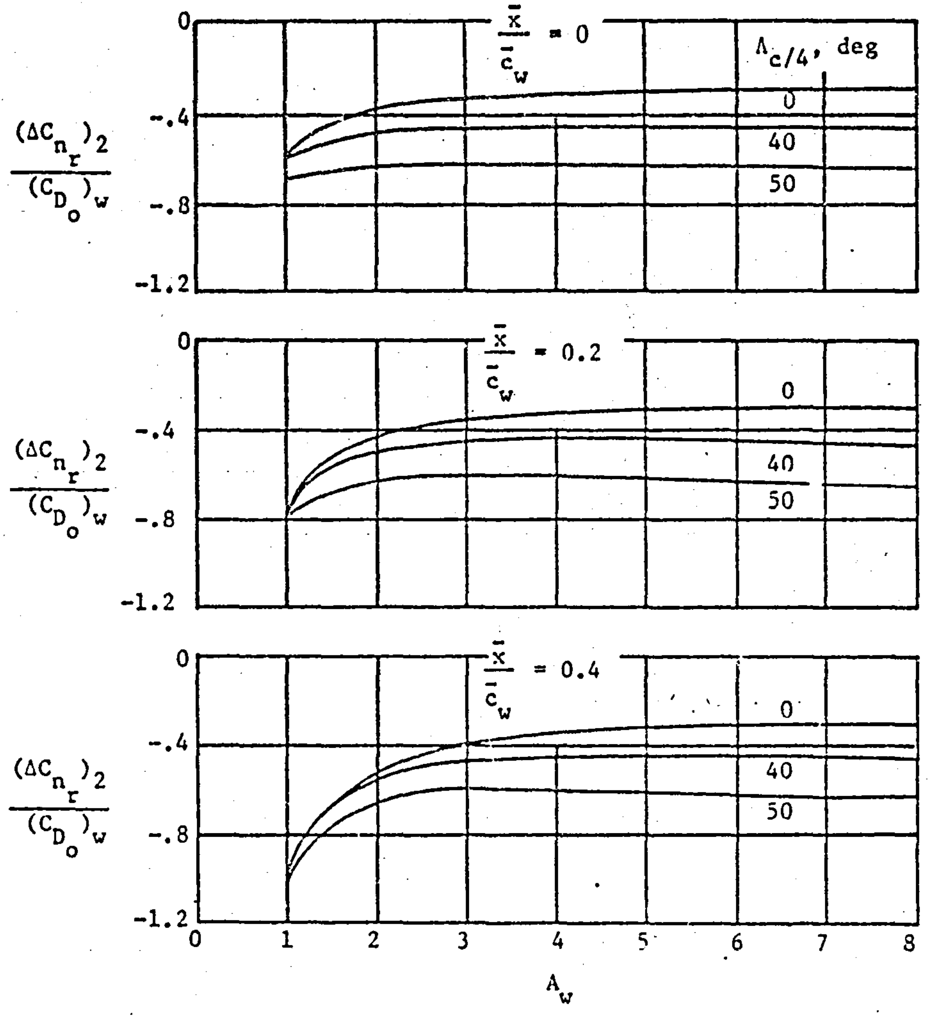

Figure 5.2.1.2: Increment in C_{n_r} due to wing profile drag for $0.5 < \lambda > 1.0$ (Reference 3)

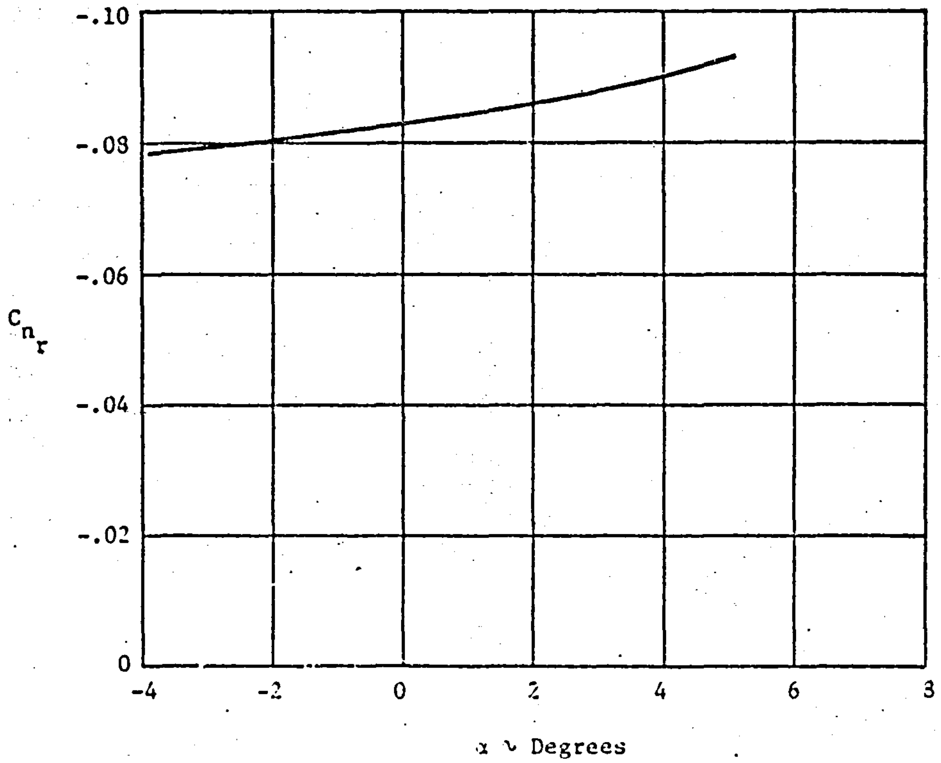

Figure 5.2.4.1: Predicted C_{n_r} of the ATLIT Airplane
(propellers removed)

5.3 Roll Due to Yaw Rate Derivative, C_{ℓ_r}

Rolling moment due to yaw rate is mainly affected by the wing and vertical tail only for airplanes of conventional fuselage shape. Therefore only wing and vertical tail effects are calculated.

5.3.1 Wing Contribution to C_{ℓ_r}

The wing contribution to C_{ℓ_r} is produced by the spanwise lift differential produced by the yaw rate. For unswept wings, C_{ℓ_r} is linear with lift until $C_{L_{MAX}}$. There is also an increment due to geometric dihedral. For zero Mach number, the wing C_{ℓ_r} is given by Equation 5.3.1.1 from Reference 3.

$$(C_{\ell_r})_w = \left(\frac{C_{\ell_r}}{C_{L_w}}\right)_{\Gamma=0} C_{L_w} + \left(\frac{\Delta C_{\ell_r}}{\Gamma}\right) \frac{\Gamma}{57.3} \qquad (5.3.1.1)$$

where

$\left(\frac{C_{\ell_r}}{C_{L_w}}\right)_{\Gamma=0}$ is the compressible change in C_{ℓ_r} due to wing lift obtained from Equation 5.3.1.2.

$$\left(\frac{C_{\ell_r}}{C_{L_w}}\right)_{\Gamma=0} = \frac{1 + \frac{A_w(1 - B_2)^2}{2B_2(A_wB_2 + 3\cos\Lambda_{c/4})} + \left(\frac{A_wB_2 + 2\cos\Lambda_{c/4}}{A_wB_2 + 4\cos\Lambda_{c/4}}\right)\left(\frac{\tan^2\Lambda_{c/4}}{8}\right)}{1 + \frac{A_w + 2\cos\Lambda_{c/4}}{A_w + 4\cos\Lambda_{c/4}}\left(\frac{\tan^2\Lambda_{c/4}}{8}\right)} \frac{C_{\ell_r}}{C_{L_w}}\Bigg|_{\Gamma=M=0} \qquad (5.3.1.2)$$

where

$\left(\frac{C_{\ell_r}}{C_{L_w}}\right)_{\Gamma=M=0}$ is obtained from Figure 5.3.1.1.

$$B_2 = \sqrt{1 - M^2\cos^2\Lambda_{c/4}}$$

The dihedral increment is obtained from Equation 5.3.1.3.

$$\frac{\Delta C_{\ell_r}}{\Gamma} = \frac{1}{12}\left[\frac{\pi A_w \sin \Lambda_{c/4}}{A_w + 4 \cos \Lambda_{c/4}}\right] \qquad (5.3.1.3)$$

The valid lift range of Figure 5.3.1.1 is dependent upon sweep angle. For conventional unswept general aviation airplanes, it is usable throughout the linear lift range. Also note that this procedure ignores the effect of center of gravity location. In general there does not appear to be enough data to account for this effect.

Table 5.3.1.1 summarizes the calculations of wing C_{ℓ_r} for the ATLIT airplane.

5.3.2 Vertical Tail Contributions to C_{ℓ_r}

Excluding the effects of sidewash, $\frac{\partial\sigma}{\partial \frac{rb_w}{2v}}$, as in Section 5.2.3 the aperiodic contribution of the vertical tail to C_{ℓ_r} can be obtained from Equation 5.3.2.1 from Reference 3. These calculations are summarized in Table 5.3.2.1 for the ATLIT airplane.

$$(C_{\ell_r})_v = -114.6(C'_{L_\alpha})_v \left(\frac{z_v \cos\alpha + l_v \sin\alpha}{b_w}\right)\left(\frac{l_v \cos\alpha - z_v \sin\alpha}{b_w}\right) \qquad (5.3.2.1)$$

where $(C'_{L_\alpha})_v$, z_v, and l_v are defined the same as in Section 5.1.3.

5.3.3 C_{ℓ_r} of the ATLIT Airplane

The propeller-off C_{ℓ_r} of the ATLIT airplane is given by Equation 5.3.3.1.

$$(C_{\ell_r})_{\substack{\text{prop}\\\text{off}}} = (C_{\ell_r})_w + (C_{\ell_r})_v \qquad (5.3.3.1)$$

Table 5.3.3.1 summarizes the propeller-off C_{ℓ_r} of the ATLIT. Figure 5.3.3.1 shows C_{ℓ_r} as a function of angle of attack.

Table 5.3.1.1: Wing Contribution to C_{ℓ_r}

Symbol	Description	Reference	Magnitude
M	Mach number	-	0.018
A_w	Wing aspect ratio	Table 2.1.1.1	10.32
λ_w	Wing taper ratio	Table 2.1.1	0.50
$\Lambda_{c/4}$	Wing quarter-chord sweep angle, deg	Table 2.1.1	1.835
Γ	Wing dihedral, deg	Table 2.1.1	7
C_{L_w}	Wing lift coefficient	Figure 4.1.1.1	variable
$\left(\frac{C_{\ell_r}}{C_{L_w}}\right)_{\Gamma=M=0}$	Wing contribution to C_{ℓ_r} for $M=\Gamma=0$	Figure 5.3.1.1	0.240
$\left(\frac{C_{\ell_r}}{C_{L_w}}\right)_{\Gamma=0}$	Wing contribution to C_{ℓ_r} for $\Gamma=0$	Equation 5.3.1.2	0.240
$\frac{C_{\ell_r}}{\Gamma}$	Dihedral contribution to C_{ℓ_r}	Equation 5.3.1.3	0.00074
Summary: $(C_{\ell_r})_w = 0.24\ C_{L_w} + 0.00074$ per rad			

Table 5.3.2.1: Vertical Tail Contribution to C_{l_r}

Symbol	Description	Reference	Magnitude
$(C_{L_\alpha}')_v$	Vertical tail effective lift curve slope, per deg	Table 4.5.1.1	0.00507
z_v	Vertical distance from the c.g. to the vertical tail mean aerodynamic chord, m (ft)	Figure 2.1.5	-1.22 (-4.0)
l_v	Horizontal distance from the c.g. to the quarter-chord of the vertical tail mean aerodynamic chord, m (ft)	Figure 2.1.5	4.50 (14.75)
b_w	Wing span, m (ft)	Table 2.1.1	12.19 (40.0)

α, deg	$(C_{l_r})_v$, per rad (Eq. 5.3.2.1)
-4	0.0263
-2	0.0239
0	0.0214
2	0.0138
4	0.0161
15.9	-0.0011

Table 5.3.3.1: C_{ℓ_r} of the ATLIT Airplane

α, deg	$(C_{\ell_r})_w$ (Table 5.3.1.1)	$(C_{\ell_r})_v$ (Table 5.3.2.1)	$(C_{\ell_r})_{\text{prop off}}$ (Eq. 5.3.3.1)
-4	-0.0121	0.0263	0.0142
-2	0.0306	0.0239	0.0545
0	0.0732	0.0214	0.0946
2	0.1158	0.0113	0.1346
4	0.1584	0.0161	0.1745
15.9	0.3593	-0.0011	0.3582

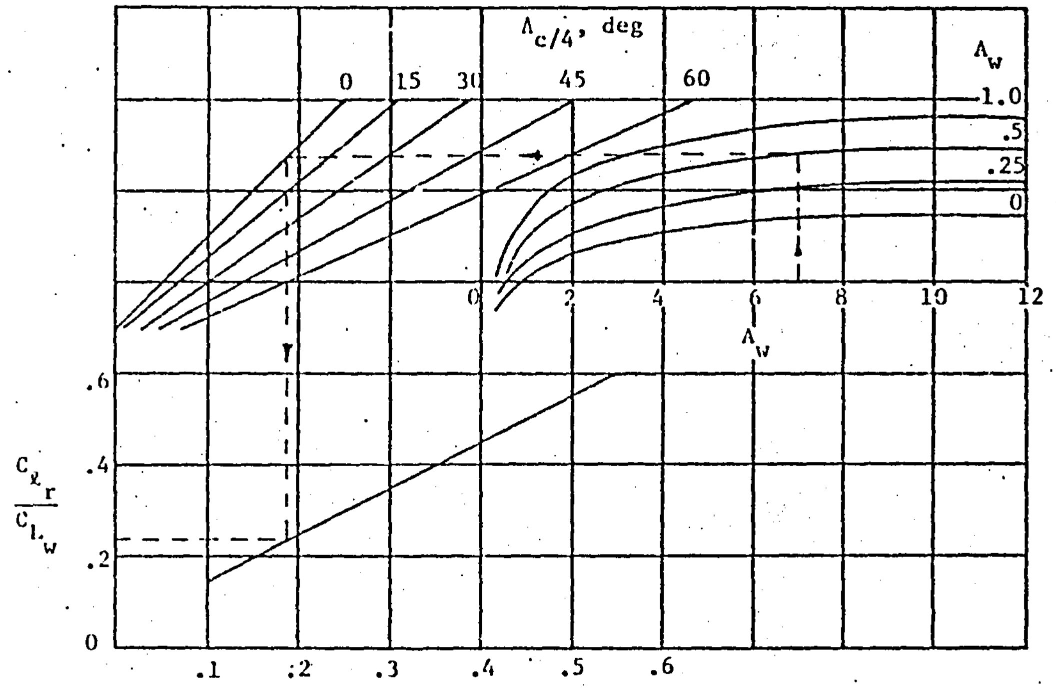

Figure 5.3.1.1: Wing contribution to C_{ℓ_r} for zero dihedral and incompressible speeds.

(Reference 3)

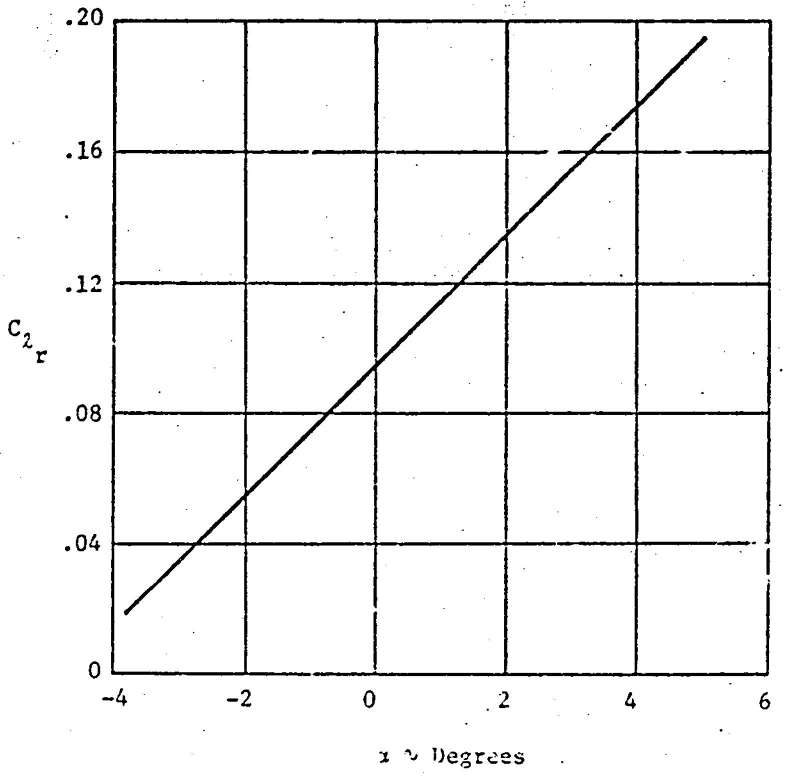

Figure 5.3.3.1: Predicted C_{ℓ_r} of the ATLIT Airplane (propellers removed)

5.4 Yaw Due to Roll Rate Derivative, C_{n_p}

In this analysis only the effects of the wing and vertical tail are calculated, since they are the predominating contributors to C_{n_p}.

5.4.1 Wing Contribution to C_{n_p}

Wing rolling produces antisymmetrical lift loading which causes a yawing moment due to induced drag. Additionally roll-induced changes in angle of attack produce a change in viscous drag. Also dihedral effects are considered separate. Equation 5.4.1.1 from Reference 3 gives the wing contribution.

$$(C_{n_p})_w = \left[\frac{(C_{n_p})_1}{C_{L_w}}\right]_{\Gamma=0} C_{L_w} + \left(\frac{\Delta C_{n_p}}{\Gamma}\right)\frac{\Gamma}{57.3} + \left(\frac{\Delta C_{n_p}}{\frac{\partial C'_{D_o}}{\partial\alpha}}\right)\frac{\partial C'_{D_o}}{\partial\alpha} \qquad (5.4.1.1)$$

where

$\left[\frac{(C_{n_p})_1}{C_{L_w}}\right]_{\Gamma=0}$ is the zero dihedral contribution of the antisymmetrical lift and induced drag. This term is obtained from Equation 5.4.1.2 from Reference 3 which accounts for tip suction effects and center of gravity location.

$$\left.\frac{C_{n_{p_1}}}{C_{L_w}}\right|_{\Gamma=M=0} = \frac{A_w+4}{A_w+\cos\Lambda_{c/4}}\left[1+6\left(1+\frac{\cos\Lambda_{c/4}}{A_w}\right)\left(\frac{\bar{x}}{\bar{c}_w}\frac{\tan\Lambda_{c/4}}{A_w}+\frac{\tan^2\Lambda_{c/4}}{12}\right)\right]\left[\frac{(C_{n_p})_1}{C_{L_w}}\right]_{\Lambda_{c/4}=0} + \frac{1}{4A_w}\left(\tan\Lambda_{c/4}+\frac{1}{A_w}\right) - \frac{1}{A_w^2}\frac{\bar{x}}{\bar{c}_w} \qquad (5.4.1.2)$$

where

$\left[\frac{(C_{n_p})_1}{C_{L_w}}\right]_{\Lambda_{c/4}=0}$ is found from Figure 5.4.1.2

To correct for compressibility effects, Equation 5.4.1.3 is used.

$$\left[\frac{(C_{n_p})_1}{C_{L_w}}\right]_{\Gamma=0} = \left(\frac{A_w + 4\cos\Lambda_{c/4}}{A_w B_2 + 4\cos\Lambda_{c/4}}\right)\left(\frac{A_w B_2 + \frac{1}{2}(A_w B_2 + \cos\Lambda_{c/4})\tan^2\Lambda_{c/4}}{A_w + \frac{1}{2}(A_w + \cos\Lambda_{c/4})\tan^2\Lambda_{c/4}}\right)\left[\frac{(C_{n_p})_1}{C_{L_w}}\right]_{\Gamma=M=0} \qquad (5.4.1.3)$$

where

$$B_2 = \sqrt{1 - M^2\cos^2\Lambda_{c/4}}$$

To account for dihedral, Equation 5.4.1.4 from Reference 3 is used.

$$\left(\frac{\Delta C_{n_p}}{\Gamma}\right) = -\left(\frac{\tan\Lambda_{c/4}}{4} + \frac{3}{A_w}\,\frac{\bar{x}}{\bar{c}_w}\right)(C_{\ell_p})_{\Gamma=0} \qquad (5.4.1.4)$$

where $(C_{\ell_p})_{\Gamma=0}$ is from Section 5.1.1 with compressibility effects included.

The viscous drag parameter $\dfrac{\Delta C_{n_p}}{\dfrac{\partial C'_{D_o}}{\partial \alpha}}$ in Equation 5.4.1.1 is found from Figure 5.4.1.2. The second viscous drag term $\dfrac{\partial C'_{D_o}}{\partial \alpha}$ is found by plotting viscous drag versus angle of attack, as shown in Figure 5.4.1.3, and graphically determining the slopes. An analytical method is presented in Appendix A. Reference 3 points out the importance of including the viscous drag contribution to C_{n_p} in obtaining good correlation with wind-tunnel results.

Table 5.4.1.1 summarizes the wing contribution to C_{n_p}.

5.4.2 Vertical Tail Contribution to C_{n_p}

The vertical tail contribution is given by Equation 5.4.2.1 from Reference 3, where all terms are as defined in Section 5.1.3.

$$(C_{n_p})_v = -57.3(C_{L_\alpha}{}')_v \left(\frac{l_v\cos\alpha + z_v\sin\alpha}{b_w}\right)\left[\frac{2(z_v\cos\alpha + l_v\sin\alpha)}{b_w} + \frac{\partial\sigma}{\partial\frac{pb_w}{2V}}\right] \quad (5.4.2.1)$$

Table 5.4.2.1 summarizes the vertical tail contribution to C_{n_p} for the ATLIT airplane.

5.4.3 C_{n_p} of the ATLIT Airplane

Considering the wing and vertical tail as the only significant contributors, C_{n_p} is given in Equation 5.4.3.1.

$$(C_{n_p})_{\substack{prop\\off}} = (C_{n_p})_w + (C_{n_p})_v$$

The calculations are summarized in Table 5.4.3.1 and plotted as a function of angle of attack in Figure 5.4.3.1. No wind tunnel data is available for comparison.

Table 5.4.1.1: Wing Contribution to C_{n_p}

Symbol	Description	Reference	Magnitude
M	Mach number	-	0.018
B_2	$1-M^2\cos^2\Lambda_{c/4}$	-	0.997
A_w	Wing aspect ratio	Table 2.1.1	10.32
λ_w	Wing taper ratio	Table 2.1.1	0.50
$\Lambda_{c/4}$	Wing quarter-chord sweep angle, deg	Table 2.1.1	1.835
b_w	Wing span, m (ft)	Table 2.1.1	12.19 (40.0)
$\bar{c}_w$	Wing mean aerodynamic chord, m (ft)	Table 2.1.1	1.225 (4.018)
$\bar{x}$	$\bar{x}_{a.c.} - \bar{x}_{c.g.}$	-	0
$\frac{(C_{n_p})_1}{C_{L_w}}_{\Lambda=0}$	Zero sweep damping parameter	Figure 5.4.1.1	-0.372
$\frac{(C_{n_p})}{C_{L_w}}_{\Gamma=0}$	Zero dihedral damping parameter	Equation 5.4.1.3	-0.0752
$\frac{\Delta C_{n_p}}{\Gamma}$	Dihedral contribution to C_{n_p}	Equation 5.4.1.4	0.0042
$\frac{\Delta C_{n_p}}{\frac{\partial C_{D_0}'}{\partial \alpha}}$	Viscous drag parameter	Figure 5.4.1.2	2.059
$\frac{\partial C_{D_0}'}{\partial \alpha}$	Viscous drag rate of change	Figure 5.4.1.3	variable

α, deg	$(C_{n_p})_w$, per rad (Eq. 5.4.1.2)
-4	0.30432
-2	-0.30834
0	-0.32219
2	-0.33155
4	-0.36060
10.0	-0.39514

Table 5.4.2.1: Vertical Tail Contribution to C_{n_p}

Symbol	Description	Reference	Magnitude
$(C_{L_\alpha}')_v$	Vertical tail effective lift curve slope, per deg	Table 4.5.1.1	0.00507
z_v	Vertical distance from the c.g. to the vertical tail mean aerodynamic chord, m (ft)	Figure 2.1.5	-1 22 (-4.0)
l_v	Horizontal distance from the c.g. to the quarter-chord of the mean aerodynamic chord of the vertical tail, m (ft)	Figure 2.1.5	4.50 (14.75)
b_w	Wing span, m (ft)	Table 2.1.1	12.19 (40.0)
$\frac{\partial\alpha}{\partial\frac{pb_w}{2V}}$	Rate of change of sidewash with wing tip helix angle	-	0.20

α, deg	$(C_{n_p})_v$, per rad (Eq. 5.4.2.1)
-4	0.00198
-2	0.00272
0	0
2	-0.00280
4	-0.00567
15.9	-0.02333

Table 5.4.3.1: C_{n_p} of the ATLIT Airplane

α, deg	$(C_{n_p})_w$ (Table 5.4.1.1)	$(C_{n_p})_v$ (Table 5.4.2.1)	$(C_{n_p})_{\text{prop off}}$
-4	0.00452	0.00198	0.00650
-2	-0.00884	0.00272	-0.00612
0	-0.02219	0	-0.02219
2	-0.03355	-0.00280	-0.03635
4	-0.04690	-0.00567	-0.05257
15.9	-0.09534	-0.02333	-0.11367

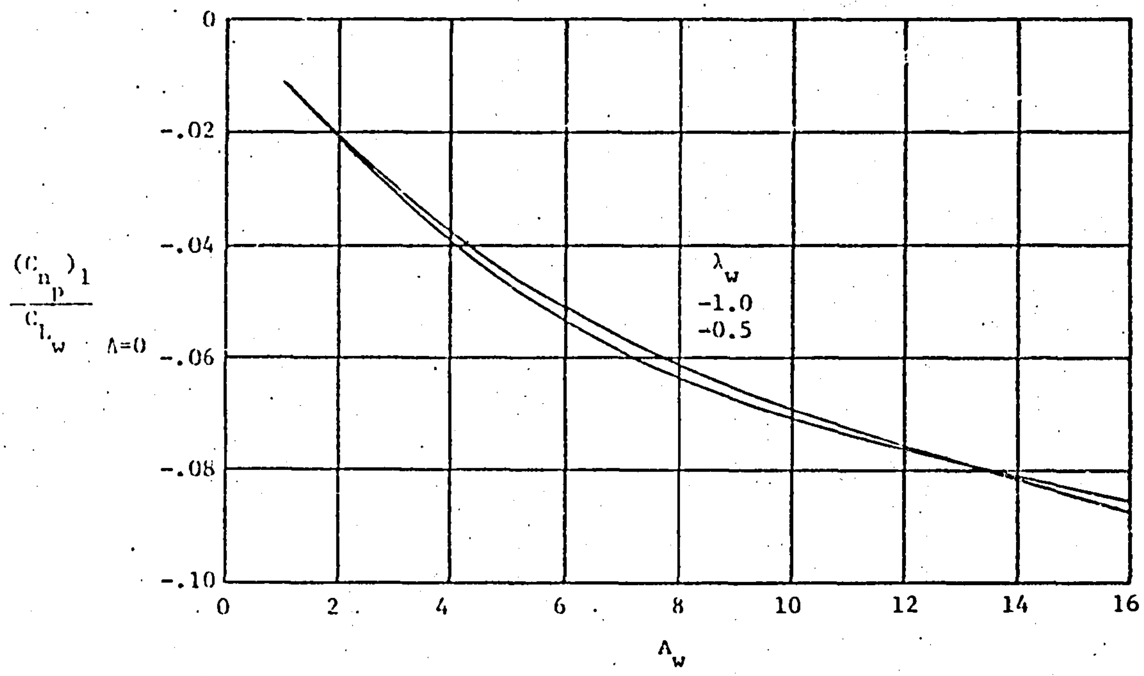

Figure 5.4.1.1: Wing contribution to C_{n_p} for unswept wings due to antisymmetrical lift and induced drag (Reference 3)

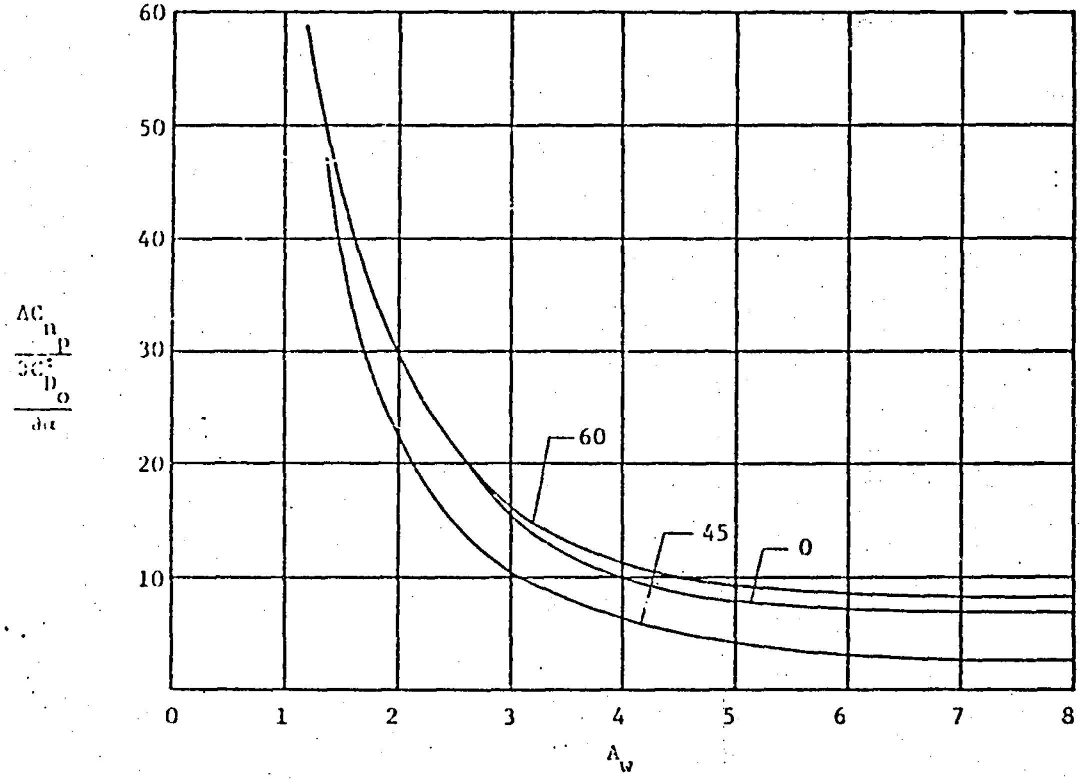

Figure 5.4.1.2: Increment in C_{n_p} due to wing viscous drag (Reference 3)

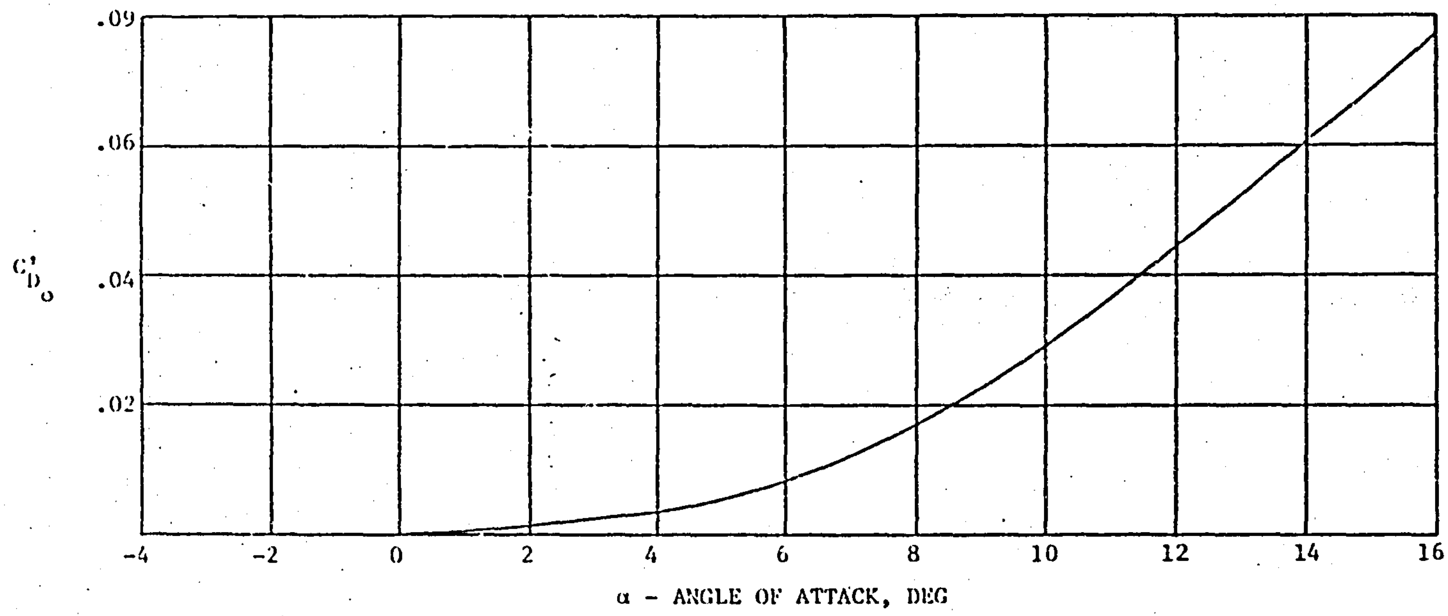

Figure 5.4.1.3: Variation of viscous drag with angle of attack for ATLIT (Reference 3)

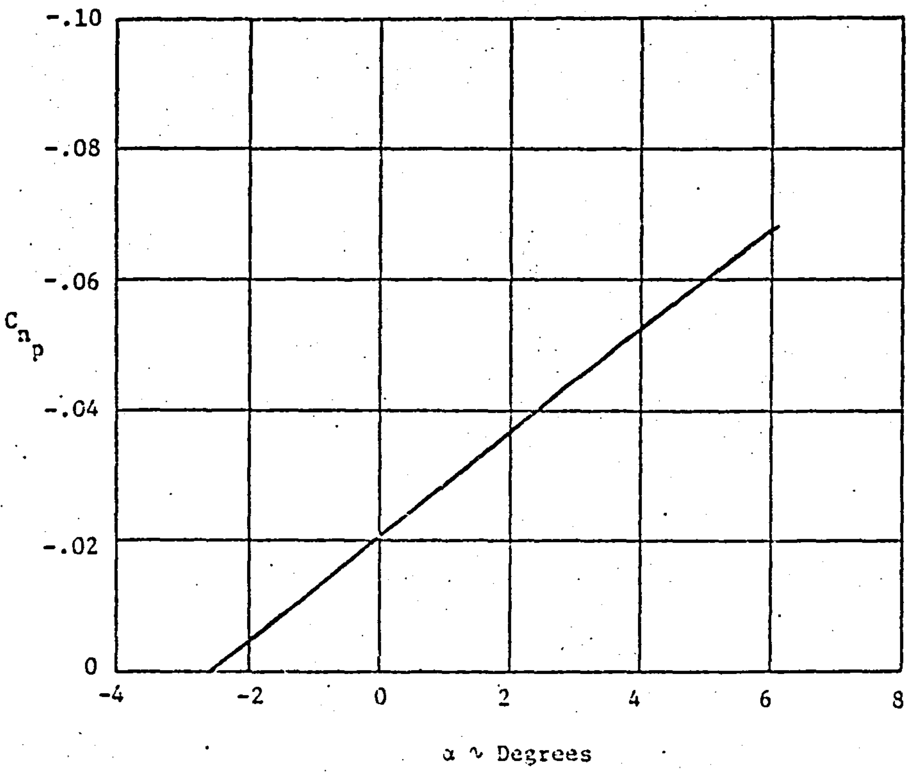

Figure 5.4.3.1: Predicted C_{n_p} of the ATLIT Airplane (propellers removed)

CHAPTER 6

PREDICTION OF POWER-ON AERODYNAMIC CHARACTERISTICS

The effects of power especially from a propeller operation can have a significant effect on the aerodynamic characteristics of an airplane. Due to the highly interactive nature of the propeller slipstream, there are usually a number of effects that must be considered. Power effects are considered at three power settings: $T_c'=0$, $T_c'=.0195$, $T_c'=.1970$, where $T_c'=\text{Thrust}/\bar{q}_\infty S_w$.

6.1 Propeller Power Effects on Static Stability Characteristics

For conventional twin engine airplanes the vertical tail is assumed to be outside the propeller slipstream. Therefore the propellers are assumed to produce no sidewash or dynamic pressure change at the vertical tail.

6.1.1 Power Effects on C_{Y_β}

The contribution of power to C_{Y_β} is given in Equation 6.1.1.1.

$$(\Delta C_{Y_\beta})_{power} = (\Delta C_{Y_\beta})_{N_p} + (\Delta C_{Y_\beta})_{n(\Delta\bar{q})} + (\Delta C_{Y_\beta})_{n(\sigma_p)} \qquad (6.1.1.1)$$

where

$(\Delta C_{Y_\beta})_{N_p}$ is the normal side force caused by the propellers

$(\Delta C_{Y_\beta})_{n(\Delta\bar{q})}$ is the change in nacelle C_{Y_β} due to the increased dynamic pressure

$(\Delta C_{Y_\beta})_{n(\sigma_p)}$ is the change in nacelle C_{Y_β} due to power induced sidewash at the nacelle.

The normal force contribution $(\Delta C_{Y_\beta})_{N_p}$ is given by Equation 6.1.1.2 from Reference 3.

$$(\Delta C_{Y_\beta})_{N_p} = -\frac{nf}{57.3}(C_{N_\alpha})_p\left(\frac{S_p/\text{prop}}{S_w}\right) \qquad (6.1.1.2)$$

where

n is number of propellers

f is the propeller inflow factor, obtained from Figure 6.1.1.1

S_p/prop is the disc area of each propeller

$(C_{N_\alpha})_p$ is the normal force parameter at $T'_c=0$ given by Equation 6.1.1.3 from Reference 3.

$$(C_{N_\alpha})_p = (C_{N_\alpha})_{p_{K_N=80.7}}\left[1 + .8\left(\frac{K_N}{80.7}\right) - 1\right] \qquad (6.1.1.3)$$

where

K_N is the empirical normal force factor of the propeller given by

$$K_N = 262\left(\frac{b_p}{R_p}\right)_{0.3R_p} + 262\left(\frac{b_p}{R_p}\right)_{0.6R_p} + 135\left(\frac{b_p}{R_p}\right)_{0.9R_p} \qquad (6.1.1.4)$$

where $\left(\frac{b_p}{R_p}\right)$ is the ratio of blade width to propeller radius at the given propeller radius stations.

$[(C_{n_\alpha})_p]_{K_N=80.7}$ is the normal coefficient at $K_N=80.7$ obtained from Figure 6.1.1.2 as a function of blade angle β'.

The change in C_{Y_β} of the nacelles due to increased dynamic pressure is given by Equation 6.1.1.5 from Reference 3.

$$(\Delta C_{Y_\beta})_{n(\Delta\bar{q})} = [(C_{Y_\beta})_n]_{\substack{\text{prop}\\\text{off}}}\frac{\Delta\bar{q}_n}{\bar{q}_\infty} \qquad (6.1.1.5)$$

where

$[(\Delta C_{Y_\beta})_n]_{\substack{\text{prop}\\ \text{off}}}$ is nacelle contribution with propellers off as determined in Section 4.1.3

$\frac{\Delta \bar{q}_n}{\bar{q}_\infty}$ is the increase in dynamic pressure at the nacelle due to power given by

$$\frac{\Delta \bar{q}_n}{\bar{q}_\infty} = \frac{S_w(T_c'/\text{prop})}{\pi R_p^{\,2}} \tag{6.1.1.6}$$

The effect of propeller induced sidewash on the nacelle contribution is given by Equation 6.1.1.7 from Reference 3.

$$(\Delta C_{Y_\beta})_{n(\sigma_p)} = -[(\Delta C_{Y_\beta})_n]_{\substack{\text{prop}\\ \text{off}}} \left(\frac{\partial \sigma_p}{\partial \beta}\right)\left(1 + \frac{\Delta \bar{q}_n}{\bar{q}_\infty}\right) \tag{6.1.1.7}$$

where

$\frac{\partial \sigma_p}{\partial \beta}$ is the change in propeller induced sidewash with sideslip given by

$$\frac{\partial \sigma_p}{\partial \beta} = C_1 + C_2\ (C_{N_\alpha})_p \tag{6.1.1.8}$$

where C_1 and C_2 are obtained from Figure 6.1.1.3.

Table 6.1.1.1 (a) - (c) summarizes the effects of power on C_{Y_β} of the ATLIT airplane. The power on C_{Y_β} is given by

$$C_{Y_\beta} = (C_{Y_\beta})_{\substack{\text{prop}\\ \text{off}}} + (\Delta C_{Y_\beta})_{\text{power}} \tag{6.1.1.9}$$

Table 6.1.1.1 (d) gives the power on C_{Y_β} of the ATLIT. Figure 6.1.1.4 presents this data as a function of angle of attack and power setting, T_c'. Also the calculated values are compared with wind-tunnel results.

6.1.2 Power Effects on C_{n_β}

The effect of power on C_{n_β} is due to power-induced changes in C_{Y_β}. The same factors are assumed in the power increment.

$$(\Delta C_{n_\beta})_{power} = (\Delta C_{n_\beta})_{N_p} + (\Delta C_{n_\beta})_{n(\Delta\bar{q})} + (\Delta C_{n_\beta})_{n(\sigma_p)} \qquad (6.1.2.1)$$

The propeller normal side force increment, $(\Delta C_{n_\beta})_{N_p}$, is given by Equation 6.1.2.2.

$$(\Delta C_{n_\beta})_{N_p} = (\Delta C_{Y_\beta})_{N_p} \left(\frac{x_p \cos\alpha + z_p \sin\alpha}{b_w}\right) \qquad (6.1.2.2)$$

where

$(\Delta C_{n_\beta})_{N_p}$ is the increment in C_{Y_β} due to propeller normal force, from Section 6.1.1

x_p is the longitudinal distance from the ptopeller to the airplane c.g.

z_p is the vertical distance from the thrust line to the airplane c.g.

b_w is the wing span.

Since the two nacelle increments, $(\Delta C_{n_\beta})_{n(\Delta\bar{q})}$ and $(\Delta C_{n_\beta})_{n(\sigma_p)}$, act through the same moment arm, their effect can be considered together.

$$(\Delta C_{n_\beta})_{n(\Delta\bar{q})}+(\Delta C_{n_\beta})_{n(\sigma_p)}=[(\Delta C_{Y_\beta})_{n(\Delta\bar{q})}+(\Delta C_{Y_\beta})_{n(\sigma_p)}]\left(\frac{x_n\cos\alpha+z_n\sin\alpha}{b_w}\right) \qquad (6.1.2.3)$$

where

$(\Delta C_{Y_\beta})_{n(\Delta\bar{q})}$ and $(\Delta C_{Y_\beta})_{n(\sigma_p)}$ are the power increments to C_{Y_β} due to the nacelles, obtained from Section 6.1.1

x_n is the longitudinal distance from the nacelle center of pressure to the airplane c.g., from Figure 2.1.4

z_n is the vertical distance from the nacelle center of pressure to the airplance c.g., from Figure 2.1.4.

The total airplane C_{n_β} is

$$(C_{n_\beta}) = (C_{n_\beta})_{\substack{\text{prop}\\\text{off}}} + (\Delta C_{n_\beta})_{\text{power}} \qquad (6.1.2.4)$$

Table 6.1.2.1 presents the summary calculations for the ATLIT airplane. Figure 6.1.2.1 gives total C_{n_β} as a function of angle of attack and power setting, comparing it with wind tunnel results.

6.1.3 Power Effects on C_{ℓ_β}

Two power effects on C_{ℓ_β} are considered. The first is caused by the normal force produced by the propeller. The second is the result of the lateral shift of the portion of the wing immersed in the propeller slipstream. Equation 6.1.3.1 gives the total power increment.

$$(\Delta C_{\ell_\beta})_{\text{power}} = (\Delta C_{\ell_\beta})_{N_p} + (\Delta C_{\ell_\beta})_{(\Delta\bar{q} + \epsilon_p)} \qquad (6.1.3.1)$$

where

$(\Delta C_{\ell_\beta})_{N_p}$ is the propeller normal side force increment given by Equation 6.1.3.2.

$$(\Delta C_{\ell_\beta})_{N_p} = (\Delta C_{Y_\beta})_{N_p} \left(\frac{-z_p \cos\alpha + x_p \sin\alpha}{b_w} \right) \qquad (6.1.3.2)$$

where all terms are the same as in Equation 6.1.2.2.

When the airplane is yawed, the center of pressure of the wing shifts proportional to $\tan(\beta - \sigma_p)$. On one wing the shift will be inboard, while on the opposite wing the shift will be outboard. The net result is a rolling moment. Equation 6.1.3.3, from Reference 3, gives the increment.

$$(\Delta C_{\ell_\beta})_{(\Delta\bar{q}+\epsilon_p)} = \left(\frac{1}{2}\right) \frac{1}{57.3} \frac{x_p'}{b_w} \left[(\Delta C_L)_{w_{(\Delta\bar{q})}} + (\Delta C_L)_{w_{(\epsilon_p)}}\right]\left(1 - \frac{\partial\sigma_p}{\partial\beta}\right) \qquad (6.1.3.3)$$

where

the factor 1/2 accounts for fuselage interference effects

x_p' is the distance from the propeller to the wing quarter-chord along the thrust line

b_w is the wing span

$(\Delta C_L)_{w(\Delta\bar{q})}$ is the increase in lift due to power-induced increased dynamic pressure, obtained from Table 5.1.3.2, of Reference 1

$(\Delta C_L)_{w(\epsilon_p)}$ is the increment in lift due to power-induced downwash, obtained from Table 5.1.3.2 of Reference 1

$\frac{\partial\sigma_p}{\partial\beta}$ is the power-induced sidewash from Equation 6.1.1.8.

Table 6.1.2.1 presents the summary calculations for the ATLIT airplane. Total airplane C_{ℓ_β} is:

$$C_{\ell_\beta} = (C_{\ell_\beta})_{\substack{\text{prop}\\\text{off}}} + (\Delta C_{\ell_\beta})_{\text{power}} \qquad (6.1.3.4)$$

Figure 6.1.3.1 gives total C_{ℓ_β} as a function of angle of attack and power setting and compares it with wind-tunnel results.

6.1.4 Rudder Control

As previously mentioned, it is assumed that the vertical tail is outside the propeller slipstream and is not affected by power settings. As a result, there is no predicted change in $C_{\ell_{\delta_R}}$, $C_{n_{\delta_R}}$, or $C_{Y_{\delta_R}}$ with power. Figure 6.1.4.1 shows the full-scale wind-tunnel results for the power effect on rudder control derivatives. As shown, it appears that there is very little power interaction.

6.1.5 Spoiler Control

For an airplane with ailerons, the effect of power on roll control should be small. For spoilers it depends on the proximity of the spoilers to the propeller slipstream. For the ATLIT airplane, the portion of the spoiler immersed in the slipstream is quite small at low angle of attack, and none of the spoiler is immersed at higher angles of attack. (For data on the immersed span as a function of power and angle of attack, see Table 5.1.3.2 of Reference 1.) For this reason it was assumed that the effect of power would be small. In addition there is no wind tunnel data that gives the isolated effect of power. The spoiler derivatives were therefore assumed not to vary with power setting.

Table 6.1.1.1(a): Increment of C_{Y_β} Due to Propeller Normal Force, $(\Delta C_{Y_\beta})_{N_p}$

Symbol	Description	Reference	Magnitude
n	Number of propellers	-	2
R_p	Propeller radius, m (ft)	Table 2.1	0.97 (3.17)
b_p	Width of propeller blade, m (ft)	-	0.127 (0.417) at .3 R_p 0.157 (0.515) at .6 R_p 0.108 (0.354) at .9 R_p
Sp/prop	Propeller disc area, πR_p^2, m^2 (ft^2)	-	2.93 (31.57)
$\frac{S_w(T_c'/prop)}{8 R_p^2}$	Propeller correlation parameter	-	variable
f	Propeller inflow parameter	Figure 6.1.1.1	variable
K_n	Propeller side force parameter	Equation 6.1.1.4	
β'	Propeller blade angle, deg	-	variable
$(C_{N_\alpha})_{p\ K_N=80.7}$	Propeller normal force parameter	Figure 6.1.1.2	variable
$(C_{N_\alpha})_p$	Propeller normal force derivative	Equation 6.1.1.3	variable

T_c'	$(C_{N_\alpha})_p$ (Eq. 6.1.1.3)	$(\Delta C_{Y_\beta})_{N_p}$ (Eq. 6.1.1.2)
0	0.10	-0.0007
0.0915	0.10	-0.0008
[illegible]	0.10	-0.0008

Table 6.1.1.2(b): Change in Nacelle C_{Y_β} Due to Increased Dynamic Pressure, $(\Delta C_{Y_\beta})_{n(\Delta\bar{q})}$

Symbol	Description	Reference	Magnitude
$(\Delta C_{Y_\beta})_{n\ \text{prop off}}$	Propeller off nacelle contribution to C_{Y_β}, per deg	Table 4.1.3.1	-0.000476
$\dfrac{\Delta\bar{q}_n}{\bar{q}_\beta}$	Power induced change in nacelle dynamic pressure	Equation 6.1.1.6	variable

T'_c	$\dfrac{\Delta\bar{q}_n}{\bar{q}_\infty}$ (Eq. 6.1.1.6)	$(\Delta C_{Y_\beta})_{n(\Delta\bar{q})}$, per deg (Eq. 6.1.1.5)
0	0	0
0.0915	0.2249	-0.000107
0.1970	0.4836	-0.000230

Table 6.1.1.1(c): Change in Nacelle C_{Y_β} Due to Propeller Sidewash, $(\Delta C_{Y_\beta})_{n(\sigma_p)}$

Symbol	Description	Reference	Magnitude
$(\Delta C_{Y_\beta})_{n_{\text{prop off}}}$	Propeller off nacelle contribution to C_{Y_β}, per deg	Table 4.1.3.1	-0.000476
$\frac{\partial \sigma_p}{\partial \beta}$	Change in propeller sidewash with sideslip	Equation 6.1.1.8	variable
C_1, C_2	Propeller sidewash factors	Figure 6.1.1.3	variable
$\frac{\Delta \bar{q}_n}{\bar{q}_\infty}$	Power induced change in nacelle dynamic pressure	Equation 6.1.1.6	variable

T_c'	$\frac{\partial \sigma_p}{\partial \beta}$ (Eq. 6.1.1.8)	$\frac{\Delta \bar{q}_n}{\bar{q}_\infty}$ (Eq. 6.1.1.6)	$(\Delta C_{Y_\beta})_{n(\sigma_p)}$, per deg (Eq. 6.1.1.7)
0	0.025	0	0.000012
0.0915	0.1033	0.2249	0.000060
0.1970	0.1554	0.4836	0.000110

Table 6.1.1.1(d): Power-on C_{Y_β} of the ATLIT Airplane

T_c'	$(C_{Y_\beta})_{\text{prop off}}$ (Table 4.1.5.1)	$(\Delta C_{Y_\beta})_{N_p}$ (Table 6.1.1.1(a))	$(\Delta C_{Y_\beta})_{n(\Delta \bar{q})}$ (Table 6.1.1.1(b))	$(\Delta C_{Y_\beta})_{n(\sigma_p)}$ (Table 6.1.1.1(c))	$(C_{Y_\beta})_{\text{power on,}}$ per d (Eq. 6.1.1
0	-0.00977	-0.0007	0	0.000012	-0.01046
0.0915	-0.00977	-0.0008	-0.000107	0.000060	-0.01062
0.1970	-0.00977	-0.0008	-0.000230	0.000110	-0.01069

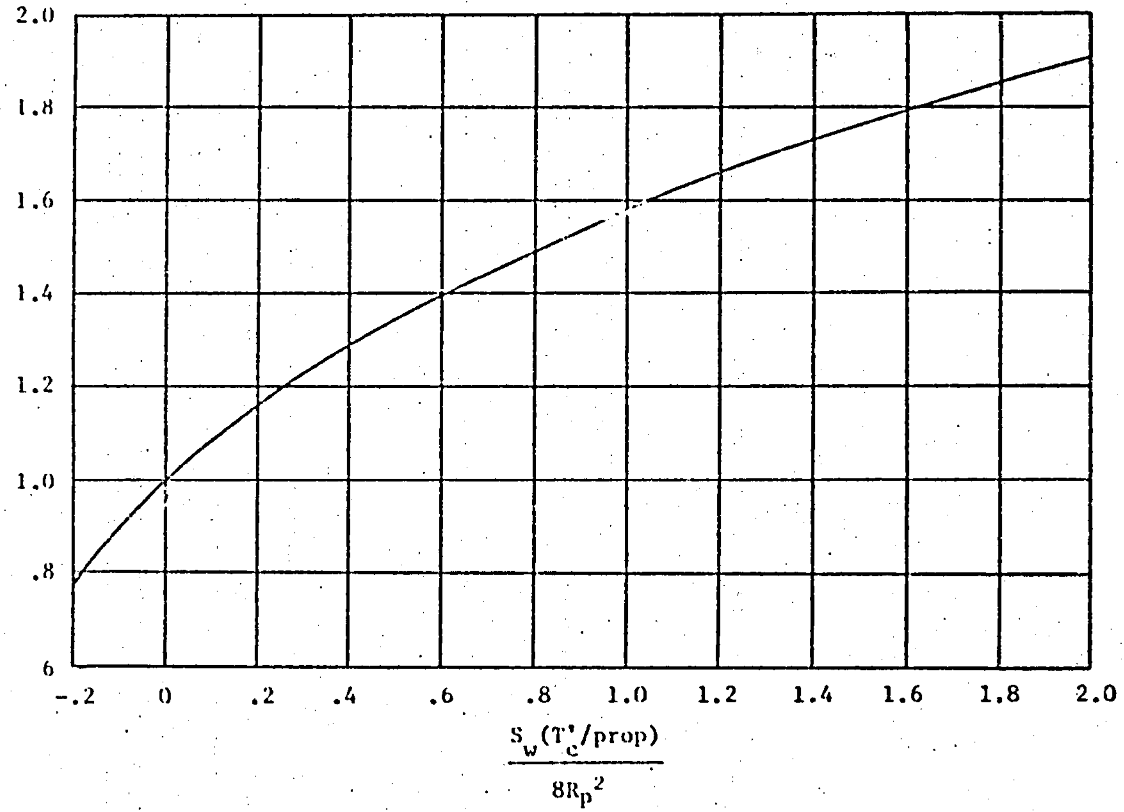

Figure 6.1.1.1: Propeller inflow factor (Reference 3)

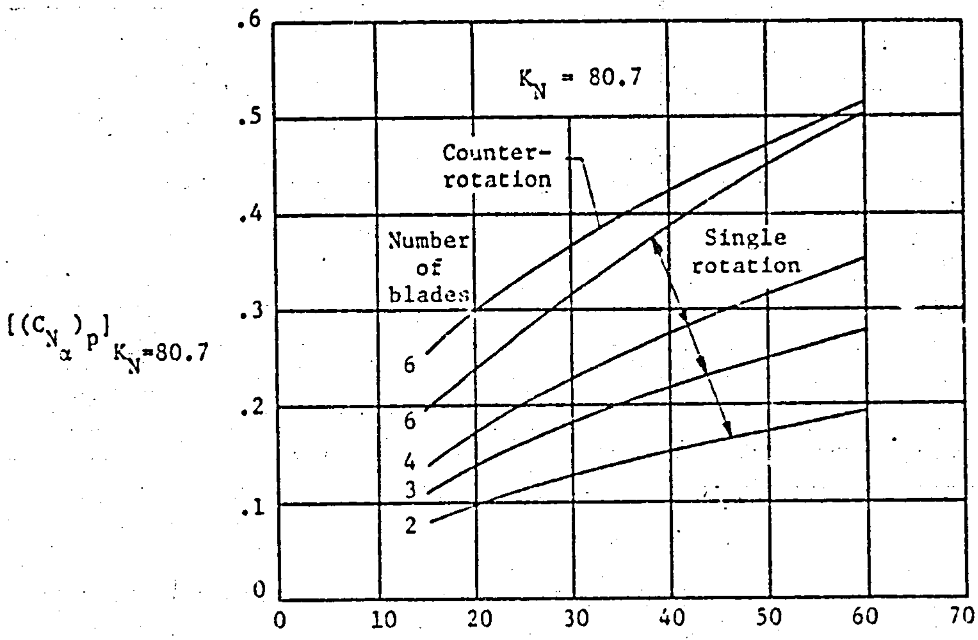

Figure 6.1.1.2: Propeller normal force parameter (Reference 3)

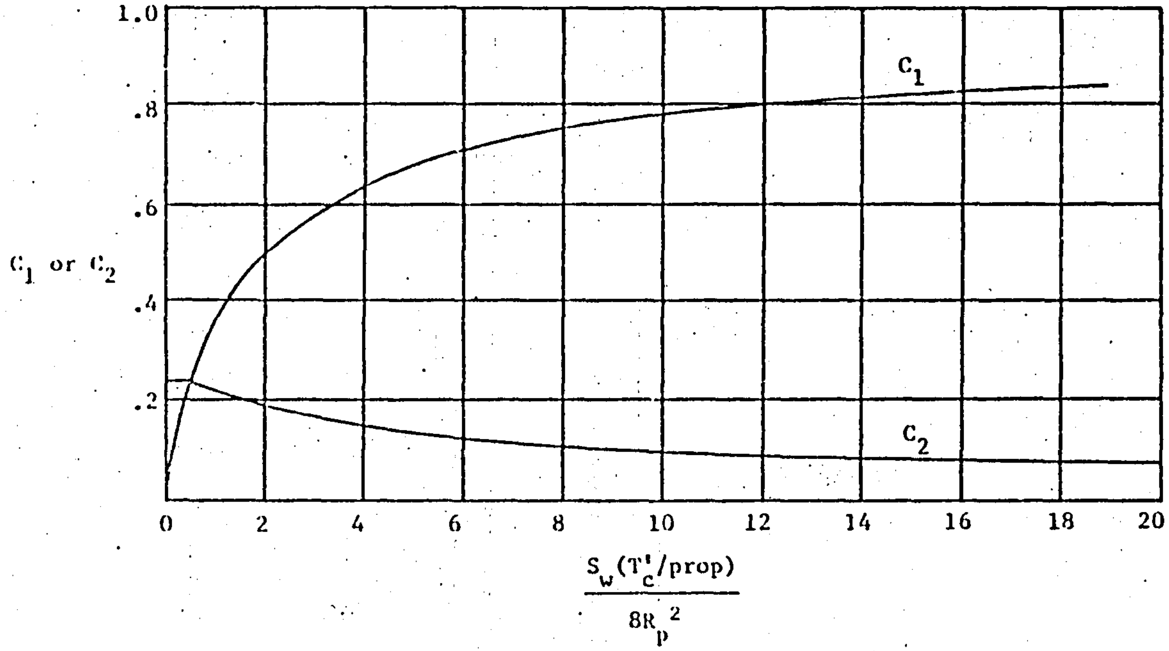

Figure 6.1.1.3: Factors for determining propeller downwash (Reference 3)

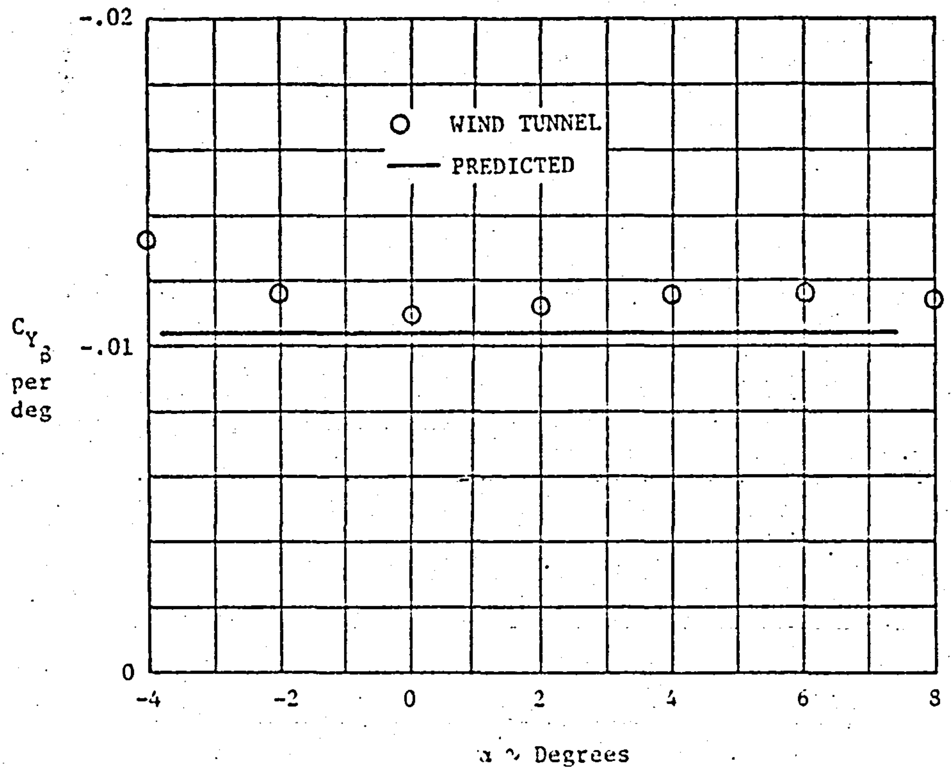

Figure 6.1.1.4: Comparison of predicted power-on C_{Y_β} with wind tunnel data (T'_c = .1970)

Table 6.1.2.1: Power-on C_{n_β} of the ATLIT Airplane

Symbol	Description	Reference	Magnitude
$(\Delta C_{Y_\beta})_{N_p}$	Propeller normal side force derivative, per deg	Table 6.1.1.1	variable
x_p	Longitudinal distance from the propeller to the c.g., m (ft)	Figure 2.1.4	2.10 (6.89)
z_p	Vertical distance from the propeller to the c.g., m (ft)	Figure 2.1.4	-0.127 (-0.417)
b_w	Wing span, m (ft)	Table 2.1.1	12.19 (40.0)
$(\Delta C_{Y_\beta})_{n(\Delta\bar{q})}$	Change in nacelle C_{Y_β} due to increased dynamic pressure, per deg	Table 6.1.1.1	variable
$(\Delta C_{Y_\beta})_{n(\sigma_p)}$	Change in nacelle C_{Y_β} due to propeller sidewash, per deg	Table 6.1.1.1	variable
x_n	Longitudinal distance from nacelle center of pressure to airplane c.g., m (ft)	Figure 2.1.4	0.97 (3.17)
z_n	Vertical distance from nacelle center of pressure to airplane c.g., m (ft)	Figure 2.1.4	-0.15 (-0.50)

α, deg	$(C_{n_\beta})_{\text{prop off}}$	$(\Delta C_{n_\beta})_{N_p}$			$(\Delta C_{n_\beta})_{n(\Delta\bar{q})}+(\Delta C_{n_\beta})_{n(\sigma_p)}$			$(C_{n_\beta})_{\text{power on}}$		
		T'_c			T'_c			T'_c		
		0	0.0915	0.1970	0	0.0915	0.1970	0	0.0915	0.1970
-4	0.00189	-0.0001	-0.0001	-0.0001	0	0	-0.00001	0.00179	0.00179	0.00178
-2	0.00190	-0.0001	-0.0001	-0.0001	0	0	-0.00001	0.00180	0.00180	0.00179
0	0.00191	-0.0001	-0.0001	-0.0001	0	0	-0.00001	0.00181	0.00181	0.00180
2	0.00195	-0.0001	-0.0001	-0.0001	0	0	-0.00001	0.00185	0.00185	0.00184
4	0.00194	-0.0001	-0.0001	-0.0001	0	0	-0.00001	0.00184	0.00184	0.00183

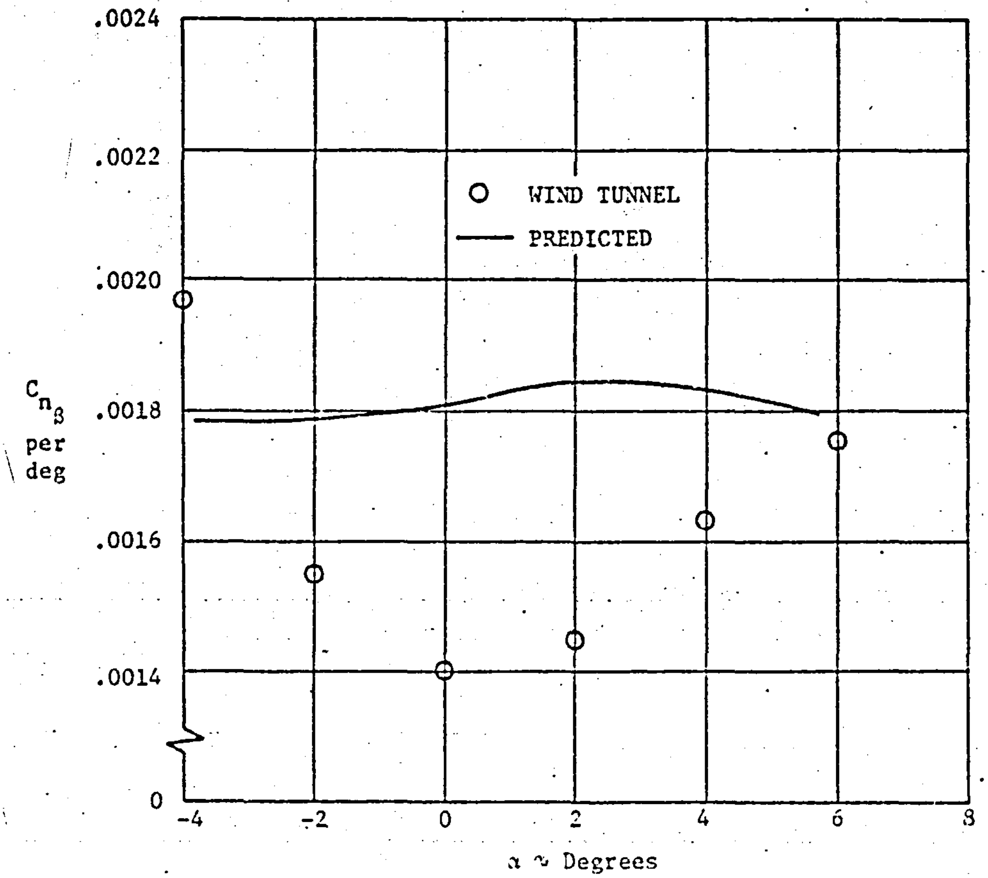

Figure 6.1.2.4: Comparison of predicted power-on C_{n_β} with wind tunnel data on the ATLIT Airplane ($T_c' = .1970$)

Table 6.1.3.1: Power on C_{ℓ_β} of the ATLIT Airplane

Symbol	Description	Reference	Magnitude
$(\Delta C_{Y_\beta})_{N_p}$	Propeller normal side force derivative, per deg.	Table 6.1.1.1	variable
z_p	Longitudinal distance from the propeller to the c.g., m (ft)	Figure 2.1.4	2.10 (6.59)
x_p	Vertical distance from the propeller to the c.g., m (ft)	Figure 2.1.4	-0.127 (-0.417)
b_w	Wing span, m (ft)	Table 2.1.1	12.19 (40.0)
x'_p	Distance along thrust line from the propeller to the wing quarter-chord, m (ft)	Figure 2.1.4	
$(\Delta C_L)_{w(\Delta\bar{q})}$	Increase in lift due to power-induced increased dynamic pressure	Table 5.1.3.2 Reference 1	variable
$(\Delta C_L)_{w(\varepsilon_p)}$	Increment in lift due to power-induced downwash	Table 5.1.3.2 Reference 1	variable
$\frac{\partial\sigma_p}{\partial\beta}$	Power-induced sidewash derivative	Equation 6.1.1.8	variable

α, deg	$(C_{\ell_\beta})_{\text{prop off}}$	$(\Delta C_{\ell_\beta})_{N_p}$			$(\Delta C_{\ell_\beta})_{(\Delta\bar{q}+\varepsilon_p)}$			$(C_{\ell_\beta})_{\text{power on}}$		
		T'_c			T'_c			T'_c		
		0	0.0915	0.1970	0	0.0915	0.1970	0	0.0915	0.1970
-4	-0.00212	~0	~0	~0	0	0.0001	0.0002	-0.00212	-0.00202	-0.00192
-2	-0.00209	~0	~0	~0	0	0.0002	0.0004	-0.00209	-0.00189	-0.00169
0	-0.00206	-0.00001	-0.00001	-0.00001	0	0.0003	0.0005	-0.00207	-0.00177	-0.00157
2	-0.00203	-0.00001	-0.00001	-0.00001	0	0.0003	0.0007	-0.00204	-0.00174	-0.00134
4	-0.00200	-0.00002	-0.00002	-0.00002	0	0.0004	0.0008	-0.00202	-0.00162	-0.00122
5.9	-0.00174	-0.00004	-0.00004	-0.00004	0	0.0004	0.0009	-0.00178	-0.00138	-0.00088

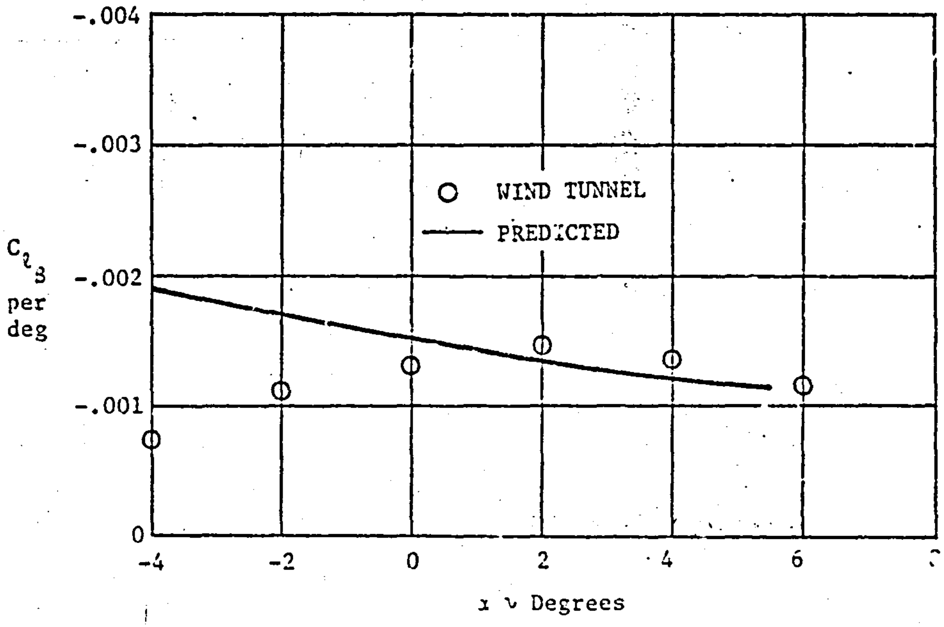

Figure 6.1.3.1: Comparison of predicted power-on C_{l_β} with wind tunnel data on the ATLIT Airplane (T'_c = .1970)

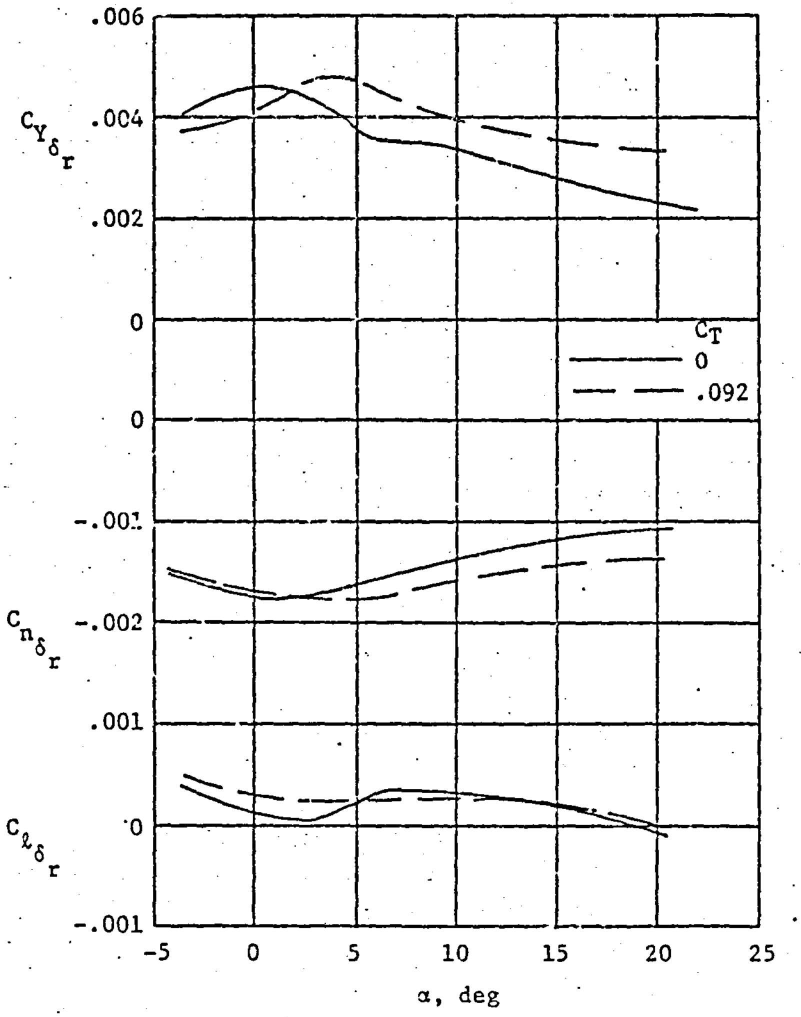

Figure 6.1.4.1: Effect of power on rudder derivatives from full scale wind-tunnel tests (Reference 2)

6.2 Propeller Power Effects on Dynamic Derivatives

6.2.1 Power Effects on C_{ℓ_p}

The power increment on C_{ℓ_p} is caused by the propeller normal force, the change in dynamic pressure over the immersed sections of the airplane and the change in downwash in the slipstream. The power-induced normal force contribution is given in Equation 6.2.1.1.

$$(\Delta C_{\ell_p})_{N_p} = -114.6 (C_{L_\alpha})_{N_p} \left(\frac{y_T}{b_w}\right)^2 \qquad (6.2.1.1)$$

where

$(C_{L_\alpha})_{N_p}$ is the lift curve slope of the propeller normal force obtained from Figure 6.2.1.1 (from Table 5.1.3.1 of Reference 1)

y_T is the lateral distance from the thrust line to the airplane center of gravity

b_w is the wing span.

The increment in wing C_{ℓ_p} due to power is given by Equation 6.2.1.2 from Reference 3.

$$\begin{aligned}(\Delta C_{\ell_p})_{w(\Delta\bar{q} + \epsilon_p)} &= (\Delta C_{\ell_p})_{w(\Delta\bar{q})} + (\Delta C_{\ell_p})_{w(\epsilon_p)} \\ &= -114.6 \left[(\Delta C_{L_\alpha})_{w(\Delta\bar{q})} + (\Delta C_{L_\alpha})_{w(\epsilon_p)}\right] \left(\frac{y_T}{b_w}\right)^2\end{aligned} \qquad (6.2.1.2)$$

where

$(\Delta C_{L_\alpha})_{w(\Delta\bar{q})}$ is the change in lift curve slope due to the power-induced change in dynamic pressure obtained from Figure 6.2.1.2 (from Table 5.1.3.2 of Reference 1)

$(\Delta C_{L_\alpha})_{w(\epsilon_p)}$ is the change in lift curve slope due to the power-induced change in downwash obtained from Figure 6.2.1.3 (from Table 5.1.3.2 of Reference 1).

The change in nacelle C_{ℓ_p} with power is given by Equation 6.2.1.3 from Reference 3.

$$(\Delta C_{\ell_p})_{n(\Delta\bar{q}+\epsilon_p)} = (\Delta C_{\ell_p})_{n(\Delta\bar{q})} + (\Delta C_{\ell_p})_{n(\epsilon_p)}$$

$$= (C_{\ell_p})_{n_{\substack{\text{prop}\\\text{off}}}} \left[\frac{\Delta\bar{q}}{\bar{q}_\infty} - \left\{ \frac{\dfrac{\partial\epsilon_p}{\partial\alpha_p}}{1-\dfrac{\partial\epsilon_u}{\partial\alpha_w}} \right\} \left(1+\frac{\Delta\bar{q}}{\bar{q}_\infty}\right) \right] \qquad (6.2.1.3)$$

where

$(C_{\ell_p})_{n_{\substack{\text{prop}\\\text{off}}}}$ is the propeller off nacelle contribution from Section 5.1.4.

$\frac{\Delta\bar{q}}{\bar{q}_\infty}$ is the increment in dynamic pressure behind the propeller obtained from Table 5.1.3.2 of Reference 1.

$\frac{\partial\epsilon_p}{\partial\alpha_p}$ is the rate of change of propeller downwash with propeller angle of attack, obtained from Table 5.1.3.2 of Reference 1.

$\frac{\partial\epsilon_u}{\partial\alpha}$ is the propeller upwash gradient obtained from Table 5.1.3.1 of Reference 1.

Total airplane C_{ℓ_p} is

$$C_{\ell_p} = (C_{\ell_p})_{\substack{\text{prop}\\\text{off}}} + (\Delta C_{\ell_p})_{w(\bar{q}+\epsilon_p)} + (\Delta C_{\ell_p})_{n(\Delta\bar{q}+\epsilon_p)} \qquad (6.2.1.4)$$

Table 6.2.1.1 summarizes the power effects on the ATLIT airplane. Figure 6.2.1.4 shows total C_{ℓ_p} as a function of angle of attack and power setting. There is no wind-tunnel data available for comparison.

6.2.2 Power Effects on C_{n_r}

No analytical methods of computing the power increment to C_{n_r} were found. In Reference 3, the C_{n_r} variation with power was deduced by comparing with wind-tunnel data on a similar model. The same percentage change in C_{n_r} with power for the model was assumed.

This procedure is highly empirical and cannot readily be extended to other aircraft. A comparison of the prediction of Reference 3 with flight test data shows poor correlation. In view of this and due to the fact that no experimental ATLIT data is yet available, the power effect on C_{n_r} is not predicted for the ATLIT.

6.2.3 Power Effects on C_{ℓ_r}

Reference 3 shows that the effect of power on C_{ℓ_r} is due mainly to wing contributions and that even this effect is negligible (of the order of 1%). For this reason the power effects of C_{ℓ_r} are not computed for the ATLIT and are assumed zero.

6.2.4 Power effects on C_{n_p}

Due to a lack of design data and for the same reasons as those outlined above, the power effect on C_{n_p} for the ATLIT airplane is assumed zero.

Table 6.2.1.1: Power-on C_{ℓ_p} of the ATLIT Airplane

Symbol	Description	Reference	Magnitude
$(C_{L_\alpha})_{N_p}$	Lift curve slope of the propeller normal force	Figure 6.2.1.1	variable
y_T	Lateral distance from thrust line to airplane c.g., m (ft)	Figure 2.1.1	1.89 (6.21)
b_w	Wing span, m (ft)	Table 2.1.1	12.19 (40.0)
$(\Delta C_{L_\alpha})_{w(\Delta\bar{q})}$	Change in wing lift curve slope due to power-induced change in dynamic pressure	Figure 6.2.1.2	variable
$(\Delta C_{L_\alpha})_{w(\varepsilon_p)}$	Change in wing lift curve slope due to propeller downwash	Figure 6.2.1.3	variable
$\frac{\Delta\bar{q}}{\bar{q}_\infty}$	Change in dynamic pressure behind the propeller	Table 5.1.3.2 Reference 1	variable
$(C_{\ell_p})_{n_{\text{prop off}}}$	Propeller off C_{ℓ_p} of the nacelles	Table 5.1.4.1	variable
$\frac{\partial\varepsilon_n}{\partial\alpha_p}$	Rate of change of propeller downwash with propeller angle of attack	Table 5.1.3.2 Reference 1	
$\frac{\partial\varepsilon_u}{\partial\alpha}$	Propeller upwash gradient	Table 5.1.3.1 Reference 1	-.155

α, deg	$(C_{\ell_p})_{\text{prop off}}$ (Table 5.1.5.1)	$(\Delta C_{\ell_p})_{N_p}$ (Eq. 6.2.1.1)			$(\Delta C_{\ell_p})_{w(\Delta q + \varepsilon_p)}$ (Eq. 6.2.1.2)		
		T'_c			T'_c		
		0	.0915	.1970	0	.0915	.1970
-4	-0.5398	-0.00099	-0.00110	-0.00121	0.00083	-0.0153	-0.0367
-2	-0.5391	-0.00099	-0.00110	-0.00121	0.00083	-0.0152	-0.0340
0	-0.5388	-0.00099	-0.00110	-0.00121	0.00083	-0.0152	-0.0284
2	-0.5289	-0.00099	-0.00110	-0.00121	0.00083	-0.0152	-0.0284
4	-0.5394	-0.00099	-0.00110	-0.00121	0.00083	-0.0105	-0.0284
15.0	-0.5491	-0.00099	-0.00110	-0.00121	-0.00276	0	0.0028

$(\Delta C_{\ell_p})_{n(\Delta\bar{q} + \varepsilon_p)}$ (Eq. 6.2.1.3)			(C_{ℓ_p}), per rad (Eq. 6.2.1.4)		
T'_c			T'_c		
0	.0915	.1970	0	.0915	.0970
0.00011	-0.00059	-0.00146	-0.5399	-0.5567	-0.5792
0.00012	-0.00062	-0.00153	-0.5391	-0.5560	-0.5758
0.00012	-0.00064	-0.00159	-0.5388	-0.5557	-0.5700
0.00013	-0.00067	-0.00165	-0.5289	-0.5459	-0.5602
0.00013	-0.00069	-0.00171	-0.5394	-0.5517	-0.5707
0.00016	-0.00085	-0.00209	-0.5527	-0.5511	-0.5496

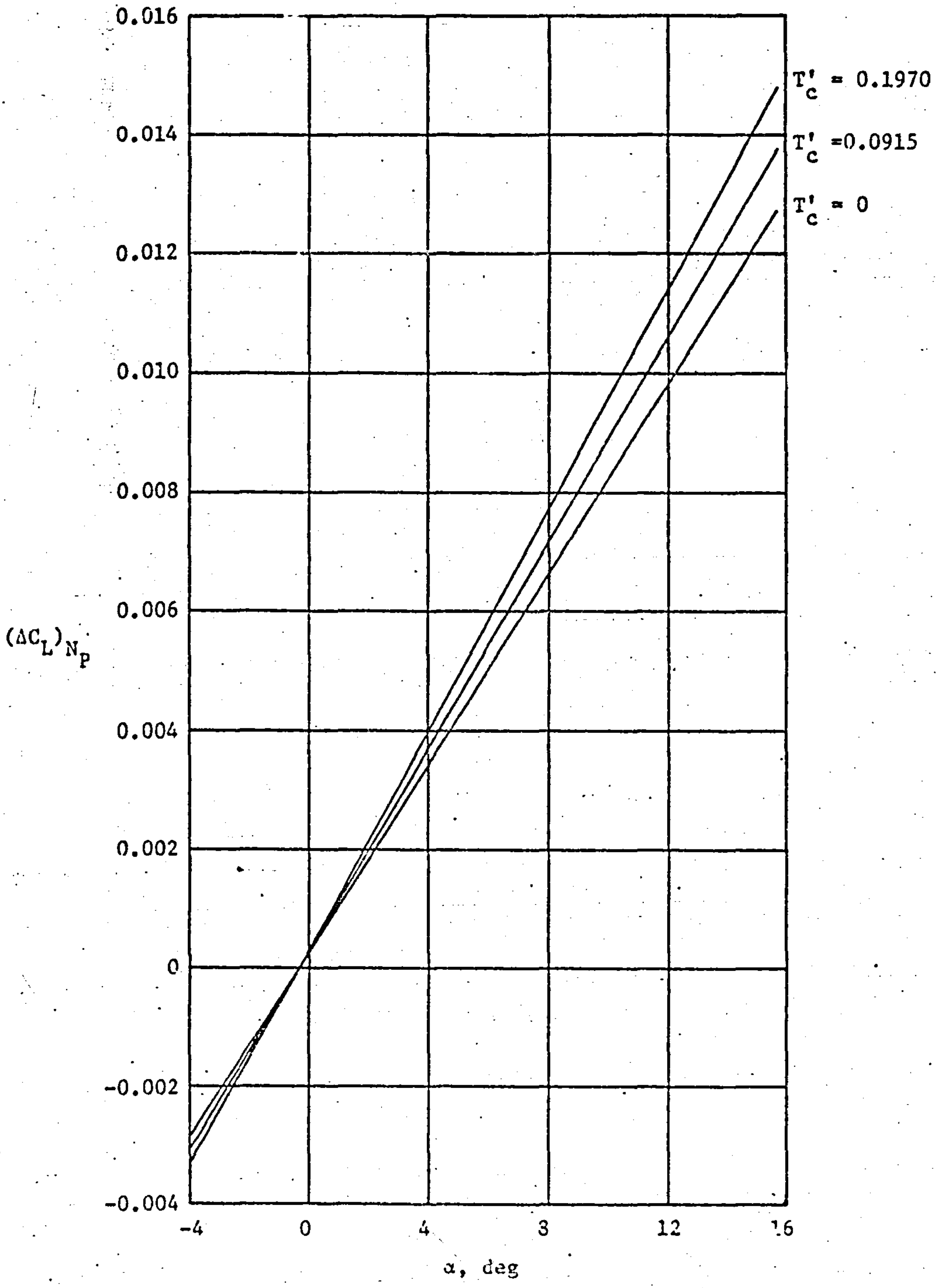

Figure 6.2.1.1: Increment in lift due to propeller normal force (Reference 1)

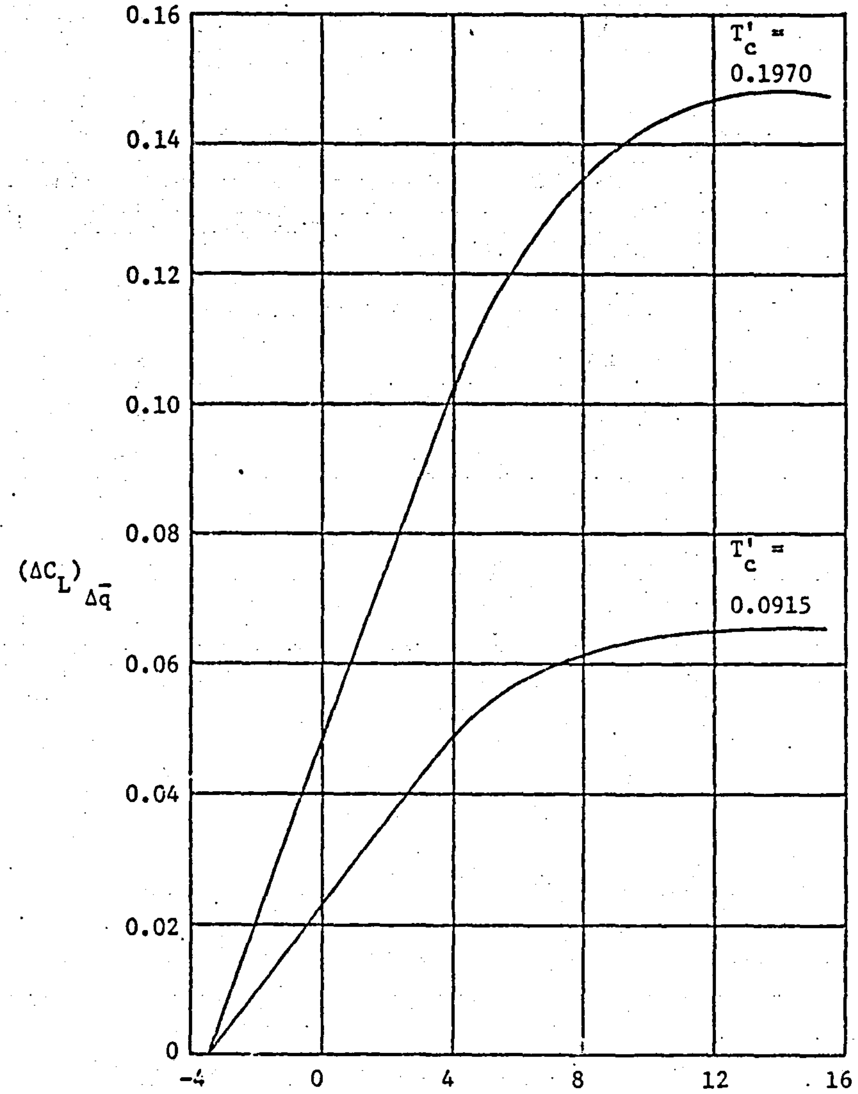

Figure 6.2.1.2: Increment in lift due to increased dynamic pressure behind the propeller (Reference 1)

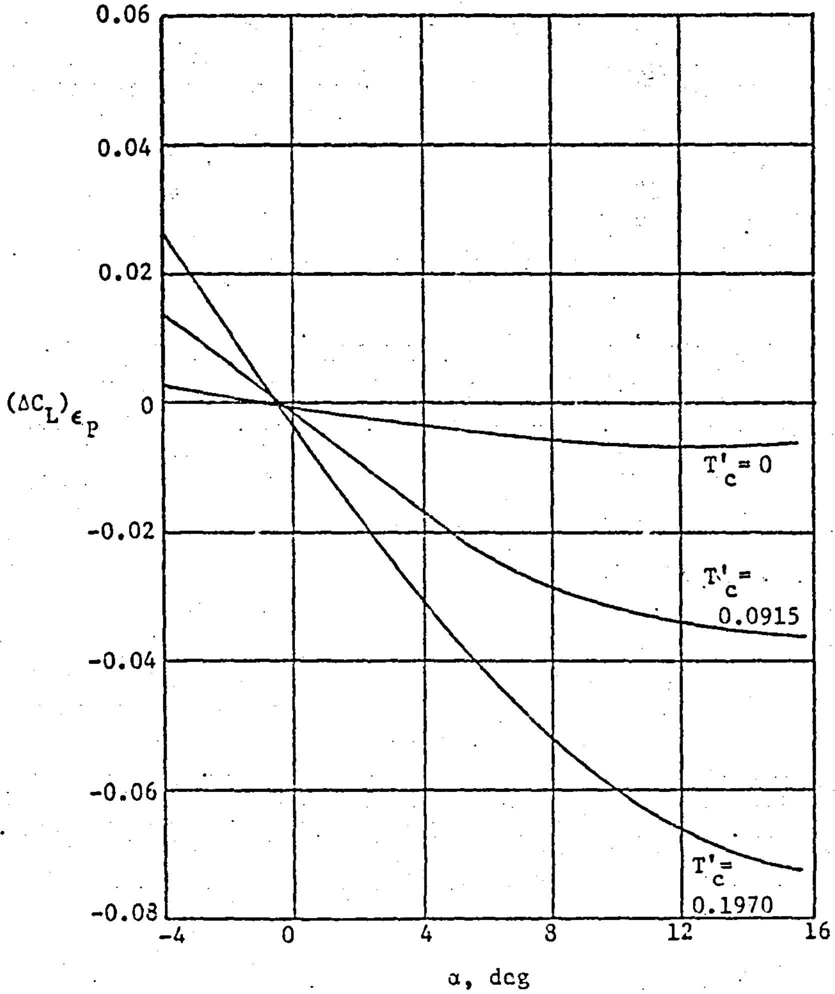

Figure 6.2.1.3: Increment in lift due to propeller downwash (Reference 1)

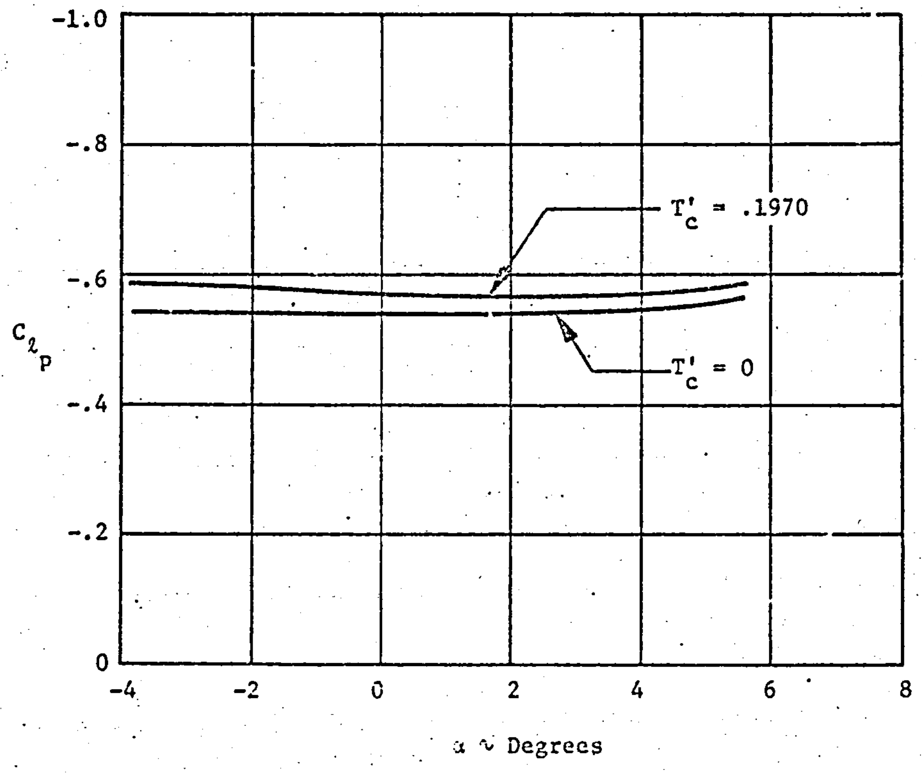

Figure 6.2.1.4: Effect of power on predicted C_{ℓ_p} of the ATLIT Airplane

CHAPTER 7

CONCLUSIONS AND RECOMMENDATIONS

This report presents an analytical method for predicting the lateral-directional aerodynamic characteristics of light twin-engine airplanes. This method is applied to the Advanced Technology Light Twin (ATLIT) airplane, and the predictions are then compared to full-scale wind tunnel data.

Based upon this comparison, the following observations and conclusions are presented:

1. The predicted values of C_{Y_β} are lower than the wind tunnel values; however, the overall value is fairly reasonable, especially for preliminary design. It is necessary to consider more completely the effect of angle of attack. The two areas that are thought to need the most study are the fuselage C_{Y_β} variation with angle of attack and the fuselage-vertical tail interference variation with angle of attack.
2. For the power-off case at least, the average predicted values of C_{n_β} show fairly good agreement with wind tunnel data. The tunnel tests show large variations of C_{n_β} with angle of attack, especially with power on. The contribution of the fuselage is strongly influenced by the wing location, and only partial methods are available to account for it. A more detailed study needs to be conducted to determine the effect of wing location and angle of attack.

3. The predicted C_{ℓ_β} of the ATLIT is slightly higher than wind tunnel results but still compares quite well.
4. The spoiler performance, both rolling and yawing moments, is predicted somewhat higher than found in the wind tunnel data. However, the agreement is still quite good considering the highly general nature of the methods used. A method should be developed which is tailored to general aviation airplanes.
5. The prediction of the rudder derivatives was disappointing. But again it appears that the angle of attack factors have not been accounted for. The angle of attack variation of the wing and body wake needs to be included in the prediction method.
6. The dynamic derivatives are also presented in this report. When experimental data becomes available, it should be correlated with these predictions to evaluate the prediction method.
7. There needs to be more power-on wind tunnel data in order to better correlate the effects of power. Only limited power data was available, and it was at a relatively low thrust coefficient.
8. The data in this report and in Reference 1 should be correlated with flight test data as it becomes available.

REFERENCES

1. Roskam, J.; Van Dam, C., and Griswold, M., "Comparison of Theoretically Predicted Longitudinal Aerodynamic Characteristics with Full-Scale Wind Tunnel Data on the ATLIT Airplane," KU-FRL-399-1, University of Kansas, July 1979.

2. Hassell, J. L., Jr., "Full-Scale Wind Tunnel Investigation of an Advanced Technology Light Twin-Engine Airplane (ATLIT)," Proposed NASA TP, 1979.

3. Wolowicz, C. H., and Yancey, R. B., "Lateral-Directional Aerodynamic Characteristics of Light, Twin-Engine Propeller Driven Airplanes," NASA TN D-6146, October 1972.

4. Finck, R. D., and Hoak, D. E., "USAF Stability and Control DATCOM," Air Force Flight Dynamics Laboratory, Wright Patterson Air Force Base, Ohio, October 1960 (Revised 1975).

5. Holmes, B. J., "Flight Evaluation of an Advanced Technology Light Twin-Engine Airplane (ATLIT)," NASA CR-2832, July 1977.

6. Wolowicz, C. H., and Yancey, R. B., "Longitudinal Aerodynamic Characteristics of Light, Twin-Engine, Propeller Driven Airplanes," NASA TN-D-6800, June 1972.

APPENDIX A

A SIMPLE METHOD FOR COMPUTING WING VISCOUS DRAG, C_{D_o}'

APPENDIX A

A SIMPLE METHOD FOR COMPUTING WING VISCOUS DRAG, C_{D_o}'

The wing drag which varies with angle of attack is comprised of two components. First is the drag due to direct lift production (vortex drag). The second is a type of profile drag caused by the buildup of the upper surface boundary layer as angle of attack increases (viscous drag). Together these two factors comprise the induced drag. Since the viscous drag term is needed for the prediction of C_{n_p}, the following procedure from Reference 6 is given.

Equation B.1 gives the viscous drag of a wing.

$$C_{D_o}' = k\,\Delta \tag{A.1}$$

where

k is an empirical sweep correction factor obtained from Figure A.1 as a function of sweep and the parameter J given in Equation A.2

Δ is the empirical viscous drag increment factor from Figure A.2, also a function of J

and where

$$J = 0.3(c_1 + 1)\,\frac{A_w}{B_1}\cos_{\Lambda le}\left\{(c_1 + 1)(c_2 + 1) - \left[\frac{(c_2 + 1)\tan_{\Lambda le}}{7}\right]^3\right\} \tag{A.2}$$

where

c_1 and c_2 are taper ratio constants obtained from Figure A.3.

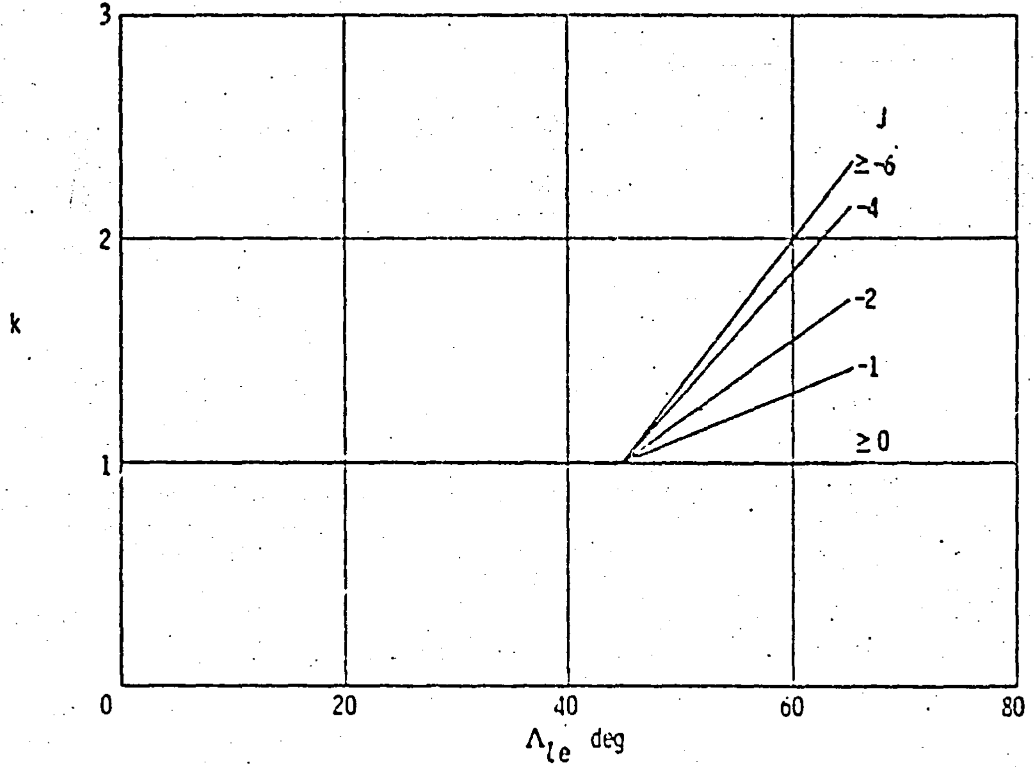

Figure A.1: Sweep correction factor (Reference 6)

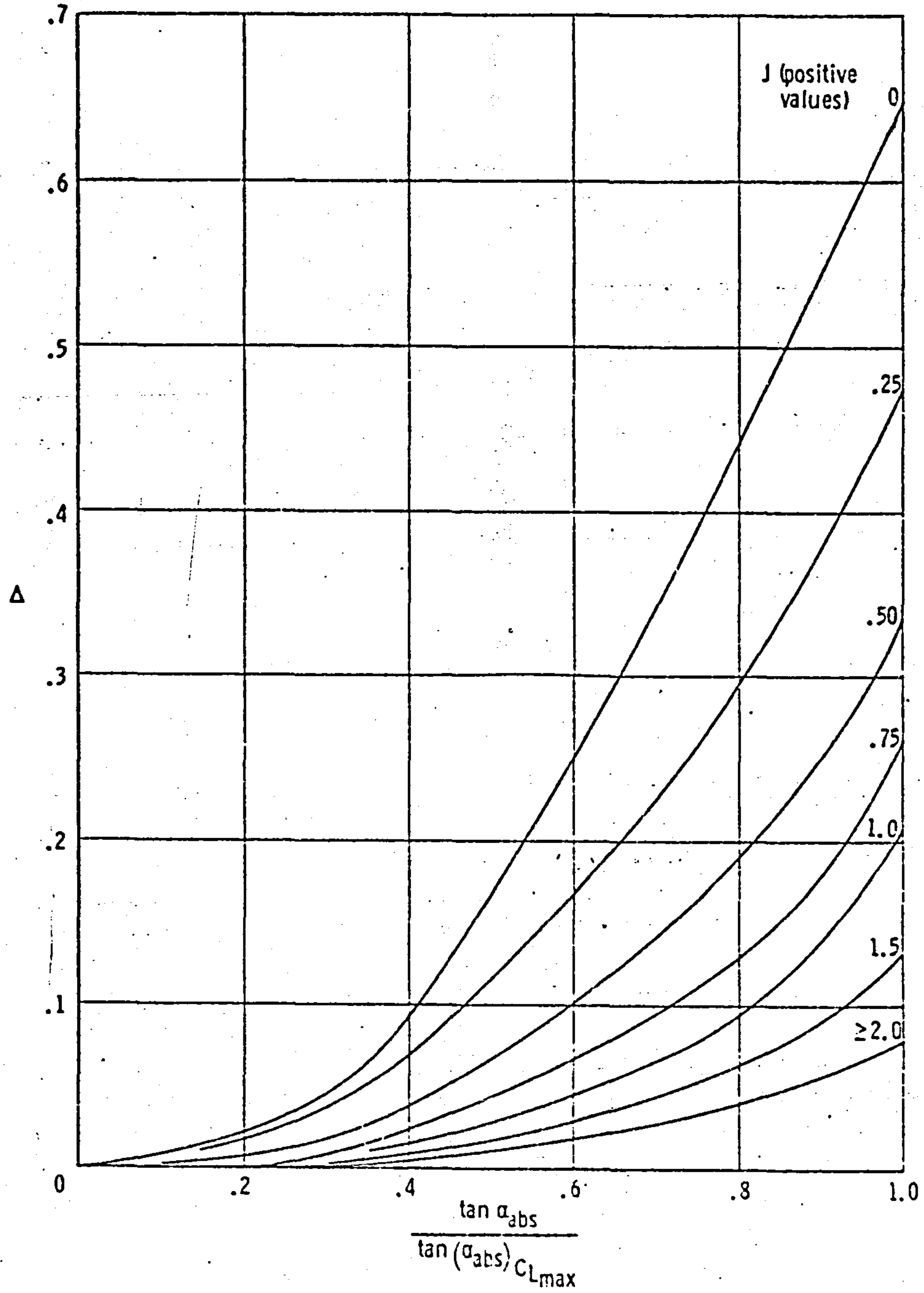

Figure A.2: Viscous drag increment factor (Reference 6)

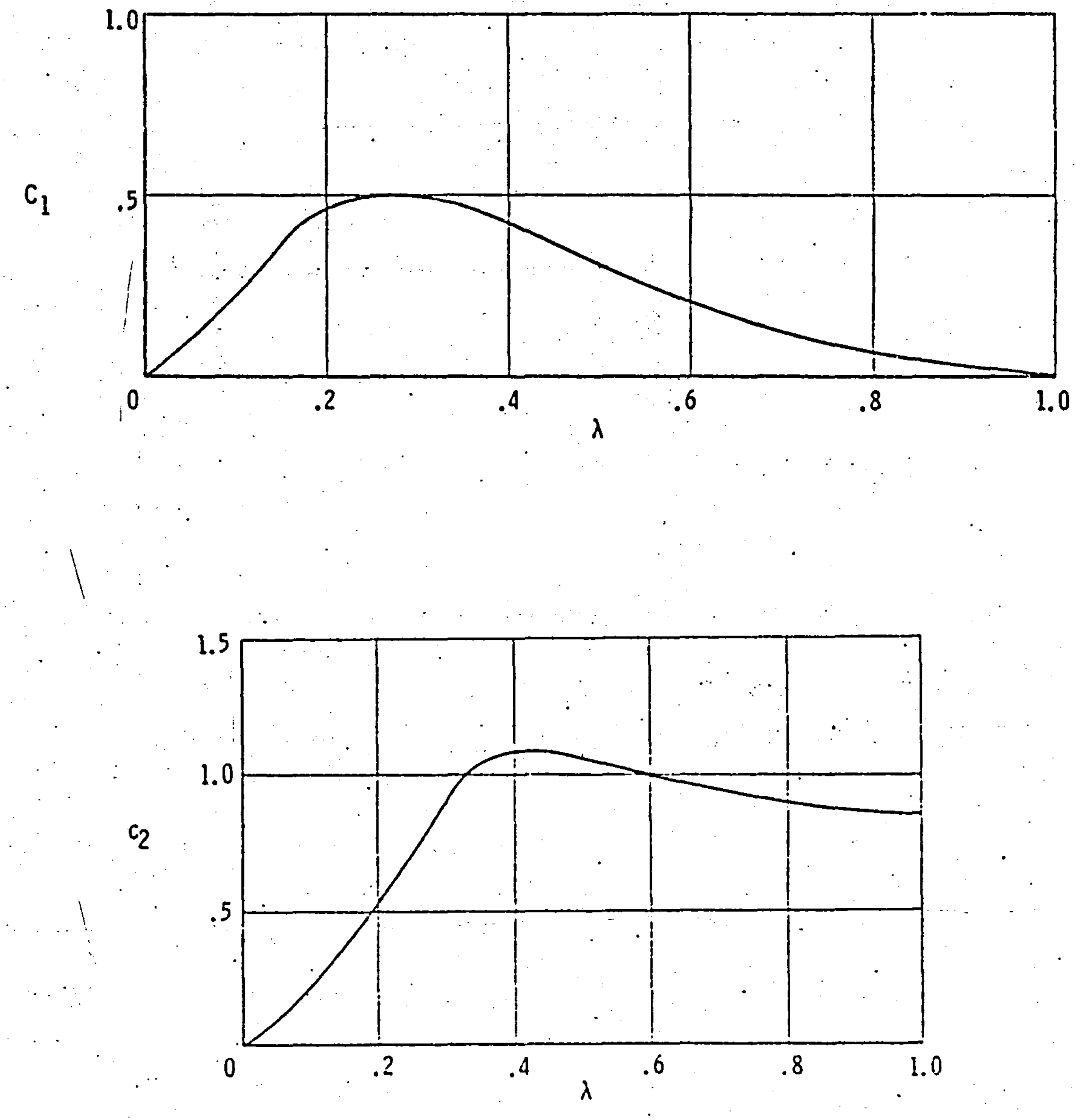

Figure A.3: Taper ratio factors for C_{D_o}' (Reference 6)

END

DATE

FILMED

JUL 23 1980

End of Document